5-2015

# Synthesis of Mesoporous Carbon for Carbon Dioxide Capture and Sequestration

Kimberly Marie Nelson
*University of Tennessee - Knoxville*, knelso12@vols.utk.edu

To the Graduate Council:

I am submitting herewith a dissertation written by Kimberly Marie Nelson entitled "Synthesis of Mesoporous Carbon for Carbon Dioxide Capture and Sequestration." I have examined the final electronic copy of this dissertation for form and content and recommend that it be accepted in partial fulfillment of the requirements for the degree of Doctor of Philosophy, with a major in Chemistry.

Sheng Dai, Major Professor

We have read this dissertation and recommend its acceptance:

Jimmy Mays, Ziling Xue, Robert Counce

Accepted for the Council:

Carolyn R. Hodges

Vice Provost and Dean of the Graduate School

(Original signatures are on file with official student records.)

# Synthesis of Mesoporous Carbon for Carbon Dioxide Capture and Sequestration

A Dissertation Presented for the

Doctor of Philosophy

Degree

The University of Tennessee, Knoxville

Kimberly Marie Nelson

May 2015

*"Never risking anything meant never having or doing or being anything either. Life is risk, it turned out."*

— Lev Grossman, *The Magician's Land*

# ACKNOWLEDGEMENTS

These last few years have showed the value of the people that help you through your work. Firstly, I would like to offer my thanks to my advisor, Dr. Sheng Dai, who is renowned in the field of porous materials and has guided me through this project.

I would like to thank the rest of my thesis committee: the late Dr. Georges Guiochon for his friendship and guidance. His optimism and exuberance helped immensely when motivation was needed. Dr. Jimmy Mays for his gracious help on my committee and reminding me that science and life can be exciting. Many thanks to Dr. Robert (Pete) Counce for his patience and encouragement and I would also thank Dr. Ziling (Ben) Xue graciously taking a position on my committee under the circumstances.

My sincere thanks to Dr. Shannon Mahurin and Dr. Richard Mayes for the immense amount of help, instruction, and collaboration on a number of projects as well as the camaraderie. I give many thanks to my lab mates: Dr. Yatsandra Oyola, Zhen An Qiao, Andrew Binder, Jonathan Powell, Nada Mehio, Chi-Linh Do-Thanh, and Joseph Stankovich for mutual help and friendship. Also, I thank all my friends at UTK the past few years. There has never been a place where I have felt such friendship and support.

I would like to thank Andrew Goodwin for our chemistry synergy and loving support. I would also like to thank my mother, Christine, my father, Rocky, and my sister, Leslie, for supporting me in this endeavor.

# ABSTRACT

The growing evidence and concern over global climate change has presented the relevant nature and urgency for carbon dioxide $CO_2$ emission regulations. With the economical gap between fossil fuel based energy and renewable energy sources' slowly gradually closing with the technological innovations, the current need exists for a cost-effective solution to $CO_2$ sequestration. This examination of synthesis techniques for activated porous carbon as $CO_2$ adsorbents provides a non-contradictory approach, *via* "green" synthesis, for selective and energy efficient capture. In this work, the "green" synthesis is approached through the established techniques and activation of monolithic carbon, establishing a templating approach, and using biomass as a carbon precursor.

A soft-templating synthesis is used where phenolic-formaldehyde (PF) resin is polymerized in the presences of an amphiphilic triblock copolymer where, upon calcination, the elimination of the triblock copolymer reveals an inverse carbon replica. For hierarchical meso-macroporous carbon monoliths, dual phase separation of the phloroglucinol-formaldehyde (PF) - triblock copolymer gel in glycolic solvent separates into macroporous domains to form a rod. The porosity of the porous carbon monoliths and the relationship to $CO_2$ capture capacity was examined as a function of the calcination temperature and subsequent activation with potassium hydroxide and $CO_2$.

By using soft-templating, green reactants can be used to further pursue our means-end product. In lieu of the triblock copolymer, using linear poly (ethylene glycol) (PEG) reduces the

cost and increases the tunability of the synthesis. Polymerization induced phase separation of the PF-PEG blend occurs through spinodal decomposition and, upon calcination, results in mesoporous carbon. The mesoporosity can be tuned through both the ratio of precursors and the molecular weight of the linear PEG, and activated for microporosity for $CO_2$ adsorption.

Interchanging the phenolic moiety with biomass eliminates the need for further refinement of precursors and accessibility to large-scale synthesis. Chestnut tannin, a hydrolysable polyphenolic, was used and with a triblock copolymer, which resulted in the morphology tunability with weight ratio. Moreover, the tunable structures were only found without the addition of acid. Upon high temperature activation with ammonia, increased microporosity and the addition of nitrogen functionality attributed to increased $CO_2$ uptake capacity.

# TABLE OF CONTENTS

# LIST OF TABLES

# LIST OF FIGURES

# CHAPTER 1.
# INTRODUCTION AND MOTIVATION

## 1.1 Motivation

The evidence of global climate change is nearly undisputable among the scientific community and includes: rising sea levels, melting ice sheets, global temperature rise, warming oceans, glacial retreat, extreme weather, and ocean acidification.[1] Increasing temperatures via the "green house effect" are known to be caused by increased levels of "green house gases" (GHGs): carbon dioxide ($CO_2$), methane ($CH_4$), nitrous oxide ($N_2O$), hydrofluorocarbons (HFCs), perfluorocarbons (PFCs) and sulfur hexafluoride (SF6).[2] Although, throughout the history of the Earth there is evidence of periods of heating and cooling due to solar cycles known as Milankovitch cycles, within the past 200 years, increased levels of carbon dioxide can be attributed to burning fossil fuels for energy and electricity (Figure 1).[3] In combination with this, natural processes like volcanic eruption and decay of organic matter release $CO_2$ in the natural carbon cycle but natural remediation due to increased deforestation reveals a net increase of $CO_2$ release.[4]

The reliance on coal for electric generation is staggering considering its' lack of efficiency, the impact of the process on the environment, and the available alternative options.

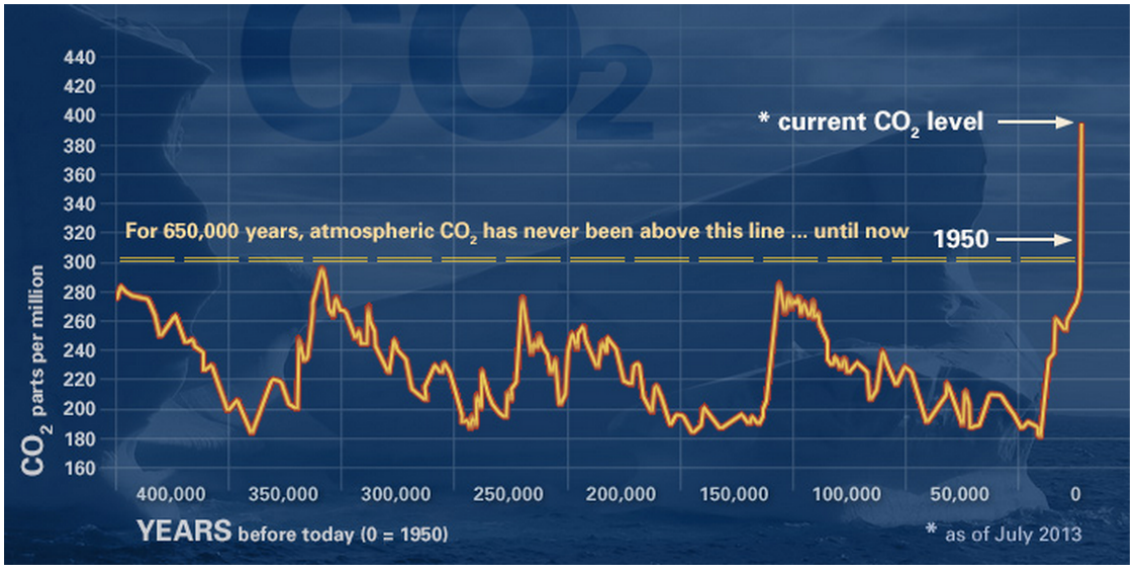


**Figure 1. Global $CO_2$ levels.** ***Reproduced from*** **[1]**

The U.S. coal industry has relied on aging and established facilities because of the immense capital necessary to implement new regulation compliant plants enacted by the Clean Air Act. The Clean Air Act has brought about enormous change with regards to health concerns through regulation of particulate matter, lead, ozone, and carbon monoxide and the environmental pollutants: sulfur dioxide ($SO_2$) and nitrogen oxides ($NO_x$), which are source of acid rain.[5] As a result, systems for removal of $SO_2$ and $NO_x$ have been implemented in the form of selective catalytic reduction (SCR) and flue gas desulfurization (FGD) systems. The SCR system involves the injection of anhydrous ammonia ($NH_3$) into the flue gas stream to react with the $NO_x$ over titanium oxide catalysts to generate $N_2$ and $H_2O$, where further downstream the flue gas is treated with limestone ($CaCO_3$) in a dry FGD or lime ($Ca(OH)_2$) in a wet FGD. Additionally, the flue gas is passed through an electrostatic precipitator (ESP) to remove fly ash. The typical flue gas path shown is shown in Figure 2. With all of these systems, the flue gas needs to be reheated and repressurized, further increasing the energy penalty. Typical coal fired power plants run at an average 32 % efficiency, with the bulk of the energy lost as heat

. The majority of coal fired power plants currently in operation in the United States have not operated at the optimum efficiency established when they were first constructed because of the addition of flue gas cleaning devices.[6]

In the past decade, reevaluation of the coverage of the Clean Air Act prompted the recognition of GHGs providing the motivation for reducing $CO_2$ emissions. With the prospect of coal persevering a mainstay of energy production (Figure 3) due to the capital expense of initializing new and emerging energy technologies, it has become relevant to develop advanced adsorption and separation materials to reduce the harmful $CO_2$ emissions in the interim.

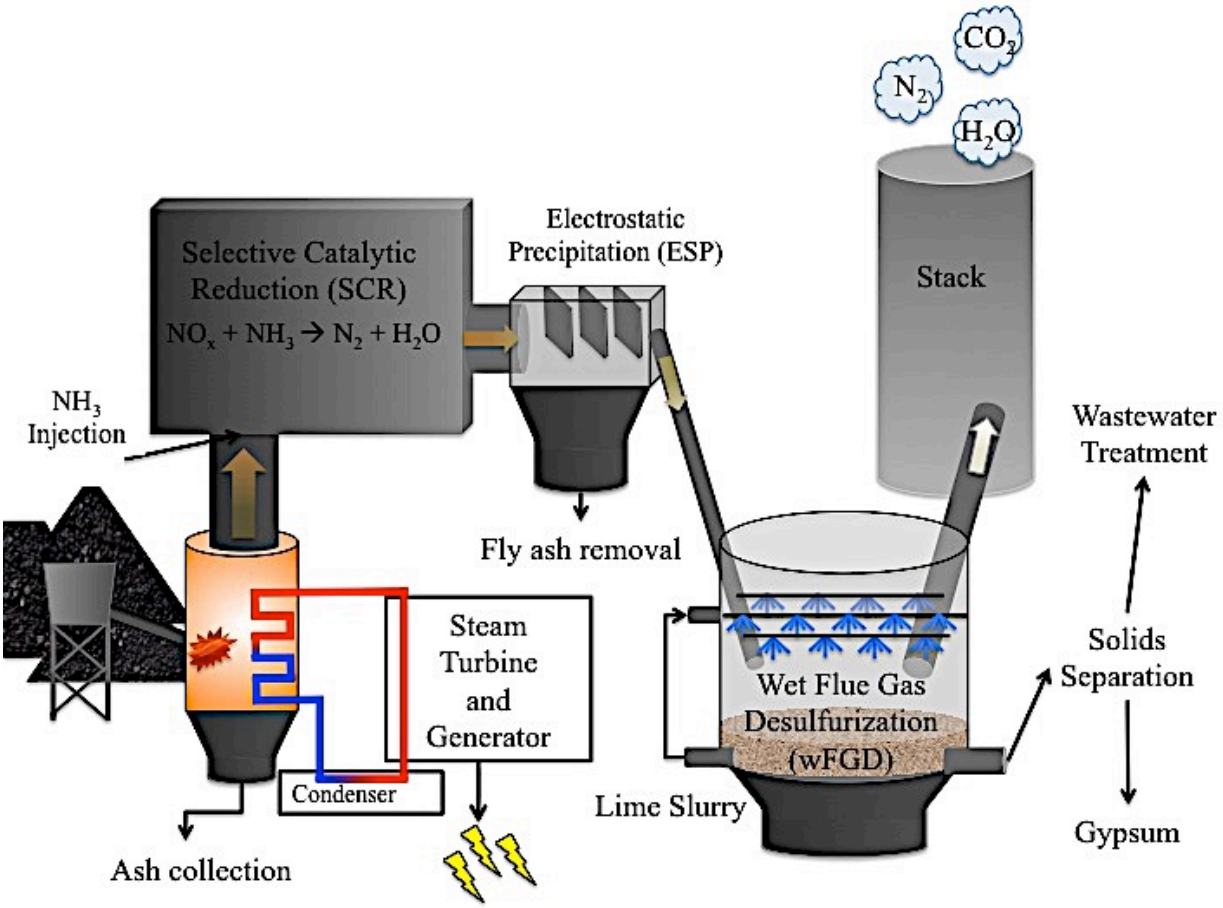


**Figure 2. Schematic diagram of coal fired power plant equipped with various flue gas cleaning systems.**

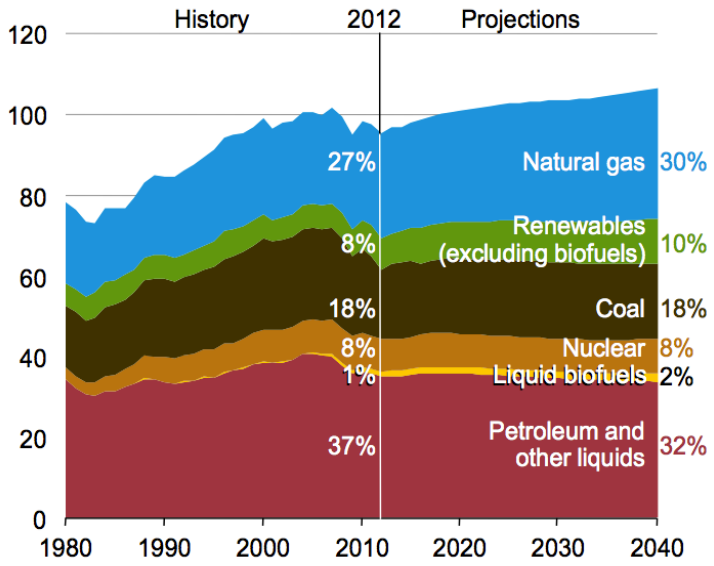


**Figure 3. United States energy consumption by fuel (1980-2040) by quadrillion Btu.** ***Reproduced from*** **[7]**

Porous materials are characterized by their inherit porosity that provide increased surface area for molecular adsorption. Porous materials can exhibit surface areas > 1000 $m^2$ $g^{-1}$ and naturally occur as aluminosilicates minerals *aka* zeolites. Under high temperatures and inert atmosphere, other natural materials can be converted to porous carbon materials. This process was traditionally performed on coal but further material exploration has found that coconut shells, corn cobs, bean dreg, almond shells, and many other biomass residues can reveal porous carbon structures under the same procedure.[8-14] Because of the heterogeneous nature of the starting material, these materials are typically disordered microporous (< 2 nm).

## 1.2 Objectives and Methodology

The goal of this study was to understand the adsorption behavior of $CO_2$ on porous carbon adsorbents. The primary objective was to synthesize a selective medium for adsorption of $CO_2$ from $N_2$, the primary components in flue gas. For selective and uniform adsorption and desorption of $CO_2$, it is necessary to obtain an ordered, high surface area adsorbent that can be inert in the flue gas atmosphere and the nature of the application also requires that the synthesis of the material be "green" and have a low environmental impact. Laboratory experiments and modeling provide the necessary assessment for industrial scale viability and knowledge of the gas sorption on carbon for separation processes.

For adsorption experiments, the carbon polymer precursor used was a phenolic, phloroglucinol or chestnut tannin, cross-linked with formaldehyde or glyoxal with a templating agent. With various synthesis conditions, morphology changes are observed in the resulting

carbon. The replacement of the traditional triblock copolymer template to a tunable sacrificial templating agent was then accomplished. Laboratory experiments to measure the amount (gravimetric) of pure gas sorption along a range of pressure conditions afford the necessary data for analysis of the surface interactions with each adsorbate. Sorption modeling of the experimental results can provide the more valuable mixed gas adsorption data. Modeling can better help us predict real conditions through our ideal laboratory experiments.

## 1.3 Organization of Dissertation

In this chapter, the motivation, objectives and general methodology of the study were briefly introduced. The next chapter, *Chapter 2*, contains the necessary background information on the representative characteristics of porous carbon and existing materials used for $CO_2$ sequestration from flue gas streams. In *Chapter 3*, descriptions of the experimental apparatus's and procedures, data processing, and sorption modeling are explained. The established technique for synthesis of monolithic carbon and the pore and surface characteristics using a range of calcination temperatures is examined in *Chapter 4. Chapter 5* studies using linear polyethylene glycol as a templating agent of phenolic resin carbon precursors. *Chapter 6* includes results and analysis of carbon derived from chestnut tannin using a soft template synthesis. *Chapter 7* examines the different activation techniques for increasing $CO_2$ adsorption capacity of carbons produced in *Chapter 4, 5, and 6*. Finally, *Chapter 8* summarizes the breadth of work included in this dissertation and lists some suggestions for further investigation.

# CHAPTER 2. BACKGROUND AND THEORY

## 2.1 Carbon Structure

Calcination is the heat treatment process of a material under inert atmosphere to obtain a primarily carbon substance. The process of calcination creates sheets of 5 and 6 membered rings but unlike graphitization, which takes temperatures reaching passed the thousands of degrees Celsius, calcination occurs under 1000 $^{o}$C in the absence of oxygen or air. The process takes a carbon source and with increasing temperatures, gradually decomposes and releases the heteroatoms. The decomposition of heteroatom structures is beneficial to removing soft-templates, which typically contain heteroatoms in the primary backbone, leading to decomposition and removal at relatively low temperatures (400 $^{o}$C to 500 $^{o}$C).

Typical carbon sources consist primarily of carbon, oxygen, nitrogen and hydrogen. The various oxygen groups outlined in Figure 4 are those commonly found on carbon surfaces and their respective decomposition temperatures and products measured by temperature programmed decomposition (TPD).[15] While oxygen heteroatoms can provide increased wettability and polarity, most oxygen functional groups also increase acidity of the carbon surface. The additional acidity can be detrimental to the adsorption of $CO_2$, which is an acid gas. Coincidentally, the oxygen functional groups provide chemical reactivity sites for ammonia,

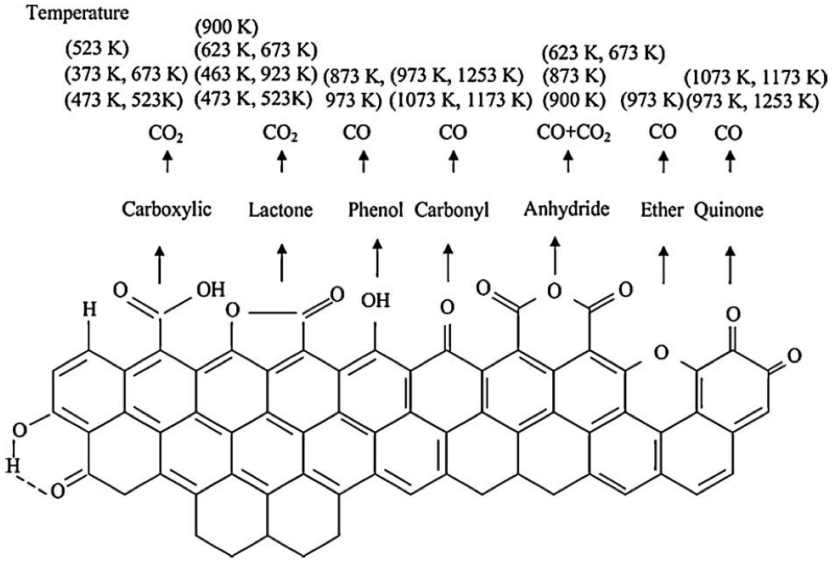


**Figure 4. Various surface oxygen containing groups and their respective decomposition temperatures.** ***Reproduced from*** **[15].**

adding basic nitrogen functionalities for $CO_2$ adsorption, which is discussed further in *Chapter 7*. Although using carbon precursors with inherent nitrogen content has provided the desired nitrogen functionality post-calcination, retaining large amounts on the surface remains elusive due to the nature of the process. As the heteroatoms are eliminated from the carbon structure, the interstitial spacing between the carbon sheets is reduced and the contraction of the structure allows for the sheets to stack into parallel layers, creating a graphitic like structure Figure 5. The contraction also applies to the pores, where expansion of the macro and mesostructure occurs due to the gasification of decomposition products and their transport followed by contraction and annealing.

## 2.2 Gas Sorption on Porous Carbon

Porous carbon has been used as an adsorbent for harmful gases and liquids for many centuries. One of the reasons that it has been used so extensively is the high capacity due to the high surface area found in activated carbon. The amount of adsorption of a specific adsorbate (V) is a function of pressure (P) and temperature (T):

$$V = F(P,T) \qquad (1)$$

In isothermal conditions, the adsorption capacity is only a function of pressure. Sorption isotherms can be collected as concentration versus pressure either gravimetrically (mole uptake) or volumetrically ($cm^3$ uptake) per unit mass of adsorbate.

Adsorption isotherms can be evaluated through qualitative understanding of isotherm types (Figure 6) that have been evaluated thoroughly and are characteristic of certain materials.

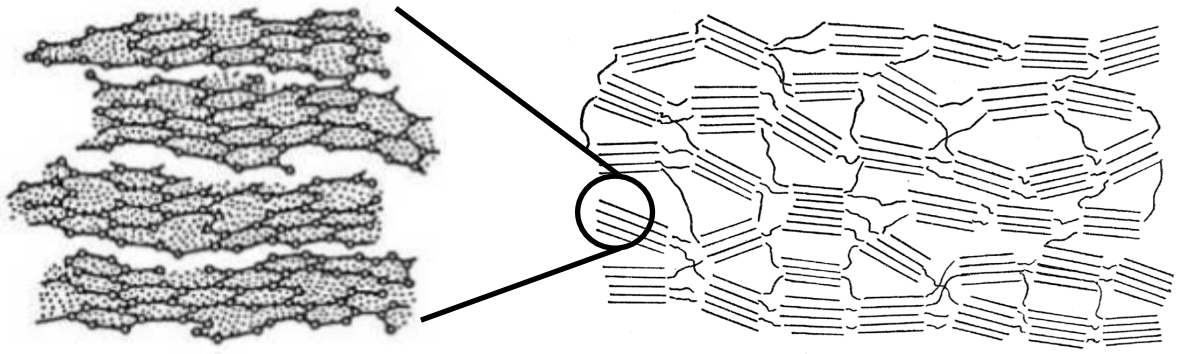

**Figure 5. Carbonized structure indicating the interlayer spacing caused by heteroatoms (left) and partially cross-linked layers (right), indicative of non-graphitizing carbon.** ***Reproduced from [16] and [17]***

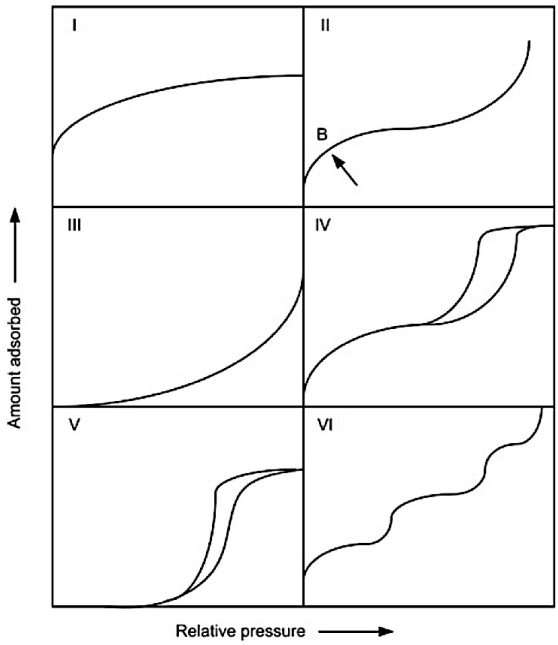


**Figure 6. Characteristic $N_2$ adsorption isotherms for (I) predominately microporous, (II) predominately macroporous, (III) weak interactions at the fluid-wall interface, (IV) mesoporous, (V) combination of type III and type IV, and (VI) step-wise adsorption.** ***Reproduced from*** **[18]**

With mesoporous carbon materials, the most frequently found isotherms are of types I and IV for microporous and mesoporous carbon, respectively, and graphitic carbon can exhibit types III and V when there is decreased interaction of the adsorbate with the material through the lack of heteroatoms and defects on the surface.[18] The isotherm type is indicative of the types of pores and surfaces present, particular emphasis is on the mesoporosity that the shape of the hysteresis must also be considered as it provides information about the mesopore shape and size distribution. The type IV isotherm is clearly distinguishable through the presence of the hysteresis. The hysteresis is due to condensation of adsorbate in the mesopores below saturation pressure i.e. capillary condensation. The classification of mesopore hystereses was first established by de Boer and then adopted by IUPAC, as shown in Figure 7.[18]

The adsorption in the H1 hysteresis is relatively flat and then steeply elevates to a plateau at a relative pressure of ~1 Bar with the desorption hysteresis following a parallel path and eventually overlapping with the adsorption curve. The H1 hysteresis is indicative of cylinder shaped pores and can be found in ordered mesoporous materials. In cylindrical, interconnected pores there is no desorption delay and the desorption meets the adsorption curve at >0.45 $P/P_o$, in contrast to the forced closures like those found in the H3 and H4 type hystereses. The forced closure at ~0.45 $P/P_o$ can occur either due to constrictions that would be found in "ink-bottle" shaped pores (H2) or adsorption in confined slit-shaped pores (H3). The type H2 hysteresis occurs with interconnected pores that show a distribution in both size and shape. Furthermore, in cases where desorption curves do not connect back to the adsorption branch is caused by to adsorbate remaining in the pore structure.

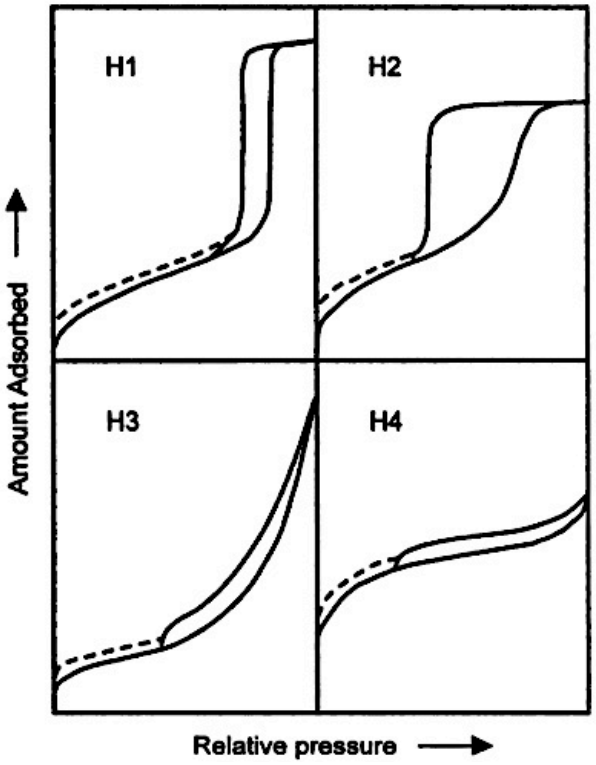


**Figure 7. IUPAC classifications for hysteresis loops.** ***Reproduced from*** **[19]**

To quantify the adsorption isotherm, several model methods and parameters to obtain: specific surface area, micropore surface area, total pore volume, micropore volume, pore size distribution, and average pore size. Furthermore, instrumentation that can utilize the ultra-low pressure range can provide a micropore profile to obtain micropore sizes and corresponding histograms in the micropore regime using density functional theory (DFT) to quantify pore diameters as low as ~0.5 nm. The surface area in the ultramicropore (0.5 - 0.7 nm) and supermicropore (0.7-1 nm) helps evaluate the overall capacity contribution of these pores to $CO_2$ adsorption.

### 2.2.1 Langmuir and Brunauer-Emmett-Teller (BET) equations for surface area analysis

Analysis of adsorption of $N_2$ onto the surface of a porous substrate requires mathematical modeling equations. The most famous of these, the Langmuir equation, is the reference for the more recent standard for multilayer adsorption analysis: Brunauer-Emmett-Teller (BET) equation. Adsorption onto a flat surface was first proposed by Langmuir.[20] This model presumes a homogeneous surface, with adsorption energy constant over all adsorption sites and Henry's law i.e. there is a relationship between coverage and pressure. The adsorption sites are definite and, at equilibrium, the rate of adsorption is the same of that of desorption. The Langmuir equation is written in terms of fractional loading (θ):

$$\theta = \frac{bP}{1+bP} \qquad (2)$$

with an affinity parameter ($b$) and pressure ($P$). For complete monolayer adsorption coverage, $q$, is introduced in the modified Langmuir as the amount adsorbed (mmol $g^{-1}$) and $q_{sat}$ for the maximum coverage capacity:

$$n_i^o = \frac{q_{sat} bP}{1 + bP} \tag{3}$$

Furthermore, a temperature dependent affinity parameter yields:

$$b = b_o \exp\left(\frac{E}{RT}\right) \tag{4}$$

Furthermore, the affinity constant, $b_o$, (Equation 4) is a function of temperature ($T$) the heat of adsorption ($E$), the gas constant ($R$).

The Langmuir equation is limited to only one monolayer, as in, it only accounts for adsorbate-adsorbent interactions and it does not account for adsorbate-adsorbate interactions or condensation. The BET equation (Equations 5 and 6) in terms of volumes at constant pressure and masses is an extension of the Langmuir equation and includes the Langmuir monolayer adsorption but adds that after the first layer is adsorbed the second layer is on top of the first, the third is on the second, etc.[21]

$$\frac{P}{m(P_0 - P)} = \frac{1}{m_\infty C} + \frac{C-1}{m_\infty C} \times \frac{P}{P_0} \tag{5}$$

$$\frac{P}{V(P_0 - P)} = \frac{1}{V_\infty C} + \frac{C-1}{V_\infty C} \times \frac{P}{P_0} \tag{6}$$

To obtain the surface area with the BET constant (*C),* mass (*m),* and volume (*V)* at the given relative pressure ($P/P_o$), graphing of $\frac{P}{V(P_o-P)}$ vs. $P/P_o$ between 0.05 and 0.3 $P/P_o$ reveals a linear plot. When fit with a least squares linear regression, the slope (*s)* and the intercept (*i)* corresponding to values for $(C\text{-}1)/CV_\infty$ and $1/V_\infty C$, respectively. The monolayer adsorption capacity, $V_m$, and BET constant ($C$) are calculated by:

$$V_m = \frac{1}{s+i} \tag{7}$$

and

$$C = (s/i)+1 \tag{8}$$

From this information the total surface area can then be found through the following equation:

$$S_{Total} = \frac{V_m \times N \times s}{V} \tag{9}$$

The total surface area ($S_{total}$) takes into account the Avogadro's number (*N,* 6.022 x $10^{23}$), the cross-sectional surface area of the adsorbate, *s,* (0.162 nm for nitrogen), and the molar volume (*V)*. The $S_{total}$ ($m^2$) can then be divided by the amount used in analysis to get $S_{BET}$ in $m^2\ g^{-1}$.

### 2.2.2 Pore Size Analysis

The total pore volume is derived from the amount of $N_2$ adsorbed at $P/P_o$ = 1. In the presence of macropores, the adsorbed amount will quickly rise at this pressure. The conversion of adsorbed volume ($V_{ads}$) to the volume of liquid nitrogen ($V_{liq}$) is done by:

$$V_{liq} = \frac{P_a V_{ads} V_m}{RT} \quad (10)$$

where ambient pressure ($P_a$), ambient temperature ($T$), and molar volume of nitrogen ($V_m$) (34.7 $cm^3$/mol) provide the total pore volume. This is used to get an average pore radius ($r_p$):

$$r_p = \frac{2V_{liq}}{S} \quad (11)$$

using the specific surface area (S). Equation 11 has simply solved for the radius of an open-ended cylinder, making this applicable only to cylindrical mesopores (Figure 7, H1 hysteresis). These limitations require the pore shape to be known for a more accurate pore radius.

By taking the average pore size, an inaccurate representation of a heterogeneous pore system is made. Several approaches to increase the accuracy of the above method have been made to create a pore size distribution (PSD) with the most popular being the Brunauer-Joyner-Halenda (BJH) method and density functional theory (DFT). The BJH method uses a more active relationship between pore volume, adsorbate thickness, and relative pressure.[21] Furthermore, DFT accounts for forces imposed by the surface of the material and interactions with other molecules.[22] Both methods can be complimentary, with DFT being most useful in the micropore region and BJH being most useful in the mesopore region.

### 2.2.3 Sorbate-Sorbent Interaction

For adsorption to occur there must be negative free energy and entropy decreases with adsorption, leaving negative (exothermic) enthalpy; therefore the affinity constant will decrease

with increasing temperature:

$$\Delta G = \Delta H - T\Delta S \qquad (12)$$

The ratio of the change in enthalpy to the change in amount adsorbed (typically kJ/mol) is the isosteric heat. The isosteric heat can be used to describe the surface interactions between the adsorbent and the adsorbate. There are two sub classifications of adsorption: physisorption and chemisorption. The loosely quantified processes describe the matter by which adsorption is taking place. Adsorption capacity in a porous substrate that amasses *via* physisorption process typically relies on surface topology, that is, the surface area in addition to the size and shape of the pores; whereas chemisorption is, as the name suggests, a chemical process i.e. acid-base, hydrogen bonding, etc. While the deconvolution of the isosteric heat is not possible to reveal the exact contribution by either process, the inherent strength of the forces in chemisorption strongly outweigh those contributed by physisorption, where values of ~40 $kJ \cdot mol^{-1}$ and above characterize primarily a chemisorption progression. Increasing isosteric heat by functionalization of the surface of porous carbons can provide a more selective approach to $CO_2$ adsorption at higher temperatures.[23]

Adsorption is a spontaneous process, which therefore must be characterized by a decrease in total free energy of a system as per the Gibbs free energy (Equation 12). When a component is adsorbed, the entropy of the system decreases thus adsorption is an exothermic process. The heat of adsorption is a measure of the interaction between the adsorbent and the adsorbate. The value can assist in the design of materials as adsorbents and for gas storage. The phase conditions: temperature ($T$) and pressure ($P$) at equilibrium determine this value. The van't Hoff equation represents the relationship between pressure and temperature at loading ($n$):

$$\Delta H_{ads} = R\left(\frac{d\ln P}{d\frac{1}{T}}\right)_n \qquad (13)$$

The isosteric heat can be found at constant loading by plotting ln$P$ vs. (1/$T$) at a range of temperatures, where the slope represents the isosteric heat and the intercept is a constant. Using two temperatures, the Clausius-Clapeyron equation can be rearranged to yield:

$$\ln\left(\frac{P_1}{P_2}\right) = \Delta H_{ads} \times \frac{T_2 - T_1}{R \times T_1 \times T_2} \qquad (14)$$

where $P_1$ and $P_2$ are the pressures from the corresponding isotherms with temperatures $T_1$ and $T_2$, respectively, R=8.315 $J \cdot K^{-1} mol^{-1}$.

Due to instrument limitations, it is necessary to fit adsorption isotherms to obtain accurate pressures at the specified loading. The most commonly used fitting equations are the Langmuir, Freundlich, Sips and Toth Fits, which are explained further in context. Alternatively, temperature dependent model fits provide the heat of adsorption, which is explained in more detail in Section 3.2.

## 2.3 Materials for $CO_2$ Sequestration

A wide variety of materials have evolved for selective and effective $CO_2$ capture and sequestration (CCS). The primary concern when approaching these materials relies on the basis of cost of implementation and maintenance. This cost needs to be evaluated on and centered on

the synthesis of the material. The materials should be thoroughly scrutinized for their own "carbon footprint", as it would be counterintuitive to employ a material that has a net negative capture capacity after being implemented due to the source of the reagent(s), synthesis, stability, and recyclability.[24, 25] This concept will be evident through the evaluation of the materials and processes. These technologies include: absorption and adsorption.

### 2.3.1 Solvent absorption

Solvent absorption, or more specifically monoethanolamine (MEA) absorption of $CO_2$ is currently being implemented.[26] MEA is formed through reaction of ethylene oxide with anhydrous ammonia under high pressure.

Cooled flue gas is passed through an absorber where MEA selectively absorbs $CO_2$, the solvent then goes through a heat exchanger where the $CO_2$ is released and recovered for storage and the solvent is recycled into the absorber.[27] Although easily added to the flue gas pathway, this process yields several disadvantages. Due to the exothermic process of absorption and endothermic nature of desorption, the temperature directly affects these rates and with that comes energy penalties, indicated in Figure 8. In the presence of oxygen, oxidative degradation of MEA occurs in the presence of $Fe^{3+}$ causing corrosion of the steel facilities as well as solvent loss. Degradation of the solvent can also occur with fly ash, $SO_x$, and $NO_x$. Solvent diffusion restricts the rate of absorption as well as the capacity. Although MEA provides a route for relatively easy regeneration, improvement of the absorptive liquid would still involve the same absorption mechanisms that return the same disadvantages of MEA.[28]

### 2.3.2 Porous Adsorbents for $CO_2$ Sequestration

Porous materials consist of any material that displays an architecture where surface area is distributed throughout the material. The surface area is typically found as a combination macropores (> 50 nm), mesopores (2 – 50 nm), and micropores (> 2 nm). [29, 30] The porous material is commonly found as carbon, zeolites, porous silicas, metal organic frameworks (MOFs), covalent organic frameworks (COFs), or porous organic frameworks (POFs).

In order to lower the energy requirements for scrubbing technologies, significant research efforts have been devoted to exploring porous materials with high surface area and excellent thermal stability towards reversible $CO_2$ adsorption.[31] These materials include hybrid microporous and mesoporous materials such as metal-organic frameworks (MOFs), zeolitic-imidazolate frameworks (ZIFs)],[32-36] microporous organic polymers,[37-42] and amine-modified silicas (e.g., "molecular basket" sorbents, hyperbranched aminosilica).[43-47] Materials with high isosteric heats where adsorption proceeds *via* chemisorption, regeneration of adsorbent has a high energy penalty making them good candidates for geological $CO_2$ storage materials, such as oxide materials i.e. MgO, $Al_2O_3$, etc.[44] Chemisorption efficiency can be improved by increasing the number of accessible reacting sites on a given surface area, i.e. N basic sites for increased $CO_2$ uptake efficiency.[48, 49]

In comparison with the traditional CCS technologies, these porous solids with high surface area and lower energy for regeneration have been proven to be a more attractive solution for $CO_2$ separation. However, designing most of these materials requires costly and complex

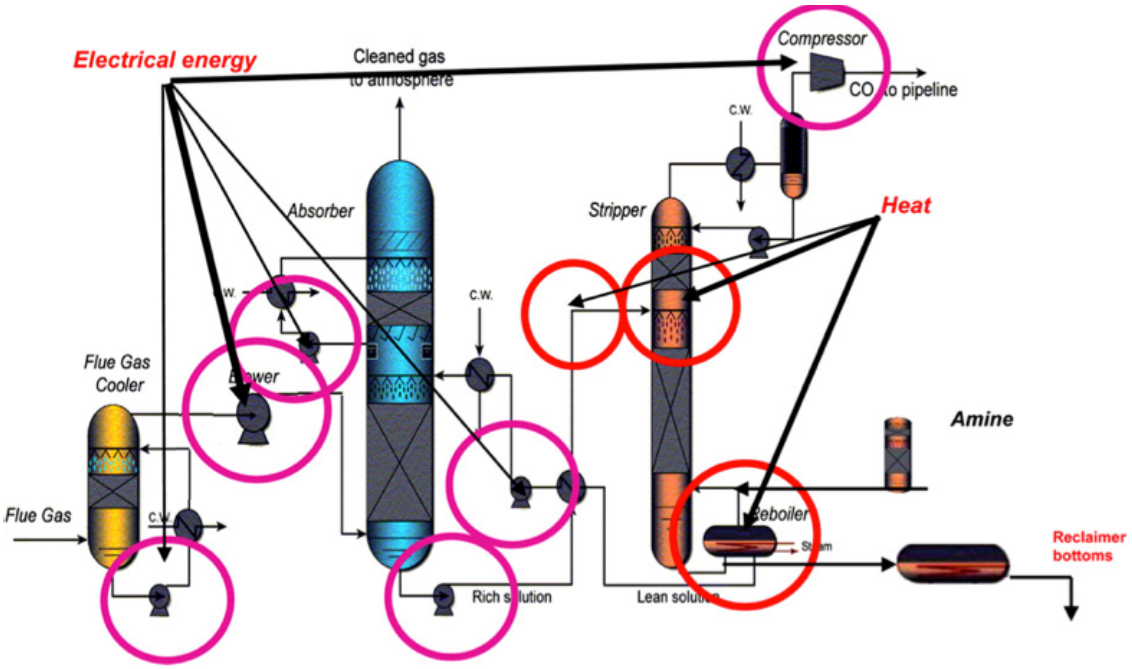


**Figure 8. Schematic of typical monoethanolamine absorption from flue gas, with sources of energy penalty shown.** ***Reproduced from [50].***

fabrication procedures, commonly involving surface modification steps with different types of amine compounds that can facilitate $CO_2$ binding. Furthermore, in some cases, high energies are still needed for their regeneration, consequently damaging and greatly reducing the lifetime of these sorbent materials.[51] Thus, sorbents based on porous carbons are considered to be the promising candidates for $CO_2$ capture due to their good thermal stability and considerably lower energy input required for regeneration, thus extending their lifetimes.

The large availability of carbon precursors and synthetic routes to design sorbents with tailorable pores, large specific surface areas, and surface groups make carbons even more attractive for the development of future CCS technologies. As shown in Figure 9, nitrogen moieties displaying a basic character can be introduced to the carbon framework by using nitrogen-containing precursors or by post-synthesis methods in an effort to improve the affinity for $CO_2$ and consequently the performance for carbon capture.[52] The addition of nitrogen functionalities also enhances the H-bonding interaction with $CO_2$.[53] Given the well-controlled porosity and high $CO_2$ adsorption capacity, various sorbents based on porous carbons have been synthesized and applied for separation processes. A summary of recent research progress on carbon-based $CO_2$ adsorbents is provided. Initial focus is given to nanoporous carbons prepared from biomass, and organic precursors, including the various existing methods to prepare materials with well-defined pores. Finally, carbons with surface nitrogen functionalities are presented, and the effect of carbon precursors and other synthetic parameters on their performances as $CO_2$ adsorbents discussed.

Charcoal was first introduced in Grecian-Roman times where it ingested as medicinal adsorbent for poisons. Activation of the charcoal to increase the surface area improved the

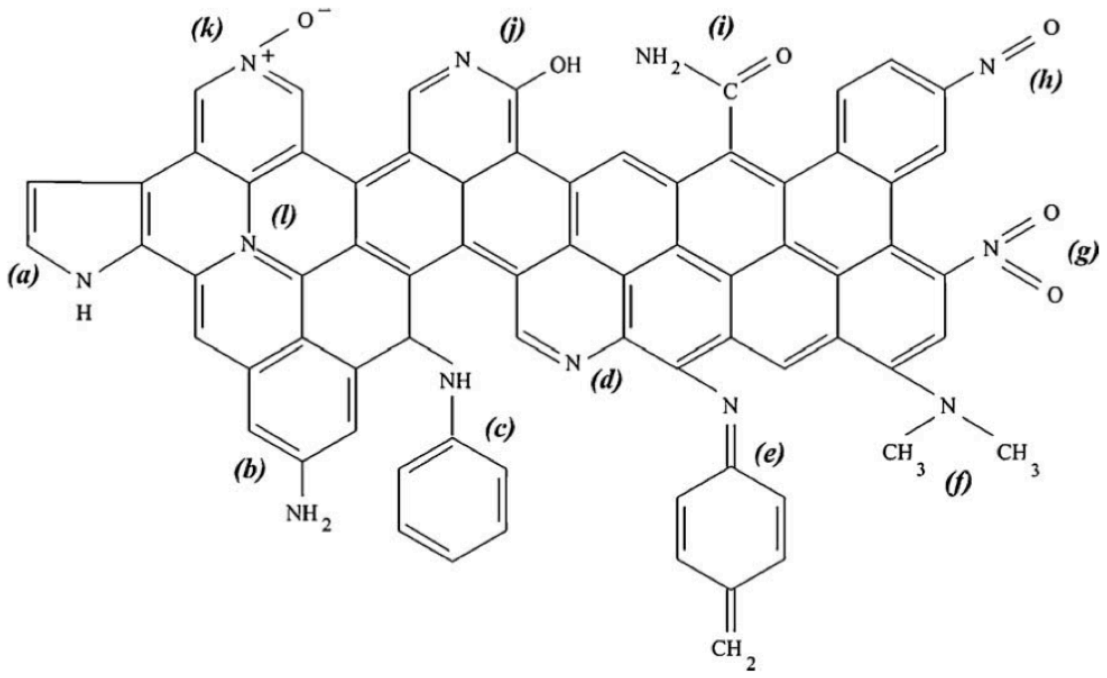


**Figure 9. Types of nitrogen surface functional groups: (a) pyrrole, (b) primary amine, (c) secondary amine, (d) pyridine, (e) imine, (f) tertiary amine, (g) nitro, (h) nitroso, (i) amide, (j) pyridone, (k) pyridine-N-oxide, (l) quaternary nitrogen. *Reproduced from* [15].**

adsorption capacity where its use continues today. Activated carbon extended its beneficial adsorption properties as a gaseous sorbent in gas masks in WWI. The typical commercial activated carbons yield surface areas that can reach upwards of 1600 $m^2$ $g^{-1}$ and contain an elemental composition of: 88 % C, 0.5% H, 0.5% N, 1% S, and 6-7% O.[16] Depending on the carbon source, oxygen is typically the most variable component ranging from 1 to 20%.

***Synthesis and Properties of Porous carbons (sans nitrogen functionality)***

Nanoporous carbons having large micropore volumes, i.e. activated carbons, have been used throughout the centuries for sequestration of various liquids and gases due to their high available surface areas and accessible pores for adsorption. However, most carbons have more than one type of pores, and the introduction of larger mesopores and macropores can greatly increase the diffusion of fluid species towards the adsorption sites on the carbon surfaces. Hence, current research efforts have focused on carbon precursors and synthetic methods that allow for the preparation of carbons with tailorable hierarchical microporous-mesoporous, or microporous-macroporous structures.

To date, the routes to obtain carbonaceous materials use synthetic sources or naturally available biomass precursors. For carbons obtained from either natural or synthetic sources, micropores are introduced by post-synthesis activation methods.[14, 54-57] These methods can involve chemical activation using inorganic bases or salts (KOH, $ZnCl_2$, $H_3PO_4$, etc.) or physical activation ($CO_2$, steam, $O_2$, $NH_3$), and the activation mechanisms are still largely debated because of the formation of radicals and the uncontrolled reactivity of intermediate species at

high temperatures. The proposed mechanisms generally consist of intercalation and/or etching, both of which are dependent on the activating agent and the surface functionality prior to activation. With either physical or chemical activation, the surface area increases until the carbon structure is stabilized or collapses from further activation. Therefore, the porosity of the resultant material can be tailored post calcination via activating temperature, ratio of activating agent to carbon, and reactivity of activating agent.

Activation increases the accessibility and widens any previously existing micropores, which are needed for $CO_2$ capture. The source of the carbon material, in addition to activation conditions, greatly influences the resulting carbon structure and $CO_2$ capture capacity. This section reviews carbon structures derived from precursors without the integration of nitrogen-containing functionality. Post-calcination high temperature activation with anhydrous $NH_3$ further results in the introduction of nitrogen groups into the carbon structure, and for this reason it will be discussed in another section of this chapter.[15, 58]

### Natural Carbon Sources

Adsorbing $CO_2$ using natural carbon sources is an environmentally conscious approach for repurposing biomass products rich in cellulose that would be otherwise discarded. Upon transformation of discarded biomass products into technologically valuable materials, $CO_2$ emission sources are minimized, while simultaneously affording a carbon molecular sieve to remove the excess atmospheric $CO_2$ generated by anthropogenic activities. Raw resources include, but are not limited to corn cobs, stalks left for fodder, nut shells, potato starch, cellulose,

coal-tar, fungus, and sawdust. The pore structure and surface composition vary from each material with all providing the necessary microporous network for adsorption of $CO_2$.[59] The $CO_2$ capture capacities of porous carbons based sorbents and their activation methods are summarized and shown in Table 1. The production of carbon materials from various sources is plentiful and activated carbons exhibit high surface areas for adsorption and separation, although the instance in which these materials are evaluated for $CO_2$ capture has been a more recent tread due to the relevant global climate issue. In 2001, Poston et al. explored the use of commercially available activated carbon for $CO_2$ adsorption. This work reached an important conclusion: $CO_2$ is preferentially and reversibly adsorbed over $N_2$ and $H_2$ at all pressures. The comparison of molecular sieves (porous compounds consisting of inorganic alkali metals and aluminosilicates) with activated carbon revealed that at higher pressures, activated carbon samples have the higher adsorption capacity.[51] This characteristic of carbon is a consequence of the abundance of micropores with widths between 0.70 and 2.00 nm (supermicropores), and of the of diffusion of $CO_2$ molecules into the narrow micropores due to the increased kinetic energy at boiling of $CO_2$ versus $N_2$.[60] This discriminative characteristic for $CO_2$ physisorption elicited further investigation into microporous carbonaceous materials and particularly those that display a uniform distribution of narrow micropores.[61]

For instance, Zheng et al. prepared KOH activated carbon using corncobs as the primary carbon source.[9] The corncobs were pretreated via adiabatic compression up to 1 MPa prior to calcination. Prior to calcination, increasing pressure under isochoric conditions force compression of gas through the pores. For increased porosity KOH was used to activate that carbon with a 4:1 wt. ratio of KOH to carbon, respectively. The resulting carbon consisted of

**Table 1. The $CO_2$ capture capacity and respective activation methods of various carbons.**

| Adsorbent | Activation Conditions | | | | Textural Properties [a] | | | $CO_2$ uptake | Adsorption Conditions | Ref. |
|---|---|---|---|---|---|---|---|---|---|---|
| | Activation Method | Activating agent: carbon [by mass] | Activation temperature [K] | Activation duration [h] | $S_{total}$ [$m^2 g^{-1}$] | $S_{micro}$ [$m^2 g^{-1}$] | $V_{micro}$ [$cm^3 g^{-1}$] | [mmol $g^{-1}$ (wt.%)] | [K (kPa)] | |
| PF resin 1 wt.% EG | $CO_2$ | - | 1073 | - | 1369 | - | 0.51 | 2.46 (10.8 %) | 298 (100) | [62] |
| PVDC | $N_2$ | - | 1073 | - | 1135 | - | 0.408 | 4.2 (18.5 %) | 303 (100) | [63] |
| PFA/SBA-15 | KOH | 4 | 973 | 1 | 1820 | 1590 | 0.71 | 3.4 (15.0 %) | 298 (100) | [64] |
| CER/MgAc | None | - | 1173 | 2 | 1195 | - | 0.399 | 3.73 (16.4 %) | 298 (100) | [65] |
| TC-EMC | None | - | 973 | 15 | 3840 | - | 1.8[b] | 3.3 (14.5 %) | 298 (100) | [66] |
| ZTC-Y-FAU | Ar | - | 1173 | 3 | 3420 | - | 1.47 | ~2 (8.8 %) | 273 (100) | [67] |
| Eucalyptus sawdust | KOH | 2 | 873 | 1 | 1260 | 1230 | 0.55 | 4.8 (21.1 %) | 298 (100) | [68] |
| Coal tar pitch spheres | Steam | - | 1123 | 2.5 | 1205 | 921 | 0.51 | 1.12 (4.9 %)<br>5.5 (24.1 %) | 303 (15)<br>303 (710) | [69] |
| Olive stones<br>Almond shells | $CO_2$ | - | 1073/973 | [c] | 830/909 | - | - | ~4 (17.5 %) | 303 (100) | [70] |
| Sugarcane bagasse | Zn | 1 | 773 | 1 | 923 | - | 0.528 | 1.54 (6.8 %) | 303 (100) | [71] |
| Coconut shells | $H_3PO_4$ | 2 | 873 | 2 | - | 1922 | 0.68 | ~1.6 (7.0 %) | 298 (100) | [72] |
| Fungus (*Agaricus*) | KOH | 1 | 973 | 1 | 1600 | 1551 | 0.66 | 3.5 (15.4 %) | 298 (100) | [73] |
| Corncob | KOH | 4 | 1073 | 1 | 2789 | - | 1.37 | 3.56 (15.7 %) | 300 (100) | [74] |

[a] $S_{total}$: BET surface area; $S_{micro}$: micropore surface area; $V_{micro}$: micropore volume. [b] Total pore volume. [c] Activated until 40% burn off.

honeycomb-like channels and granular material, shown in Figure 10, attributing the increased surface area from cited to these granules.[9, 75] Wang illustrated that by varying temperature and pressure conditions, the heat of adsorption changes with the loading on the carbon surface. Heterogeneity due to granules causes a plateau where adsorption capacity is reached. With a very large surface area, this material reached a $CO_2$ capture capacity of 3.56 mmol $g^{-1}$ at 1 atm and 28 $^{o}C$. Full utilization of the adsorption sites is still limited by the diffusion kinetics to the sites eligible for adsorption with respect to time according to modeled data.

Furthermore, Chen chemically activated carbons from coconut shells using nitrogen, KOH, or $H_3PO_4$.[72, 76] The final specific surface areas and micropore volume varied according to the activation method, consequently affecting the final $CO_2$ adsorption capacity of each tested sorbent. All samples showed a pore size distribution in the supermicropore region, with the sample activated with $H_3PO_4$ having the highest volume distribution in this region. The $CO_2$ adsorption capacity was ~1.6 mmol $g^{-1}$ at 1 atm and 25 $^{o}C$, the highest reported for coconut shell based sorbents.

The coconut shell activated with phosphoric acid exhibited a specific surface area of ~ 250-300 $m^2 \cdot g^{-1}$, greater than that for the carbons produced from the same material using nitrogen or KOH as an activating agent. As previously mentioned, the specific surface area from the activated carbons relies on the activation agent, temperature, time, and ratio of the carbon to the activation agent.[77] The resulting carbon from the activation with phosphoric acid produced sorbent with higher microporosity and higher selectivity for $CO_2$. It should be noticed that a higher weight ratio of $H_3PO_4$ to carbon was required than of alkali to carbon used for KOH activation. At high impregnation ratios, however, it has been found that $H_3PO_4$ introduced

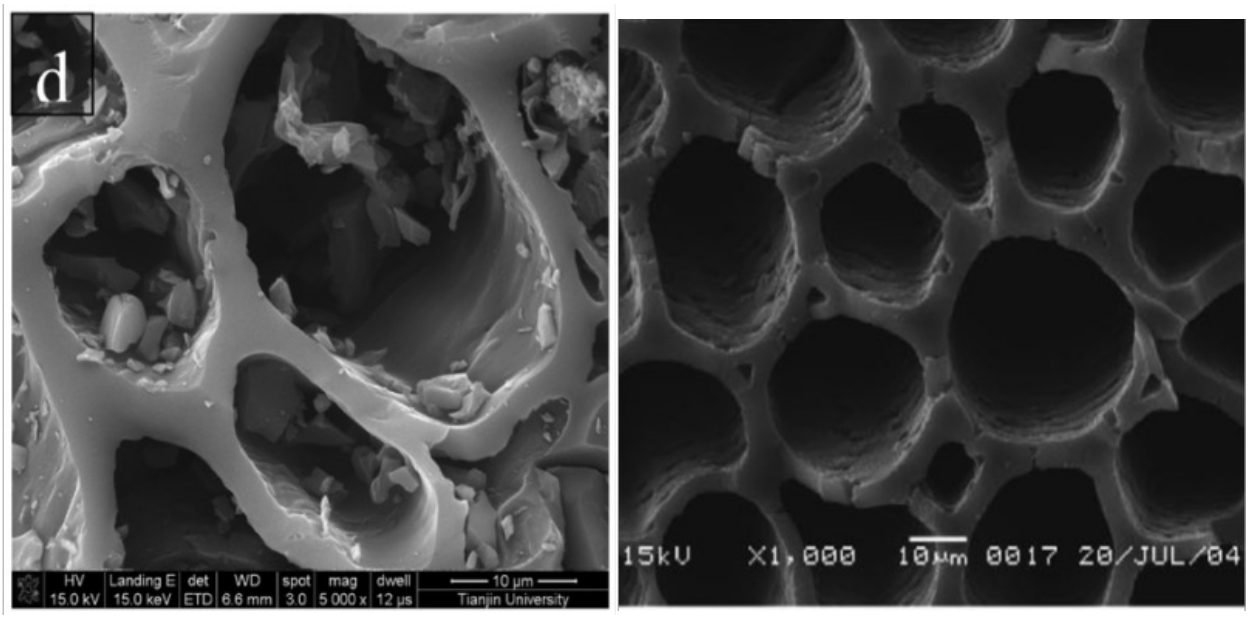


**Figure 10. Activated carbon from corncob carbon source with comparison of (left) with isochoric pressure pretreatment, and (right), without pressure pretreatment. Both were activated using a 4:1 KOH to carbon weight ratio.** ***Reproduced from*** **[9]** ***(left) and*** **[10]** ***(right).***

functional surface phosphate groups to the raw material.[78] Conversely, KOH activation proceeds through the intercalation of $K_2O$ above 400 $^oC$ within the carbonaceous frameworks. The latter is eventually reduced into metallic potassium upon reaction with carbon at increased temperatures, and subsequently etched with acid washing after activation.[56] Consequently, this harsh activation mechanism involving KOH generates large amounts of micropores and consequently high surface areas than similar ratios of $H_3PO_4$.[78] The beneficial changes in surface area, pore width, and carbon yield are limited to optimum ratios, beyond which the adsorption properties and carbon yield decrease with higher KOH to carbon ratios due to excessive etching of the carbonaceous frameworks.

Activation using KOH has been done with several other naturally occurring carbon sources. The fungus, *Agaricus*, was first calcined and then activated using KOH by Kaskel, where an equal ratio of carbon char to KOH achieved the greatest $CO_2$ capture capacity.[73] As seen in the pore size distribution shown in Figure 11, the majority of the pores using this ratio are centered at 0.84 nm in width. The importance of a narrow pore distribution is evidenced by the $CO_2$ capture capacity at 1 atm and 25 $^oC$, which increased from 1.9 mmol $g^{-1}$ for a sample prepared using 5:1 KOH to carbon ratio, up to 3.5 mmol $g^{-1}$ in case of the same carbon activated using a 1:1 ratio. When using activation conditions where the KOH to carbon ratio is high, excessive pore widening occurs, thus broadening the pore size distributions.

Fuertes further illustrated the importance of narrow PSDs using potato starch, cellulose, and eucalyptus sawdust as a carbon sources, all activated with KOH under the same conditions.[68] The eucalyptus sawdust provided smooth, homogenous surfaces that, upon activation, exhibited a narrower PSD in the supermicropore region (distribution maximum ~0.8

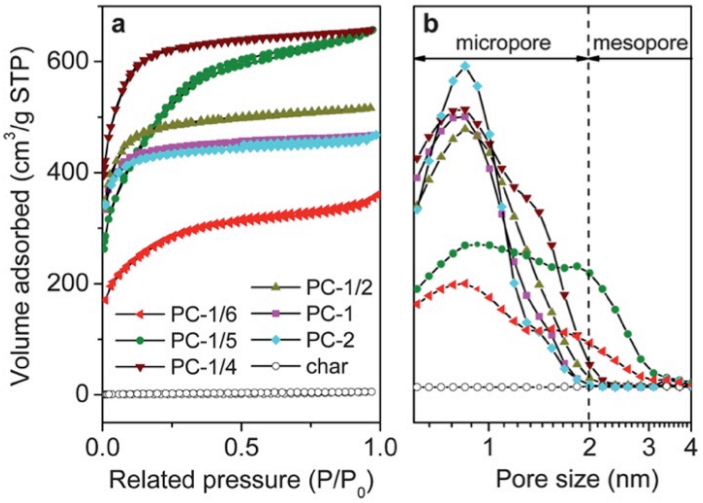


**Figure 11. Nitrogen adsorption isotherms (a) and pore size distributions (b) of fungi-based porous carbons. Char to KOH ratios indicated as shown. *Reproduced from* [73].**

nm). Consequently, the $CO_2$ uptake was as high as 4.8 mmol $g^{-1}$ at 1 atm and 25 $^oC$.

Furthermore, simultaneous calcination and chemical activation in the presence of zinc chloride ($ZnCl_2$) was used by Chidthaisong for sugarcane bagasse derived carbon.[71] The maximum $CO_2$ capture using this carbon source was of 1.54 mmol $g^{-1}$ at 1 atm and 25 $^oC$. This method for activation also widens the micropores of the carbons, similar to KOH activation. In this work, authors prepared composites of activated bagasse carbons with polyethylenimine (PEI) to further increase the $CO_2$ adsorption capacities. Among materials obtained using various ratios of $ZnCl_2$ to carbon, the most dramatic expansion and widening of the pores found for higher quantities of $ZnCl_2$ was proven beneficial when loading PEI. The explanation was based on the fact that PEI blocked the access to small micropores.

In contrast to chemical activation, physical activation utilizes common gases such as $N_2$, $CO_2$ and $H_2O$ steam, and, unlikely the chemical method, it requires no post activation treatment for removal of metals. For instance, Zhang and Ling utilized the physical method with steam to activate anthracites and pitch spheres, reaching $CO_2$ adsorption capacities at 1 atm and 25 $^oC$ of 1.49 mmol $g^{-1}$ and 1.12 mmol $g^{-1}$, respectively.[79, 80] Activation using water vapor relies on the dispersion of $H_2O$ throughout the structure and of its interaction with the carbon surface. The extent of the interaction of the activating gas with the surface determines the extent of micropore formation and widening.[81] With regards to pitch spheres, steam activation was compared to $CO_2$ activation. The $CO_2$ activation produced similar effects as KOH activation by widening the pores due to its high reactivity, in contrast to water vapor, that only increased the volumes of previously existing micropores of a given size (see PSDs in Figure 12). Similar to Ling,[80] Pevida and coworkers performed $CO_2$ activation of olive stones and almond shells that otherwise

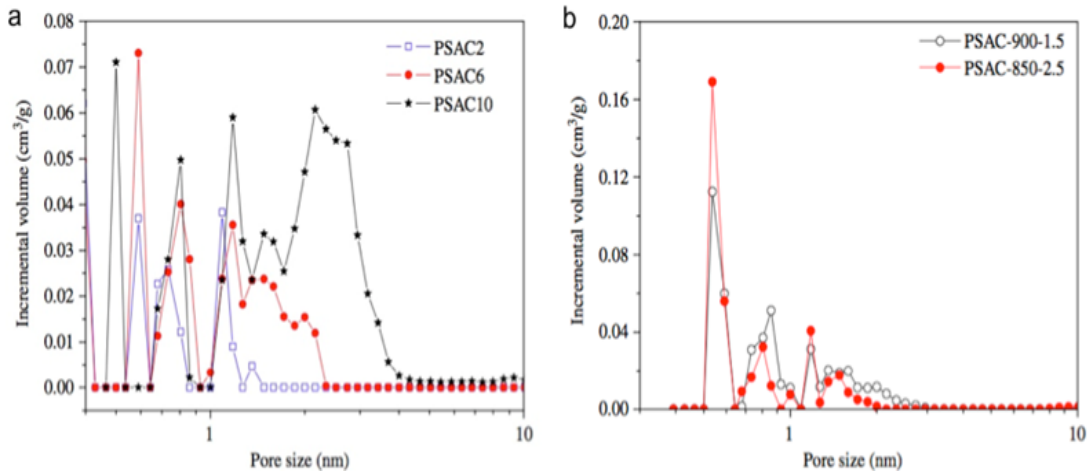


**Figure 12. Pore size distributions for pitch sphere activated carbon (PSAC) using $CO_2$ activation (a) with the respective time and $H_2O$ activation (b) with the respective temperature and time.** ***Reproduced from [80].***

had negligible initial surface areas.[70] The $CO_2$ capture results from olive stone and almond shell carbons display capacities for $CO_2$ of ~4 mmol $g^{-1}$ at 1 atm and 25 $^oC$. As in the work by Fuertes et al., in which the width of the PSD for KOH activated samples varied with sample source,[68] the efficiency of the $CO_2$ activation and its optimal conditions depend on the carbon precursor used.

### Carbons from synthetic sources and templated materials

As previously discussed, the use of natural precursors offers several advantages to manufacture high surface area carbons. However, the need for well-defined chemical composition, low level of impurities and precise control over the pore structure of carbons required the development of methods involving synthetic carbon precursors and of templates. Typically, the synthesis of carbonaceous materials requires organic compounds capable of forming stable polymeric intermediates, or polymers with high char yield at elevated thermal treatment temperatures.

For carbon capture applications, Wilson et al. calcined poly vinylidene chloride (PVDC) copolymers which yielded highly microporous framework without further activation methods.[63] The final carbons had specific surface areas > 1000 $m^2g^{-1}$ and although the PSDs for varying molecular weights of the blocks in the PVDC-methacrylate copolymers used were similar, the final $CO_2$ adsorption capacity changed among final samples, with the highest values reaching 4.2 mmol $g^{-1}$ at 1 bar and 25 $^oC$. The author probed the wide $CO_2$ capture capacity distribution using various probe molecules of differing effective diameters, as shown in Figure

13. The results revealed that even although the average diameters of the pores were similar, the access to the pores changed. While all carbons from similar parent material displayed an average pore diameter < 2 nm required for $CO_2$ adsorption, the shape and size of most pores and of the pore openings determined the accessibility of $CO_2$ to the adsorption sites.

In addition to PVDC copolymers, phenol-formaldehyde (PF) resins have also afforded high-char microporous carbons, for which final porosity was influenced by the pH and molar quantities of the resin precursors prior to calcination. PF resins are notorious thermosets, where heat-induced crosslinking gives them adhesive properties.[82] The calcination of polymer resins produces highly microporous disordered structures in the absence of templates.

In order to further increase the porosity of the PF-based carbons, Pevida and coworkers used both the novolac (PF resin prepared in acidic conditions) and resol (PF resin prepared in basic conditions) with ethylene glycol (EG) or polyethylene glycol additives, and subsequent $CO_2$ activation.[62] The characterization revealed that the additive, EG in particular, generated additional micropores due to the elimination of the free EG molecules with increased temperature during the calcination process. The sample using 1 wt.% EG yielded the maximum surface area and the narrowest micropore size distributions. Both parameters combined equated to the highest adsorption capacity (2.46 mmol $g^{-1}$ at 1 bar and 25 $^{o}$C) in this series of samples. Increasing the mass ratio of additive to carbon precursor decreased microporosity in the calcined structure. This may be attributed to agglomeration of the EG or PEG that is accounted for the formation of mesopores, not apparent in the samples prepared without additives. Although mesopores provide a means of mass transport for increased access to microporous regions, the decrease observed in the microporous contents of the carbons lead to lower $CO_2$ adsorption

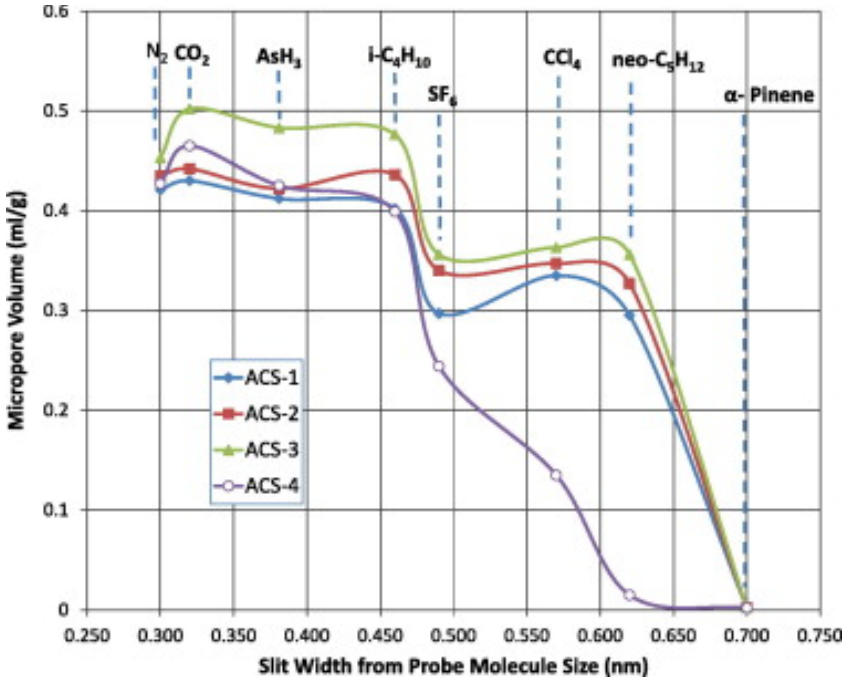


**Figure 13. Micropore volumes using probe molecules to estimate accessible pores.** ***Reproduced from*** **[63].**

capacity. For uniform adsorption, the increased interaction between the additive and the polymer network is essential for mixtures resulting in carbonaceous materials to have high microporosity.

As previously demonstrated, the reliance on interactions between the surface and the adsorbent expresses the need for a uniform surface with narrow pore size distribution. Synthetic block copolymers may undergo phase organization, and the separation of blocks, in which one type of the blocks is a thermoset and the others decompose, can induce some structural regularity to the final carbon materials; otherwise a template with uniform dimensions or lyotropic liquid crystalline phases must be used to transfer its properties to a carbon precursor and consequently the final carbons. Templating agents are categorized as “hard” for solid-state materials, mostly inorganic, or as “soft”, for soft-matter with liquid-crystalline properties, being organic in origin. Hard templating commonly involves the use of nanoporous silicate zeolites,[83] mesoporous silicas,[84] and nonporous silica colloids,[85] whereas alkyl-ammonium salts and block copolymer surfactants are commonly used as soft-templates.

Commercially available zeolites are commonly used template microporous inverse carbon replicas, corresponding to Figure 14. After the in-situ polymerization and calcination of precursors inside the microporous channels of various types of zeolites and dissolution of the silicates, a microporous carbon inverse replica of the starting template is obtained. While the pores of the siliceous template determine the geometry and thickness of the carbon pore walls, the carbon pores are dictated by the silicate pore wall thickness. For instance, when ordered mesoporous silicas, i.e. MCM-48 and SBA-15, with large mesopores are used as templates, carbons with thick pore walls with geometries resembling the pores of the starting templates, and mesopore widths comparable to the silica pore wall thickness are obtained.[64, 84, 86-88] The

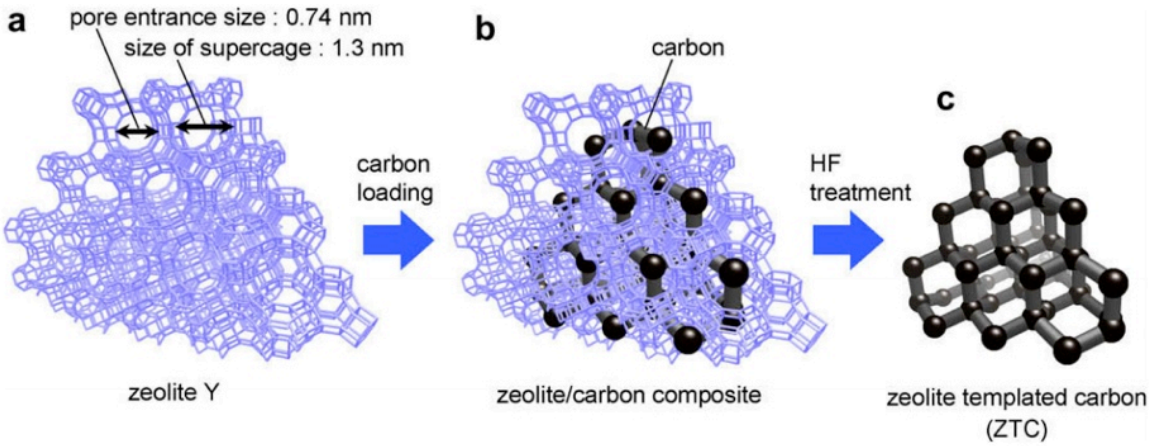


**Figure 14. Typical inverse carbon replica produced using zeolite – Y.** ***Reproduced from*** **[89].**

stability of the final carbon structure depends on the interconnectivity of the micro or mesopores of the templates, and in the successful interconnecting pore filing with the precursors.[87, 88, 90-93] This results in carbon threads interconnecting the larger carbon particles, thus maintaining their intricate porosity.[87, 90, 93] Whereas when larger colloidal silica particles have been used as templates for carbons having large spherical pores, small interconnecting pores are formed by the inability of the precursors used to fill the voids between touching silica particles.[94-97]

Compared to hard-templating, the soft-templating method offers a simpler way to prepare nanoporous carbons that are mostly bimodal because of the nature of the template.[98-103] The block or triblock copolymer templates used undergo microphase separation forming micelle structures.[98-100] Polymer resins as carbon sources provide a foundation for mechanically and chemically stable structures based on cross-linking and utilize non-bonding interactions with the corona of the micelle. Materials produced by Dai et. al[99, 100] provides a model where the hydrophilic blocks of block copolymers used interact with the carbon precursor via enhanced H-bonding, as shown in Figure 15. These reactions may proceed via self-assembly of a pre-polymerized resin-surfactant composite, or and step-growth condensation polymerization of phenolic-formaldehyde monomers and subsequent phase separation of a polymer nanocomposite.[82, 98-103] In an inert atmosphere at temperatures above 723 K, the surfactants are eliminated due to thermal instability, whereas the polymeric resins are calcined.[98-103] The triblock copolymer domains govern the pore size and structure of the resulting carbonaceous structures.

Both hard and soft-templating methods offer a wide selection of starting precursors available and structural properties to be transferred to the final carbons. The selection of the

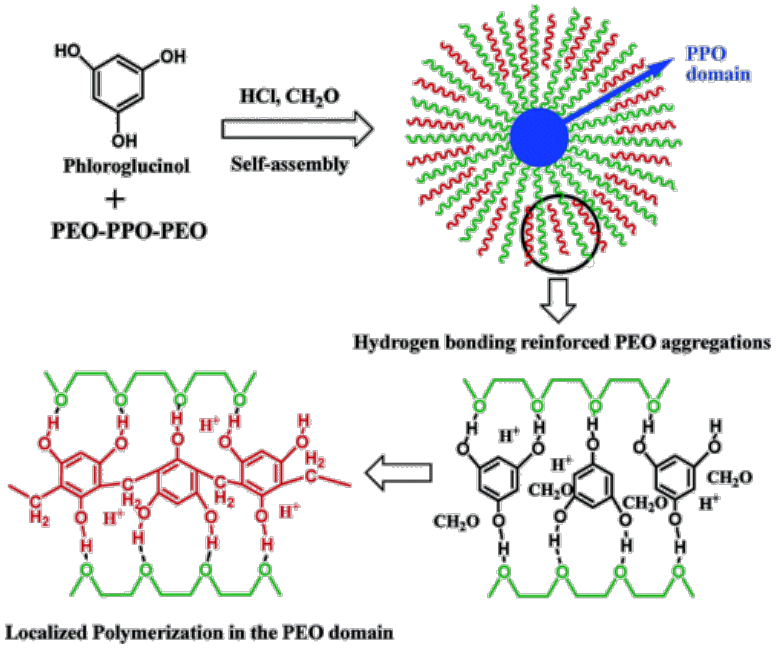


**Figure 15. Soft-template synthesis using triblock copolymer (Pluronic F127) with localized polymerization of phenolic-formaldehyde resin. *Reproduced from* [99].**

precursor is based on its ability to fill the pores of a hard-template, or favor the formation of a specific mesophase with a given surfactant in the soft-template. A combination of conditions and methods can be implemented to further tailor the pore size and structure.[104]

For instance, furfuryl alcohol is commonly utilized for hard templating techniques, which utilize inorganic siliceous architectures.[64, 67] Two zeolites were used as templates, namely EMT and Y-FAU shown in Figure 16**.** The former framework is formed by interconnected cages leading to a straight pore channel system running along the crystallographic *c*-axis, different to that of the zeolite Y, which displays a 3D system of interconnected cages. The microporous carbons obtained from both zeolites had extremely high surface areas (>3500 $m^2 \cdot g^{-1}$), and a bimodal distribution of micropores centered at 0.5 and 1.2 nm. The carbon pore walls of the EMT inverse replica consisted of a cubic system of interconnected carbon particles, with pore widths consistent with the cage-like structure of the template. The smaller pores, however, restricted the mass transport and adsorption of $CO_2$. In comparison, the carbon inverse replica of zeolite Y-FAU exhibited a simpler 3D cubic pore structure that permitted better $CO_2$ diffusion and adsorption at higher pressures (~2 mmol $g^{-1}$ at 0 $^oC$ and 1 bar).

Although the use of hard templating has provided a direct route to tailor pore size and shape, the economic, environmental, and industrial scale viability is still under heavy scrutiny. This is because of the high cost and time required for preparing the hard-templates and their dissolution using hazardous fluoridric acid and sodium hydroxide.

In order to overcome such drawbacks, Park et al. described using Mg acetate (MgAc) as a templating agent for Amberlite® cation exchange resin (CER).[65] After calcination, neutralization and washing, nitrogen adsorption isotherms indicated delayed capillary

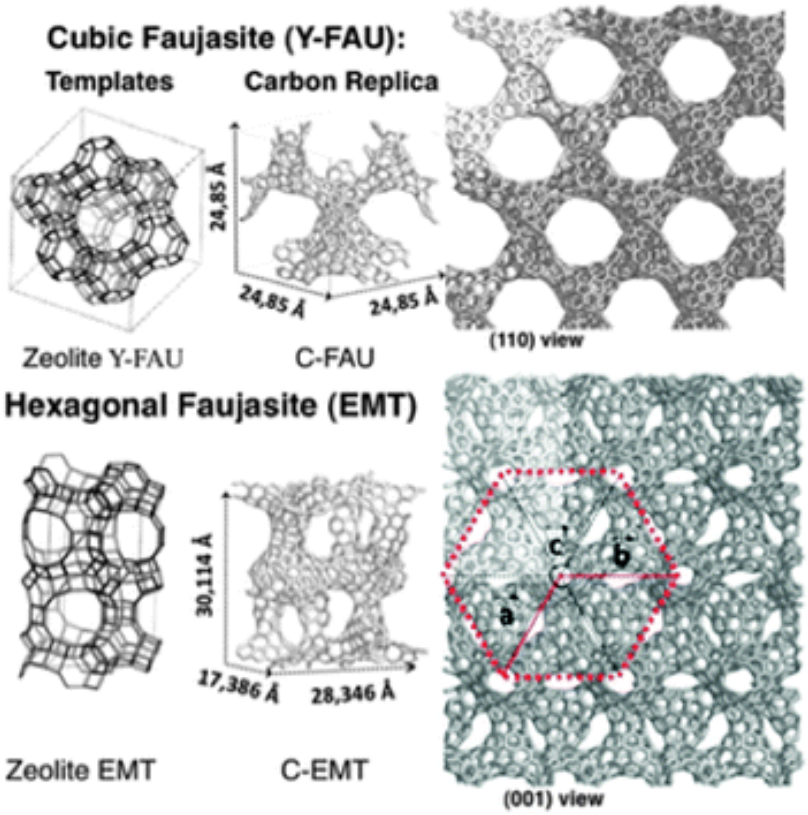


**Figure 16. Unit cell atomic structures examining zeolite Y-FAU (top left), its corresponding inverse carbon replica (top middle), and its duplicated form (top right). Unit cell of zeolite EMT (bottom left), its corresponding inverse carbon replica (bottom middle), and its duplicated form (bottom right). *Reproduced from* [67].**

condensation due to a broad distribution of mesopores. Micropores formed by intermediate individual MgO particles and small particle agglomerates. By increasing the MgAc to CER ratios, higher surface areas were achieved, whereas at high ratios, the mesopores collapsed. The sample with a ratio of 2:1 MgAc to CER provided a thick enough carbon coating onto the surface of the Mg-template to uphold the structural integrity of micropores and mesopores after calcination under $N_2$ at 900 $^oC$ and template removal using a dilute HCl solution. The bimodal porous structure with a high volume of micropores had a 3.73 mmol $g^{-1}$ $CO_2$ uptake at 1 bar and 25 $^oC$.

Finally, soft-templated carbons also provide a more environmentally friendly approach to porous carbons, simplifying the production compared to the hard-templating method, and by utilizing largely available precursors and templates. Although there have been a few works, such as those by Lu[49, 105] and Yuan,[106] using soft templating for carbons with N containing compounds for $CO_2$ capture in particular, $CO_2$ capture studies using soft templating without nitrogen functionality are sparse. Soft-templated carbons exhibit well-defined mesopores and relatively low micropore volumes, thus requiring activation steps. Ordered mesoporous materials however, have been cited for use in separations due to ability to prepare monolithic structures and free-standing membranes,[107] to replace toxic formaldehyde with glyoxal,[108] and to the ability to enlarge the mesopore sizes using carbon black and onion-like carbons.[109] Due to their large surface areas and good thermal, mechanical and chemical stability, and improved mass transport through its wide and accessible mesopores, soft-templated carbon materials are promising for future developments of sieves for carbon capture technologies.

***Synthesis and Properties of N-doped Porous carbons***

Although activated carbon adsorbents encompass desired attributes for potential CCS applications like hydrophobicity, reversibility, stability and low-energy requirements for regenerating the adsorbents, their $CO_2$ capture capacities are relatively low compared to some of other materials. In order to improve its $CO_2$ separation performance, accessible nitrogen modified basic sites can be introduced to porous carbon walls.

Recent research studies have demonstrated that the interaction between $CO_2$ molecules and nitrogen-enriched porous carbon materials occurs via strong binding interactions like dipole-dipole interactions,[48] acid-base interaction[49, 110] and hydrogen bonding[53] between $CO_2$ molecules and the nitrogen-modified heterogeneous pore walls. Hence, the surface modification of carbon frameworks significantly improves the $CO_2$ affinity of the resulting N-doped adsorbents.

Based on the different precursor sources, two different strategies have been developed to generate such N functionalities: 1) high temperature activation using N-containing volatile compounds (i.e. amination and ammoxidation)[111] and 2) the use of N-based organic molecules and polymers as carbon precursors. For most N-containing sources, hard-templating and activation methods have been widely used to create N-doped porous carbons. The surface area of the resulting carbons can be largely increased by either chemical or physical activation using KOH and $CO_2$.[112]

***Post-synthesis functionalization of porous carbon***

In view of the two key properties for high $CO_2$ adsorption capacity, the latter has been achieved by post-synthesis high-temperature treatment with ammonia or acetonitrile. This method has been found to introduce N-basic sites to the carbon surfaces.[66, 113] In this way, N-doped OMCs treated at 1000 °C exhibit enhanced $CO_2$ uptake with a $CO_2$ capture capacity of 3.46 mmol $g^{-1}$at 25 °C. A remarkable $CO_2$ capacity (4 mmol $g^{-1}$ at 1 bar and 25 °C) and selectivity ($CO_2/N_2$ at 1 bar = 14) was recently obtained for zeolite-templated porous carbon treated with acetonitrile.[66]

The post-synthesis activation provided improved $CO_2$ adsorption by modifying the chemical composition of the surfaces, while simultaneously activating the OMCs when ammonia was used in the process. Consequently, the interaction energies with $CO_2$, as approximated by the isosteric heats of adsorption, increased from 30 kJ $mol^{-1}$ by unmodified carbons to as high as 50 kJ $mol^{-1}$ for N-doped materials.[66] Different $CO_2$ capture performance of N-doped carbons and their isosteric heats of adsorption are summarized in Table 2.

Despite the many beneficial impacts to the $CO_2$ adsorption capacities of these carbons, the post modification introduces complex and time-consuming synthetic steps, which may limit the CCS large-scale application. Hence, more straightforward methods to obtain functional porous carbon materials are of great importance for practical uses.

**Table 2. The $CO_2$ capture capacity and isosteric heats of adsorption of N-doped carbons.**

| Adsorbents | Conditions T /°C (P=1 bar) | Isosteric heat of adsorption kJ $mol^{-1}$ | $CO_2$ uptake Capacity mmol $g^{-1}$ (wt. %) | Ref. |
|---|---|---|---|---|
| RN800 | 25 | - | 2.18 (9.6%) | [113] |
| N-TC-EMC | 25 | 33-50 | 4.0 (17.6) | [66] |
| CN-sphere | 25 | - | 2.25 (9.9%) | [114] |
| MCN/C | 0 | | 3.05 (13.4%) | |
| | 25 | - | 2.35 (10.3%) | [115] |
| RFL-500 | 25 | - | 3.13 (13.7%) | [49] |
| HCM-DAH-1-900-1 | 0 | | 4.9 (21.5%) | |
| | 25 | 19.6-26.7 | 3.3 (14.5%) | [105] |
| 3C-1000N | 25 | - | 3.46 (15.2%) | [106] |
| HMT-80-900 | 0 | | 5.6 (24.6%) | |
| | 25 | - | 4.0 (17.6%) | [116] |
| CP-2-600 | 0 | | 6.2 (27.3%) | |
| | 25 | 18.9-31.5 | 3.9 (17.2%) | [48] |
| a-NDC-6 | 25 | - | 4.3 (18.9%) | [117] |
| ACM-5 | 0 | | 11.51 (50.6%) | |
| | 25 | 65.2 | 5.14 (22.6%) | [118] |
| SK-0.5-700 | 25 | - | 4.24 (18.7%) | [53] |
| NPC10 | 25 | - | 3.2 (14.1 %) | [119] |
| CN500 | 0 | 29.6-32.1 | 4.39 (19.3%) | [110] |
| $C_{RHC221\text{-}DES}$-800 | 25 | | 3.3 (14.5%) | |
| | 50 | 26-32.7 | 2.3 (10.1%) | [120] |

#### *1.1.1.1 Synthesis of N-doped carbons from N-containing polymeric precursors*

From N-containing polymer sources, N-doped porous carbons can be prepared from either a hard-templating method or by means of a simple calcination-activation process. These methods have also permitted the fabrication of not only N-doped but of N-rich compounds such as carbon nitride ($CN_x$). For instance, graphitic carbon nitride (g-$C_3N_4$) is a well-known and fascinating material with application potential in many fields such as catalysis due to its pyrrolic N functionalities.[68] Other forms of $CN_x$ materials, including amorphous phases, are also desired due to their high N-contents and higher surface areas compared to bulk g-$C_3N_4$.

In general, $CN_x$ based materials applied for $CO_2$ capture display high adsorption capacities.[114, 115] Examples include the $CO_2$ adsorption of a nitrogen-enriched $CN_x$ spheres. These were prepared via calcination of a melamine and formaldehyde resin through a nanocasting pathway by using spherical mesoporous cellular silica foams as a hard-template, and the $CO_2$ adsorption capacity reached 2.25 mmol $g^{-1}$ at 25 °C.[114] In order to avoid the use of toxic reagents such as NaOH and HF for etching the siliceous templates, direct synthesis methods for porous $CN_x$ materials for $CO_2$ separation processes are preferred. Also, the development of synthetic methods to obtain composites with morphologies other than powders, i.e. monoliths and films, are desired. Figure 17 shows a direct synthesized N-doped carbon monolith prepared by direct pyrolysis of the copolymer of resorcinol, formaldehyde and lysine.[49] The resulting adsorbent shows a maximum $CO_2$ adsorption uptake of 3.1 mmol $g^{-1}$ (1 atm and 25 °C) with good recyclability. Increased $CO_2$ separation performance may be attributed to the enhanced affinity between $CO_2$ molecules and incorporated N anchors inside the

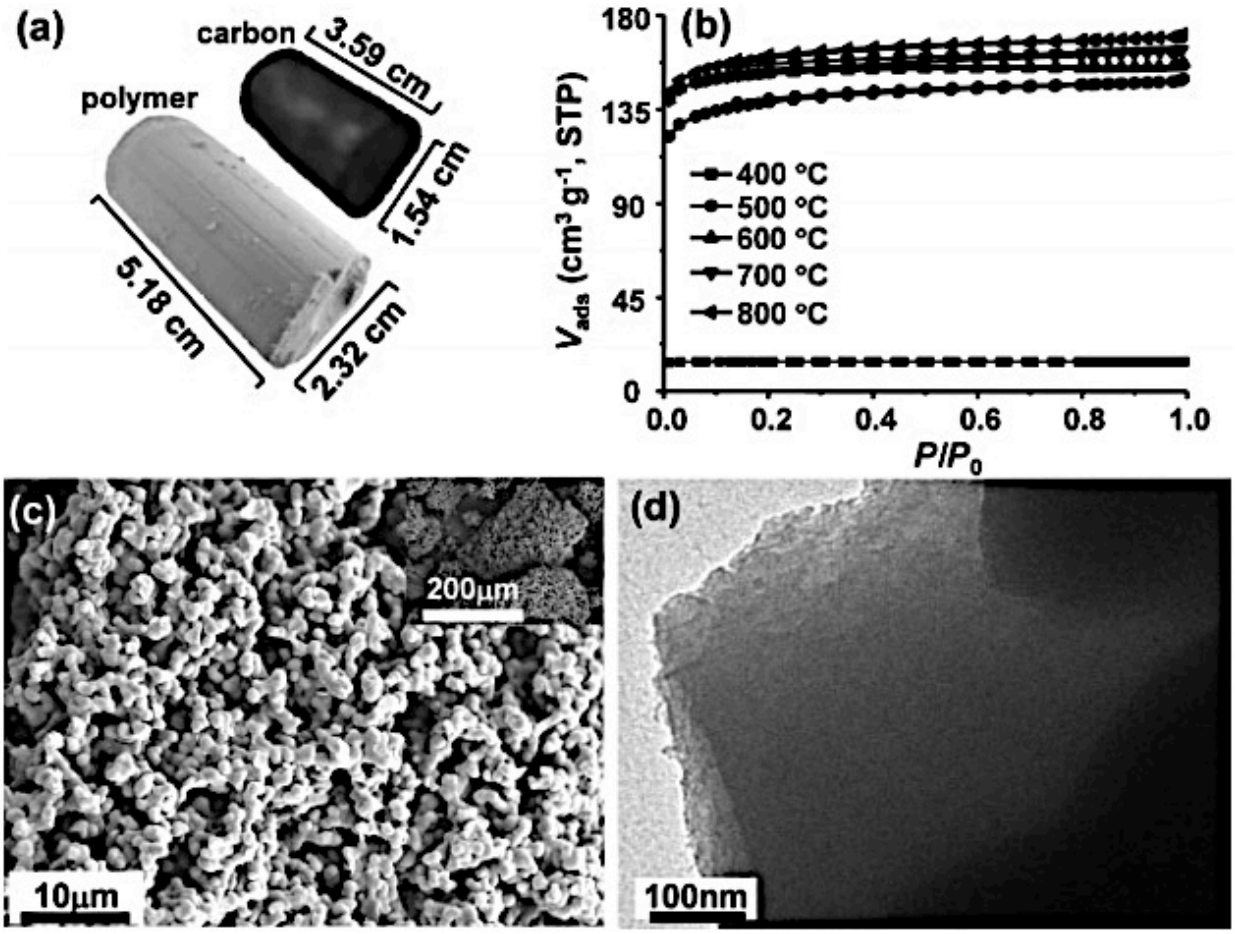


**Figure 17. N-doped carbon monolith prepared by direct pyrolysis of the copolymer of resorcinol, formaldehyde and lysine. *Reproduced from* [49].**

carbonaceous framework. A series of N-doped hierarchical porous carbons through the self-assembly of poly (benzoxazine-co-resol) with defined hierarchical pore structures and high mechanical strength were also prepared (Figure 18).[105]

These carbon monoliths display outstanding $CO_2$ capture capacities, high selectivity for separations, and facile regeneration at room temperature. At ~1 bar, the equilibrium capacities were in the range of 3.3–4.9 mmol $g^{-1}$ at 0 °C and of 2.6–3.3 mmol $g^{-1}$ at 25 °C, while the dynamic capacities are in the range of 2.7–4.1 wt. % at 25 °C using 14 % (v/v) $CO_2$ in $N_2$. The carbon monoliths also exhibited high selectivity for the capture of $CO_2$ over $N_2$ from a $CO_2/N_2$ mixture, with a separation factor ranging from 13 to 28.[105] However, this method required toxic organic amines or of formaldehyde as precursors.[106] Thus, in view of the green and easy synthesis, Lin et al. used hexamethylenetetramine both as carbon precursor instead of formaldehyde solution and as nitrogen source to synthesize the N-doped adsorbents.[116] Mainly due to the presence of nitrogen-containing groups and a large amount of narrow micropores (<1.0 nm), the resulting microporous carbons show a good capacity to store $CO_2$. At 1 Bar, the equilibrium $CO_2$ capture capacities of the obtained N-doped carbons were in the range of 3.9–5.6 mmol $g^{-1}$ at 0 °C and 2.7–4.0 mmol $g^{-1}$ at 25 °C.[116]

Similar to other carbon sieves, the $CO_2$ capture capacity of nitrogen functional materials having high densities of N-groups are dramatically improved by high specific surface areas and narrow micropore size distributions. In order to increase the surface area of N-doped carbons, chemical KOH activation has been applied for the synthesis of N-doped sorbents from polypyrrole (PPy) as precursor. As expected, a very high $CO_2$ adsorption uptake of 6.2 mmol $g^{-1}$ (0 °C) and 3.9 mmol $g^{-1}$ (25 °C) were achieved for porous carbons prepared with KOH/PPy = 2

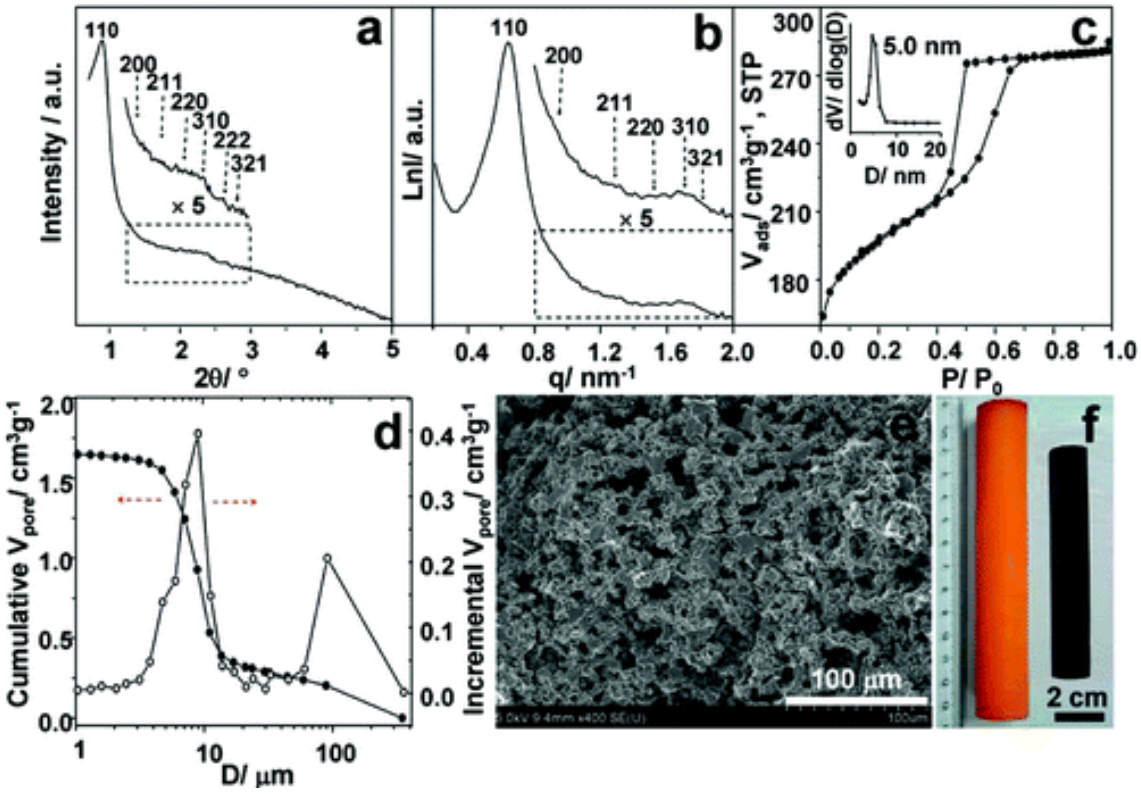


**Figure 18. A series of N-doped hierarchical porous carbons through a self-assembly of poly(benzoxazine-co-resol).** ***Reproduced from*** **[105]**

and 600 °C ($S_{BET}$ = 1700 $m^2 \cdot g^{-1}$, pore size ≈ 1 nm and 10.1 wt.% N), respectively.[48] The strong interactions between the larger quadrupole moment of $CO_2$ molecules compared to $N_2$, and the polar sites associated to N groups may account for the enhanced $CO_2$ affinity over $N_2$ in gas mixtures. This is supported by the higher calculated isosteric heat of adsorption for $CO_2$ of 31.5 kJ $mol^{-1}$.[48]

Additionally, Chandra et al. prepared N-doped carbon by KOH activation of PPy functionalized graphene sheets.[117] Graphene is a two dimensional material with hexagonal arrangement of $sp^2$ hybridized carbons.[121-124] This material displays high intrinsic electrical conductivity, large theoretical specific surface area, high mechanical strength and high chemical stability.[121-124] The $CO_2$ adsorption experiments demonstrated a capacity of 4.3 mmol $g^{-1}$ at 25 °C and 1bar, which is approximately 10% higher than the 3.9 mmol $g^{-1}$ for the aforementioned activated PPy adsorbents.[117] Despite the improvements achieved using PPy-based carbons, the toxicity of the pyrrole monomer makes it difficult to handle and restricts its application to $CO_2$ adsorption at the industrial level. In addition, extra preparation steps are introduced for the activation using harsh chemicals such as KOH, besides generating neutralization streams.

In order to make greener polymer-based porous carbons, physical activation using $CO_2$ was used with commercially available polyacrylonitrile (PAN) in a two-step thermal treatment process (Figure 19).[118] These ACMs exhibit the highest $CO_2$ capture recorded among all activated carbons reported so far. At ambient pressure, an exceptionally high $CO_2$ uptake of 5.14 mmol $g^{-1}$ at 25 °C and of 11.51 mmol $g^{-1}$ at 0 °C were achieved. A high isosteric heat of adsorption value of 65.2 kJ $mol^{-1}$ indicate the strong adsorbent-adsorbate interaction between the

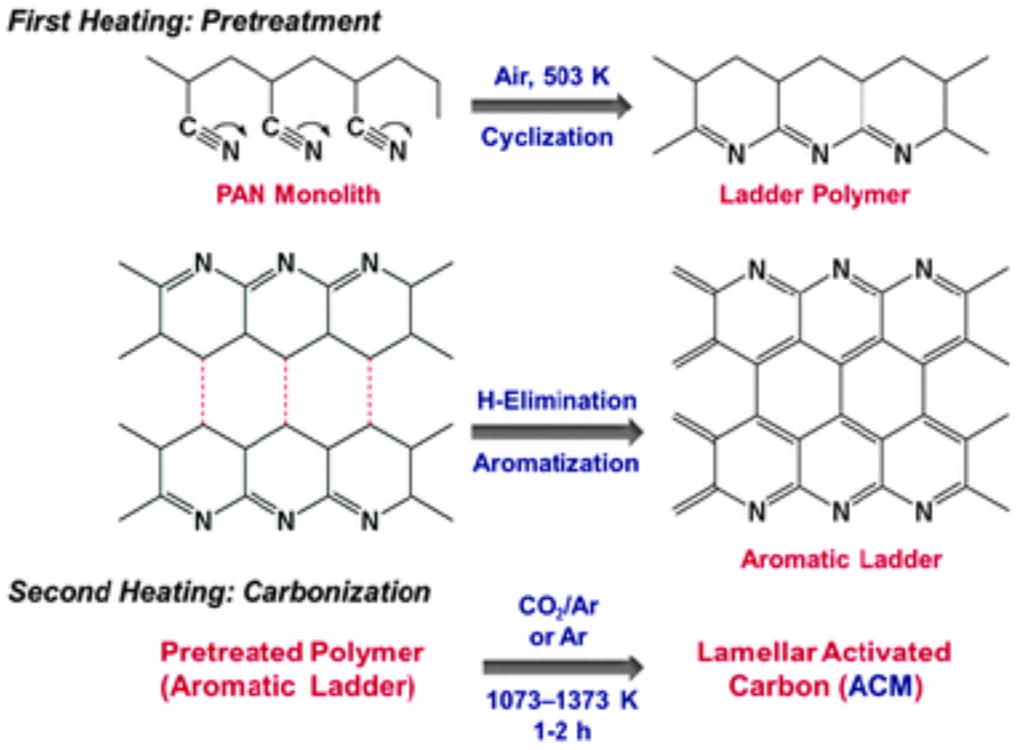


**Figure 19. Calcination of PAN monolith and $CO_2$ activation in a dual step thermal treatment process to obtain activated N-doped carbon monoliths.** ***Reproduced from [118].***

N-containing carbon framework and $CO_2$ molecules.[118] Nonetheless, this value is well below the typical energy for covalent bonds and hence the adsorption process is reversible.

Considering the environmental issues and of cost implications of utilizing petro-based resources, largely available N-containing biomass sources are becoming increasingly important and considered to be more competitive for the synthesis of $CO_2$ capture adsorbents.[53, 119] Recently, Xing et al. demonstrated that the N-doped activated carbons prepared from bean dreg, a N-containing biomass waste, interacted with $CO_2$ by strong hydrogen bonding interactions. The $CO_2$ adsorption of this carbon was 4.24 mmol $g^{-1}$ at 25 °C and 1 bar, which is larger than most N-containing polymer-based carbons.[53] This finding further challenges the long-field viewpoint that acid-base interactions between N-containing basic functional sites inside the carbon framework and the acidic $CO_2$ gas are responsible for the enhanced $CO_2$ capture capacity of N-doped carbons.

Research on other biomass waste products rich in nitrogen and the development of green processing techniques can increase interest on biomass-derived sorbents for industrial applications. These materials may further extend our current knowledge on the interactions between fluids and functionalized porous surfaces, due to the vast number of naturally occurring compounds and the carbonaceous compounds that could be obtained.

***N-doped carbons from fluidic precursors***

In addition to presenting several advantages such as negligible vapor pressures, non-flammability, and good thermal stability,[125] ionic liquids (ILs) have been used as precursors

for nanoporous carbons.[55, 126-130] ILs are defined as a combination of an organic cation and an inorganic anion that melt at temperatures near 100 $^{o}$C.[131, 132] While typical n-alkyl imidazolium IL compounds require hard-templates to induce a carbon yield,[126-128] ILs with cross-linkable functional groups, namely task specific ionic liquids (TSILs),[55, 129, 130] are directly converted into nanoporous carbons. The latter carbons exhibit slit-like pores,[55] formed via thermal polymerization of a cation or anion having one or more nitrile groups, followed by subsequent calcination without hard-templates.[55, 129, 130] The pores are voids from the non-cross linked counter ions. Hence, in this self-template process, the pore sizes and pore volumes are essentially determined by the size of the decomposing ion. In addition, TSILs further allow for the preparation of graphitizable carbons with enhanced electronic conductivity,[128] as well as of heteroatom-doped carbons such as nitrogen[55, 128-130] and boron[55] with their ratios in the carbon materials controlled by their amounts initially present in the cross-linkable ions.[133]

When tested for gas separations, the porous nitrogen-doped carbons (CNs) prepared from nitrile groups functionalized TSILs (Figure 20),[110] displayed exceptional $CO_2$ adsorption capacity of 4.39 mmol $g^{-1}$ at 0 °C and 1 bar. This results from the strong interactions between $CO_2$ molecules and abundant numbers of nitrogen containing groups in these frameworks, which exhibited an isosteric heat of adsorption value of 32.1 kJ $mol^{-1}$.[110] Given the simplicity of this method to prepare nitrogen-doped carbons, the use of TSILs as precursors for the preparation of tailor-made porous adsorbents opens interesting avenues in the area of carbon capture.[134]

Furthermore, deep eutectic solvents, a new class of IL obtained by complexion of quaternary ammonium salts with hydrogen bond donors such as acids, amines, and alcohols among others. Recently, the latter have also been used as both precursors and as structure

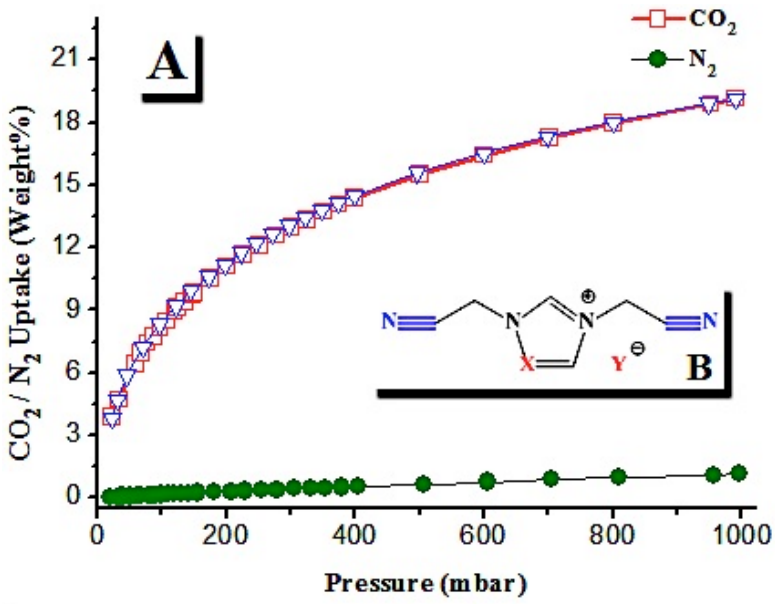


**Figure 20. $CO_2/N_2$ adsorption of CN500 at 0 °C. Inside B: Chemical structure of nitrile functionalized task specific ionic liquids.** ***Reproduced from [110]***

directing agents in the synthesis of nitrogen-doped carbons with high $CO_2$-adsorption capacities (up to 3.3 mmol $g^{-1}$ at 25°C and 1 bar).[135] Further studies may reveal the ability to preparing N-doped carbons with higher surface area using DESs or TSILs by turning the cations or anions.

## 2.4 Conclusion

Analysis of carbon structure through gas adsorption measurements and modeling provide the necessary characteristic information for evaluation of the materials as $CO_2$ adsorbents. The carbon-based adsorbents have progressed from simple activated cellulosic biomass materials to designed task specific ionic liquid based sorbents having tailorable pores and surface composition for optimum $CO_2$ capture performance. Such advancements have come at an opportune time, when innovation is fueled by an increasing demand to effectively sequestrate $CO_2$ from the atmosphere along with separating it from natural gas and other potential future fuel sources.

# CHAPTER 3. EXPERIMENTAL MEASUREMENTS AND DATA PROCESSING

The preparation of mesoporous carbon consists of the polymerization, drying, calcination and, if applicable, activation. In this work, the carbon precursor is synthesized by step-growth polymerization of a phenolic precursor and an aldehyde cross-linker. Prior to the addition of the cross-linker, the templating agent is added for dissolution. The combination of the phenolic aldehyde cross-linker will be referred to as the "phenolic resin". The interaction of the phenolic resin with the polymer templating agent varies with molecular weight of either component thus *in situ* polymerization conditions can greatly vary the phase separation parameters, which includes but is not limited to: concentration of reactants, reaction time, reaction temperature, stirring speed (related to the increasingly progressive viscosity), and pH. Through calcination, analysis of the phase separation progression and surface characteristics can be analyzed using: nitrogen adsorption, scanning electron microscopy (SEM), transmission electron microscopy (TEM), energy dispersive x-ray spectrometry (EDX), x-ray photoelectron spectroscopy (XPS), and small angle x-ray scattering (SAXS), and thermogravimetric analysis (TGA). In this chapter, these methods and associated data processing techniques for evaluating porous carbon.

## 3.1 Isothermal volumetric gas adsorption

Isothermal adsorption measurements of $N_2$ are completed volumetrically using a Micromeritics Tristar and Quantachrome AS-1. Prior to analysis, carbon samples are dried under flowing $N_2$ at 170 $^oC$ until a stable weight is obtained. Adsorption of $N_2$ is completed at 77 K. The adsorption can be interpreted using several model methods and parameters to obtain: specific surface area, micropore surface area, total pore volume, micropore volume, pore size distribution, and average pore size. Furthermore, with the ultra-low pressure capabilities of the Quantachrome AS-1 we can obtain a micropore analysis. The micropore sizes and corresponding histograms using density functional theory (DFT) can detect pore diameters as low as ~0.5 nm. The quantification of pores of this size makes this instrument valuable to $CO_2$ adsorption analysis because of the direct correlation between $CO_2$ uptake and the surface area in the supermicropores (0.5 - 0.7 nm) in addition to qualitatively assessing the contributions of physisorption and chemisorption when analyzing functionalized materials.

## 3.2 Isothermal gravimetric gas adsorption

Isothermal adsorption measurements of adsorption of $CO_2$ and $N_2$ are completed gravimetrically using thermogravimetric analysis (TGA) for analysis of monolithic carbon only and Hiden Isothermal Gravimetric Analyzer (IGA) up to 1 bar. Prior to analysis, the sample is dried under increased temperature and vacuum conditions until a stable weight is reached. Adsorption of both gases is performed under several temperature conditions. The results

obtained using this method provide adsorption capacity, isosteric heat of adsorption, and selectivity. These results provide information that can then be used to predict full-scale industrial utilization of these materials but that is beyond the scope of this research.[136]

Although only single gas gravimetric adsorption measurements can be obtained, the isotherms provide the necessary adsorbent-adsorbate interaction factors like the isosteric heat of adsorption. Temperature dependent variables can be determined in the fitting procedure in addition to the Clausius-Clapeyron equation and Ideal Adsorption Solution Theory (IAST) model.[137-145] Several approaches to fitting the single gas adsorption isotherms can provide these factors.

### 3.2.1 Freundlich Equation

The most popular isotherm fitting equations are the Langmuir equation, the Freundlich equation, the Sips equation, and the Toth equation. The equation developed by Freundlich and others approached the surface of adsorption as heterogeneous and breakdowns the localized singular adsorption sites into "patches" that are independent of one another.[20] The Freundlich equation:

$$n_i^o = KP^{1/m} \qquad (15)$$

where K and n are both temperature dependent. By plotting log($n$) vs. log($P$), the slope yields *1/m* and the intercept = log($K$); although, the purely empirical nature of the variables $K$ and $n$ and the equation represents adsorption directly proportional to pressure restricts the theoretical

presentation and pressure range extrema, respectively; although the Freundlich equation remains commonly used and good fits can be achieved.[14, 146-148]

### 3.2.2 Sips Equation

The combination of both the Langmuir and Freundlich equations resulted in the three parameter Sips equation (Equation 14).[20] The high-pressure deterioration from the Freundlich equation is resolved by integrating the theoretical variables assigned by the Langmuir equation and assigning the *m* parameter to system heterogeneity, which increase with increasing heterogeneity of the system. The Sips model equation:

$$n_i^o = \frac{q_{sat}(bP)^{1/m}}{1+(bP)^{1/m}} \tag{16}$$

where temperature dependence can be introduced to the *b* and *m* parameters through:

$$b = b_0 \exp\left[\frac{Q}{RT_0}\left(\frac{T_0}{T}-1\right)\right] \tag{17}$$

and

$$\frac{1}{m} = \frac{1}{m_0} + \alpha\left(1-\frac{T_0}{T}\right) \tag{18}$$

with reference temperature, $T_0$, sticking constant, α, gas constant, $R$, and adsorption heat, $Q$. The Sips equation is regarded to more accurately fit over a larger pressure range and provide an upper saturation limit, where the Freundlich equation failed; although, at low pressure and coverage, the equation does not reduce to Henry's law but has still aptly applied to carbon materials and is especially useful at high pressures.[20, 149-154] Do examined the mathematical relationship

between $Q$ and isosteric heat, $-\Delta H$, and found the direct relationship at a fractional coverage of 0.5.[20]

### 3.2.3 Toth Equation

The addition of a 3rd parameter in the Sips equation to account for the system heterogeneity would clearly result in increased the fit accuracy but the low pressure region in which Henry's law behavior occurs remains important. The modified Langmuir or Toth equation rectifies this shortfall in this form:

$$n_i^o = \frac{q_{sat} bP}{[1+(bP)^t]^{1/t}} \tag{19}$$

where temperature dependence is found in the affinity constant, $b$:

$$b = b_0 \exp\left[\frac{Q}{RT_0}\left(\frac{T_0}{T}-1\right)\right] \tag{20}$$

and the heterogeneity parameter, $t$:

$$t = t_0 + \alpha\left(1-\frac{T_0}{T}\right) \tag{21}$$

with the sticking coefficient, α, the gas constant, $R$, adsorption heat, $Q$, and reference temperature, $T_0$. In contrast the Sips equation, the Toth equation reduces to Henry's law under low pressure and coverage and when $t = 1$ it reduces to the Langmuir equation. The $t$ parameter in this equation is > 1 and decreases with increasing heterogeneity of the system. Increased accuracy at low pressures compared to other models has been found and proven useful in porous

carbon materials and other porous zeolites.[155-158] The $Q$ corresponds mathematically to $-\Delta H$ at a zero fractional coverage.[20]

### 3.2.4 Error analysis

Several methods are available for error analysis of isotherm fittings were used to evaluate the goodness of fit to the experimental data but by using the sum of squared error (SSE) the best model for fitting can be easily identified by the lowest value.

$$SSE = \sum_{i=1}^{n} (n_{\exp} - n_{fit})^2 \qquad (22)$$

Where $n_{\exp}$ is the experimental value for uptake in mmol $g^{-1}$ and $n_{fit}$ is the uptake value in mmol $g^{-1}$ obtained from the fitting equation at each experimental pressure. The SSE measures the total deviation of the calculated fit values with the obtained experimental values. Fitting the models to the experimental data was done using MatLab by minimizing the SSE. The Matlab code for all the fittings can be found in Appendix B.

## 3.3 Electron Microscopy

Microscopy can provide both quantitative and qualitative information for materials analysis. Pore sizes and uniformity of the sample can be found and examined in a matter of minutes, making this a valuable technique as a sieve for porous samples. Scanning electron microscopy (SEM) uses a focused electron beam to scan across a sample. A variety of electron-

sample interactions occur but, generally, images are composed of secondary electrons (electrons generated from the emitted electrons from the sample. In contrast, transmission electron microscopy (TEM) generates images from a detector that collects electrons that are transmitted through a very thin sample. The images of carbon obtained from these methods provide valuable information about morphology, which, in turn, provide information about the mechanisms occurring during synthesis.

## 3.4 X-Ray Photoelectron Spectroscopy (XPS)

Elemental analysis of surface groups found in mesoporous carbon to quantify adsorption characteristics is done by x-ray photoelectron spectroscopy (XPS). This method can quantify a wide variety of elements (Li to U) in the top 10 nm of a sample, while also revealing and quantifying the chemical environment of the respective element. The sample is bombarded with a known x-ray and contacts the sample where the high-energy x-ray excites and ejects an electron. The emitted electron contains information about its previous residence through its kinetic energy, which is a function of its binding energy.

The x-ray bombardment ejects an electron from the core shell of an atom and can decay through two different processes: photon emission (fluorescence) or radiationless dexcitation through internal rearrangement (Auger process) (Figure 21). The kinetic energy of the emitted photoelectron is calculated by:

$$K.E._{XPS} = E_{ph} - \phi_{XPS} - B.E._{XPS} \qquad (23)$$

where $K.E._{XPS}$ is the kinetic energy of the photoelectron, $E_{ph}$ (hλ) is the initiating photon energy, $\Phi_{XPS}$ is the work function of the instrument (calibrated), and $B.E._{XPS}$ is the binding energy of ejected electron. The $K.E._{XPS}$ is the measured value from the instrument and $E_{ph}$ is known from the incident x-ray.

Through obtaining the binding energies, quantitative elemental analysis can be completed through counts and peak integration. The binding energies for the elements of interest in their natural forms are: C1s 284.2 eV, N1s 409.9, N2s 37.3, O1s 543.1, and O2s 41.6. A range is found around these energies that correlate with the elemental environment. Through deconvolution of C1s peaks, determination of species is found at: 282.6-282.9 eV for carbidic carbon, 284.6-285.1 eV for graphitic carbon, 286.3-287.0 eV for carbon present in ether and alcohol groups, 287.5-288.1 eV for carbonyl groups, and 289.3-290.0 eV for carboxyl or ester functional groups.[159] Additionally, nitrogen functionalities (N1s) can be found with the following binding energies and peak width at half height: 399.7 eV (2.5) for imides, 398.7 eV (1.76) for pyridinic, 399.9 eV (2.5) for amides, and 400.7 eV (2.5) for pyrroles.[160] Where O1s functional groups can be found at: 530.4-530.8 eV for C=O, 534.8-535.6 eV for C-OH and/or C-O-C, and chemisorbed water is found between 534.8-535.6 eV.[159] From this representative data, a general scheme for the functionality present in the carbon samples can be analyzed for the effect on $CO_2$ capture and heat of adsorption.

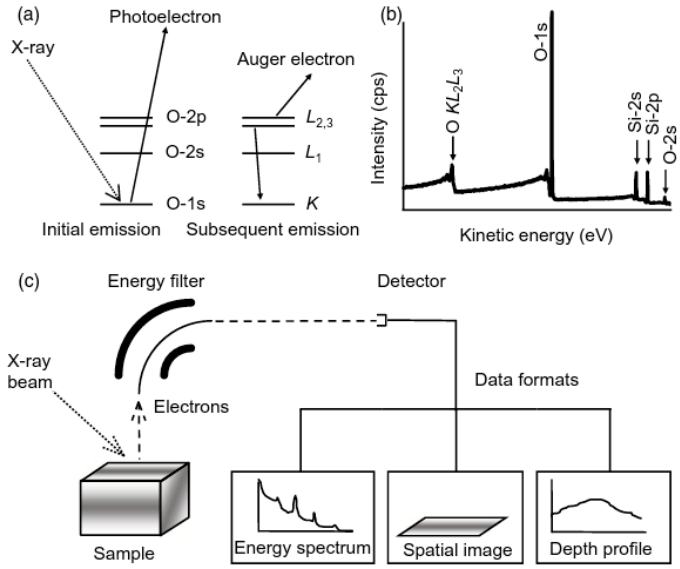


**Figure 21. Schematic example of the photoelectron process (a) and Auger electron emission process with corresponding XPS spectra (b). The typical instrumental process shown in (c). *Reproduced from* [161]**

## 3.5 X-ray diffraction

Typically, x-ray diffraction (XRD) and small angle x-ray scattering (SAXS) is used on very ordered porous and crystalline materials to determine the structure and morphology through interpretation of the counts with respect to the angle of diffraction or scattering. Due to the amorphous carbon structure, diffraction results in broad peaks. Similarly, SAXS also provides broad peaks but data can also be obtained through fitting techniques for the pore size. Results can be qualitatively analyzed and confirmed using SEM and TEM for morphology and $N_2$ adsorption for surface area and pore size.

# CHAPTER 4.
# MESOPOROUS CARBON MONOLITHS DERIVED FROM NOVOLAC PRECURSORS VIA SOFT TEMPLATE SYNTHESIS

Mesoporous carbon monoliths were prepared by soft templating via self-assembly of phloroglucinol and formaldehyde with the triblock copolymer Pluronic® F127 and subsequent calcination and activation. The effect of calcination temperature on the surface and the porosity were investigated. The results showed that $CO_2$ adsorption capacities by these monoliths were significantly affected by calcination temperature prior to activation resulting from the variation of surface area and the width of the mesopores. In *Chapter 7,* review of the characteristics of MCMs after activation and their use for $CO_2$ capture is evaluated.

## 4.1 Introduction

The use of carbon materials as sorbents for $CO_2$ adsorption has been of interest due to the low cost and high stability. Many have made some excellent work on the adsorption of $CO_2$ by carbon materials.[49, 162-164] For example, Maroto-Valer et al. showed that the use of anthracites activated with ammonia and impregnated with polyethylenimine raised the alkalinity

of the surface for adsorption of $CO_2$, however, encountered lower surface areas after impregnation due to pore blockage.[163] They also reported the progress in the use of carbon-rich doped with amines for $CO_2$ capture.[162] Furthermore, Zhang group reported that modifying the high surface area of activated carbon by microwave irradiation in $N_2$ atmosphere showed the encouraging results of 3.75 mmol $g^{-1}$ $CO_2$.[164] The coupling of porous carbon materials with high surface areas and organized pore structures with surface modification and activation has indicated the relevance of porous carbon for selective adsorption.

Monoliths, in general, are favorable structures as adsorbents because of their unique properties.[165] The synthesis of monoliths with a hierarchal pore structure has been explored using both hard and soft templating techniques with both silica and carbon frameworks; however, the use of strong acids for the removal of the metal complex is needed.[107] The hierarchal pore structure in this work is formed by soft templating, which utilizes self-assembly of the triblock copolymer Pluronic® F127 (poly(ethylene oxide)-*b*-poly(propylene oxide)-*b*-poly(ethylene oxide) $EO_{106}$-$PO_{70}$-$EO_{106}$) to form micelles in the acidic water/ethanol solution. A phenolic resin precursor, phloroglucinol and formaldehyde, is introduced under acidic conditions. The formaldehyde is protonated and an electrophilic aromatic substitution creates the phloroglucinol-formaldehyde (PF) novolac polymer. The phloroglucinol-formaldehyde polymer interacts *via* hydrogen bonding with the hydrophilic poly(ethylene oxide) (PEO) corona. The PF-Pluronic F127 undergoes phase separation as step-growth polymerization progresses with time and becomes immiscible. After solvent removal, the gel is combined with triethylene glycol (TEG) and cured at 96 $^{o}$C. During this time, phase separation *via* spinodal decomposition occurs giving rise to macro domains. The solid polymer is then removed from the TEG solvent, rinsed

and dried thoroughly, and calcined to reveal a hierarchical carbon structure, where macropores were formed by the spinodal decomposition of the PF-F127 TEG polymer blend, the micro/mesopores were revealed through the removal of the F127 via calcination, and the pore walls remain due to the stability of the PF resin. Recently, Lu et al. used this method for the synthesis of monoliths, which contain diaminohexane and reported an adsorption capacity of 3.30 mmol $g^{-1}$.[105] Compared with microporous structures, the hierarchical micro/mesoporous structures of the monoliths allow for easier mass transport and higher permeability, which exhibit many desirable characteristics needed to employ the material in a large-scale industrial setting.[166] Thereby, the unique properties of the mesoporous carbon monoliths (MCMs) inspired us to investigate its adsorption of $CO_2$.

In this chapter, review of the pore properties and surface chemistry of MCMs calcined at various temperatures prior to activation and the capture of $CO_2$ was investigated.

## 4.2 Synthesis and characterization of monolithic mesoporous carbon

*Chemicals.* Phloroglucinol (99%), triethylene glycol (TEG) (99%), hydrochloric acid, and formaldehyde (37 wt. % solution in $H_2O$, stabilized with 10-15% methanol) were purchased from Acros Organics chemical company through Thermo Fisher Scientific. Pluronic® F127 was obtained through Sigma Aldrich Co. Ethanol (200 proof) was purchased from Decon Labs through Thermo Fisher Scientific. All chemicals were used as received.

*Preparation of polymer precursor.* Phloroglucinol-formaldehyde (PF) and triblock copolymer, Pluronic F127, were used for the polymer monolith synthesis as in previous publications.[99, 167, 168] 2.52 g of phloroglucinol and 2.52 g of Pluronic® F127 were dissolved in 18.0 g of EtOH-$H_2O$-HCl stock solution (mass ratio: 100 EtOH: 90 $H_2O$: 2 HCl), then 2.6 g of formaldehyde (37 wt.%) was added. This solution was set to stir at room temperature for 70 min, with clouding occurring at about 10 to 15 min. The solution was then centrifuged and the ethanol/water layer decanted. The obtained gel was thoroughly mixed with 2 equivalents of TEG. After transferred to 4 mm I.D. Pyrex tubes, the tubes were sealed and placed into an air bath at 96 $^oC$ for three days. Then, the tubes were removed and the monoliths extracted and washed thoroughly with TEG, ethanol, and water, successively.

*Calcination.* The monoliths were placed into quartz tubes to dry overnight at 70 $^oC$, and calcined at their respective temperatures for 3.5 h with a ramp speed of 5 $^oC$ per minute. The samples were identified with their respective calcination temperature i.e. MCM-600 identifies the MCM calcined at 600 $^oC$.

## 4.3 Results and Discussion

### 4.3.1 Phase separation

Phase separation is an established synthesis technique for the synthesis of porous polymers. Phase separation occurs when a miscibility imbalance occurs. There are two

approaches to inducing phase separation: thermally induced phase separation (TIPS) and chemically induced phase separation (CIPS).

TIPS occurs due to a critical solution temperature, either the upper critical solution temperature (UCST) or lower critical solution temperature (LCST), where solubility decreases due to decreased polymer-solvent interactions resulting in a two-phase morphology. CIPS or polymerization induced phase separation (PIPS) occurs through mixing of polymer precursors and a low molecular weight, non-reactive solvent.

An example of the phase regions found with polymer-solvent and polymer-polymer blends can be found in Figure 22. The mixing of two components can be expressed through the Gibbs free energy equation (of mixing):

$$\Delta G_m = \Delta H_m - T\Delta S_m \tag{24}$$

$$\left(\frac{\partial^2 \Delta G}{\partial \phi_i^2}\right)_{T,P} > 0 \tag{25}$$

When $\Delta G_m$ is < 0, miscibility will occur but with certain areas of the phase diagram where the mixture leans heavily toward one component. By taking a second derivative of $\Delta G_m$ with respect to the volume fraction, $\phi_i$, in Equation 25, negative values represent phase rich regions present on the phase diagram.[169] The spinodal can be found where Equation 25 is equal to zero. Furthermore, a third partial derivative reveals the critical point, which is where the binodal and spinodal connect.

For low molecular weight components, increasing miscibility occurs with increasing temperature due to the $T\Delta S_m$ being large, where decreased miscibility can occur when referring

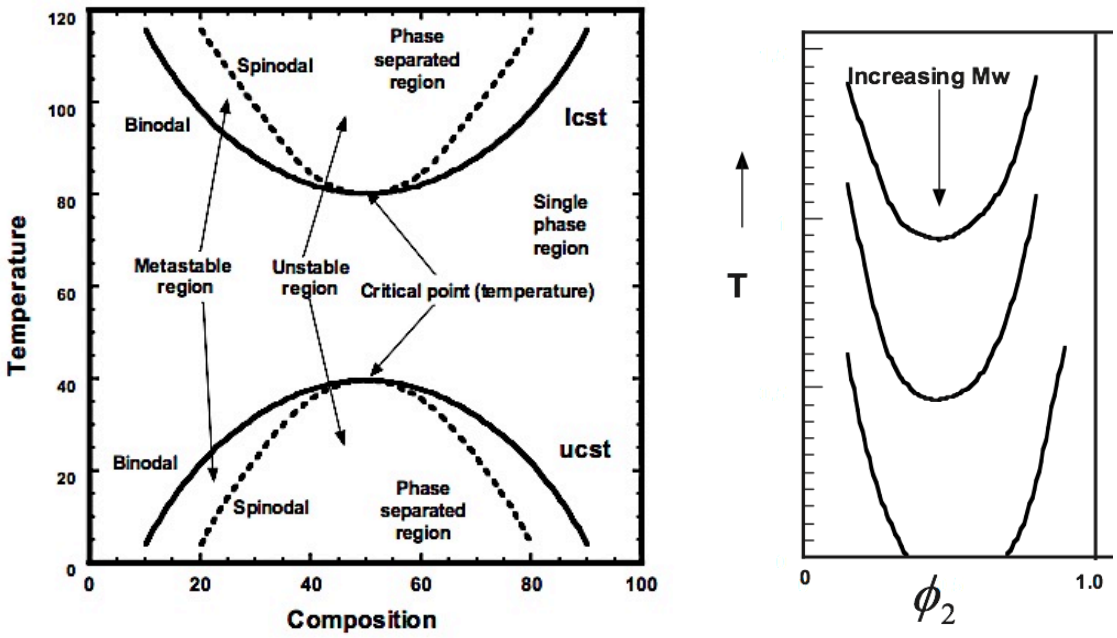


**Figure 22. Phase diagram indicating the behavior polymers in solution or as polymer blends (left) and the influence of increasing molecular weight on the LCST (right).** ***Reproduced from*** **[170]**

to higher molecular weight polymers due to conformational restrictions (Figure 22). Volume fractions ($\phi_i$):

$$\phi_1 = \frac{V_1 N_1}{V_1 N_1 + V_2 N_2} \quad (26)$$

$$\phi_2 = \frac{V_2 N_2}{V_1 N_1 + V_2 N_2} \quad (27)$$

When substituted into Equation 36, it is evident that by increasing molecular weight (correlates to $N_1$ and $N_2$, which represent cells in a lattice with volumes $V_1$ and $V_2$, respectively), it becomes more difficult to influence this factor in the Gibbs free energy equation. It is apparent that the reaction conditions that increase polymerization rate (temperature and reactivity of monomers) and molecular weight directly effect the phase separation, thus directly affecting the morphology of resulting polymer and subsequent carbon inverse structure.

### 4.3.2 Dual phase separation

Crossing the boundary between miscibility and phase separation can occur through nucleation and growth or spinodal decomposition by TIPS or CIPS. Nucleation and growth occurs in the metastable region and forms large spherical domains that increase in size and concentration with increasing time, whereas spinodal decomposition occurs from a minor change of temperature through the critical point and forms interconnected regions of polymer that uniformly grow with increasing time.[169] Parallel with the above phase separation phenomena, when block copolymers are considered, an array of morphologies can be obtained through self-assembly. The distinct of properties of each block in a particular solvent determines the corona

(soluble block) and the core (insoluble block) when microphase separation occurs. The phase behavior of neutral triblock copolymer Pluronic® F127 ($PEO_{70}PPO_{100}PEO_{70}$) behaves similarly to that of diblock copolymers due to the symmetry of the hydrophilic PEO blocks around the central hydrophobic PPO block.[171] The representative phase diagram for diblock copolymers, Figure 23, represents the morphologies that can be obtained through variation of *f*, the volume fraction, which is a function of χN, the total enthalpy attaching the two chains together.[172]

Although, the reference to the block copolymer in Θ-solvent remains of importance, the influence of additives to the system is of interest to used the block copolymer as a templating agent. When a phenolic moiety, i.e. phloroglucinol, is introduced to the self-assembled block copolymer, hydrogen bonding occurs and dissolution of the phenolic in the corona swells the domain size. Additionally, acidic conditions further enhance the hydrogen bonding effect and, under these conditions, the addition of formaldehyde crosslinks the phloroglucinol *via* step-growth polymerization.[99]

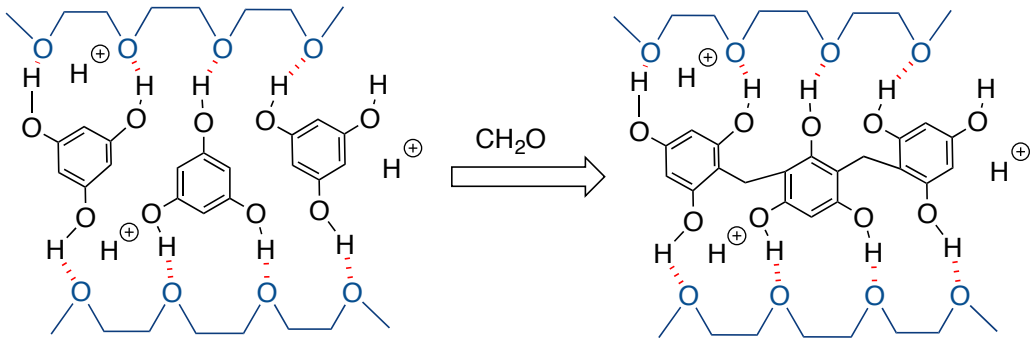


**Scheme 1. Hydrogen bonding of phloroglucinol with ethylene oxide block under acidic EtOH/$H_2O$ (left) and localized polymerization of phloroglucinol with formaldehyde to form a linear polymer with methylene linkages.**

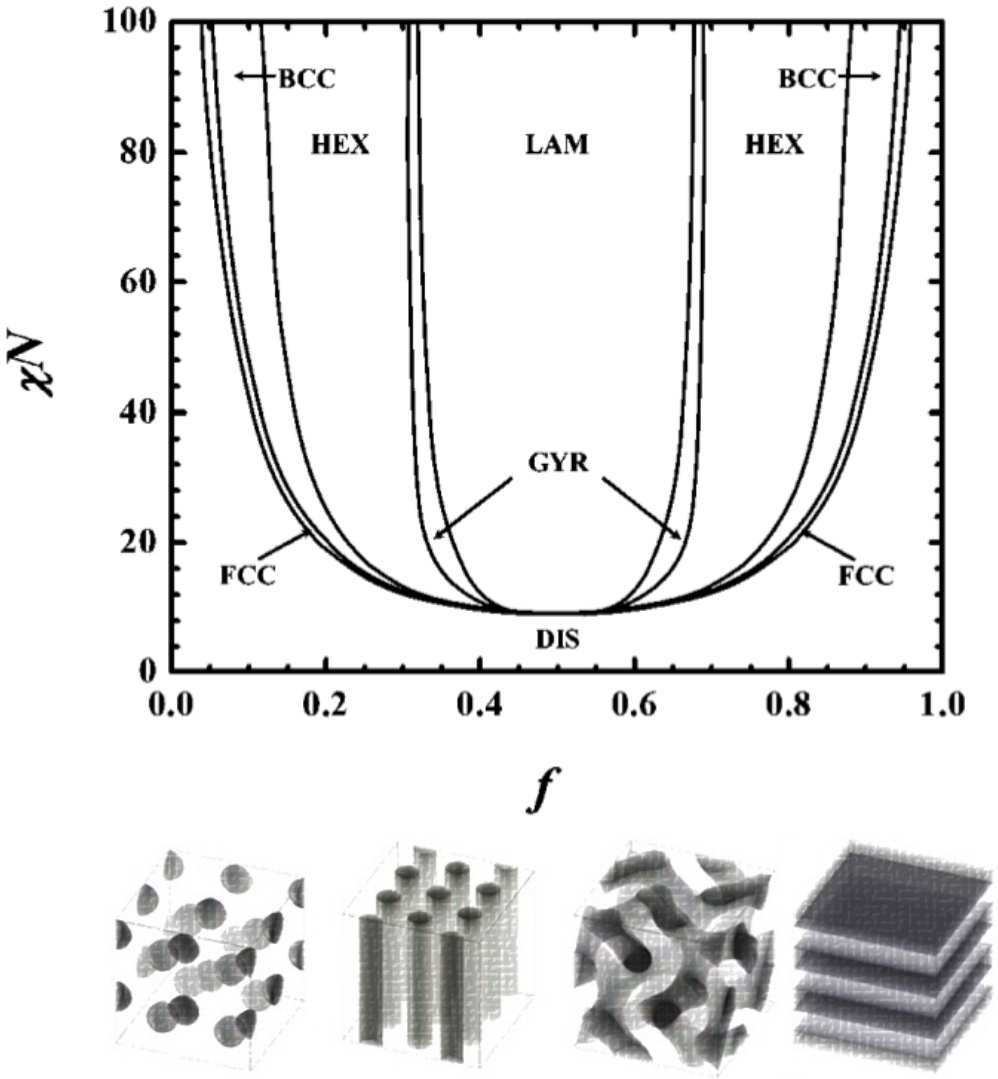


**Figure 23. Generalized phase diagram for diblock copolymers exhibiting lamellar (LAM), hexagonal (HEX), gyroid (GYR), face-centered cubic (FCC), body-centered cubic (BCC), and disordered morphologies in the regions indicated.** ***Reproduced from [172]***

As polymerization progresses, the molecular weight of the phloroglucinol-formaldehyde (PF) resin increases and the now polymer blend reaches a point of decreased miscibility indicated by the cloud point. Further polymerization shows a clear phase separation of the polymer blend from the aqueous ethanol solution. The experimental conditions promoted the formation of bicontinuous (gyroid) microstructure found previously.[167] This stage is a representation of CIPS/PIPS for the formation of a polymer blend, termed the polymer precursor, for monolith formation.

The synthesis of mesoporous monolithic carbon considers that both CIPS and TIPS are actively participating in a "dual phase separation" in the formation of the polymer rod prior to calcination (Figure 24).[167] The polymer blend is combined with a low molecular weight glycolic solvent and placed in glass tubes, sealed and heated. During this process, another cloud point is observed where a lower critical solution temperature (LCST) is reached and spinodal decomposition occurs. The resulting macroscopic phase separation forms the monolithic polymer. The increased temperature also serves to further cure and anneal the PF resin, essentially "locking in" the CIPS established previously.

### 4.3.3 Pore and surface characteristics

With increasing calcination temperature of the polymer monolith, more heteroatoms are eliminated from PF resin in addition to the elimination of the triblock copolymer template. The result is a contraction of the remaining carbon sheets, which can be observed through the porosity. The pore characteristics from the monolithic carbon yielded the characteristic type IV

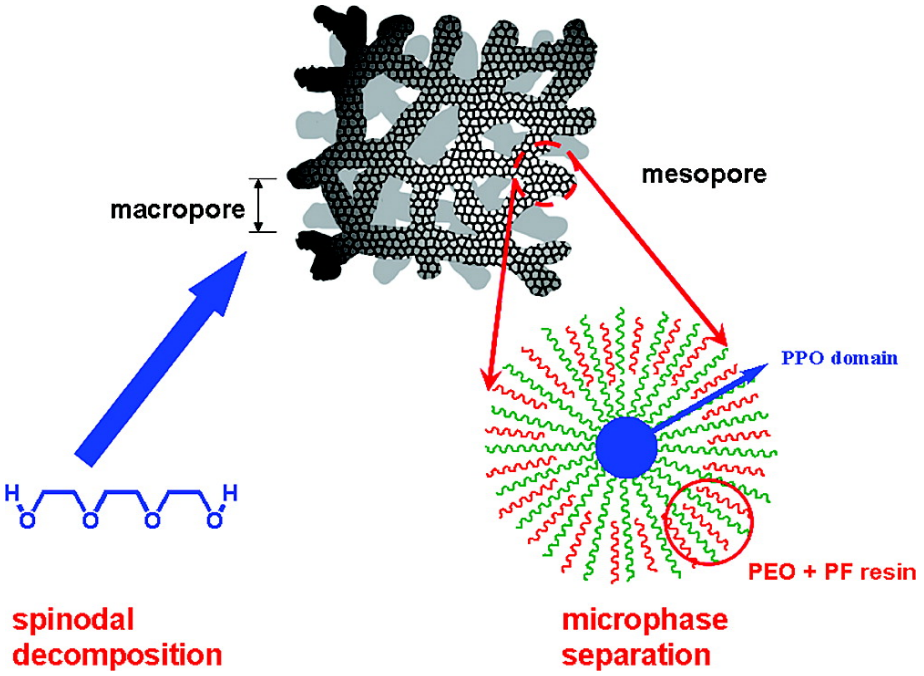


**Figure 24. Bimodal mesoporous carbon using dual phase separation synthesis.** ***Reproduced from*** **[167]**

isotherm, confirming the presence of mesopores with a steep transition adsorption and plateau at 0.95 relative pressure, as shown in Figure 25 are summarized in Table 3. The diminishing plateau indicates the widening of the mesopores into macropores.

An increase in surface area is observed up to a calcination temperature of 600 $^{o}$C and steadily decreases to 700 $^{o}$C and 800 $^{o}$C. The decrease in surface area directly correlates to the decreasing oxygen content found *via* XPS in Table 4. It should also be noted that an increase in $CO_2$ adsorption capacity is found with the monolith calcined at 700 $^{o}$C could be accounted for by the decrease in O2 (~533 eV) in the XPS spectra that recognizes the presence of carboxylic acid, whose acidic properties would offset the adsorption of acidic $CO_2$ molecules.[173] The decreased occurrence of this type of oxygen functionality can be directly associated with calcination temperature, as seen previously in Figure 4, and like many other oxygen functionalities is eliminated at increased temperatures. Although the decrease in oxygen provides increased adsorption of $CO_2$, the oxygen containing functionality can act as a tether for activating agents and direct them to the surface due to an imbalance in electrostatic potential, where the amount of oxygen present prior to activation can be tuned, as shown in Table 4, by the calcination temperature instead of pre-activation oxidation.[174, 175]

## 4.4 Conclusion

By using this prescribed method, a monolithic column was successfully synthesized and calcined to examine the pore characteristics and surface functional groups. Pristine mesoporous

**Table 3. Textural characteristics of monolithic mesoporous carbon.**

| Adsorbent [a] [°C] | $S_{BET}$ [$m^2$ $g^{-1}$] | $S_{micro}$ [$m^2$ $g^{-1}$] | $V_{micro}$ [$cm^3$ $g^{-1}$] | $CO_2$ uptake capacity [b] [mmol $g^{-1}$] |
|---|---|---|---|---|
| 400 | 384 | 59 | 0.023 | 0.685 |
| 500 | 462 | 154 | 0.0110 | 0.679 |
| 600 | 513 | 223 | 0.101 | 1.365 |
| 700 | 478 | 226 | 0.102 | 1.584 |
| 800 | 393 | 138 | 0.0613 | 1.358 |

[a)] Sample identified by calcination temperature; [b)] ~25 °C and 1 bar.

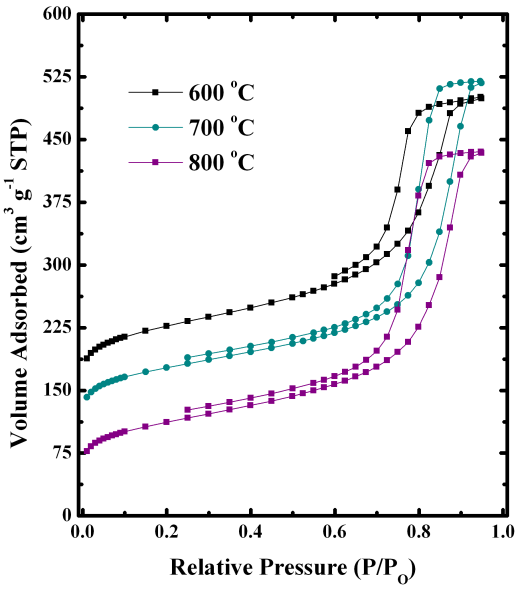


**Figure 25. Nitrogen adsorption and desorption isotherms at -196 °C of carbon monoliths. The isotherms for 600 °C and 700 °C are vertically offset by 80 $cm^3$ $g^{-1}$ and 40 $cm^3$ $g^{-1}$, respectively.**

**Table 4. XPS results for monolithic carbon prepared from calcination phloroglucinol-formaldehyde polymer.**

| Adsorbent [$^{o}$C] | | C1 | C2 | C3 | C4 | O1 | O2 | Total %C | Total %O |
|---|---|---|---|---|---|---|---|---|---|
| **400** | *counts* | *284.70* | *286.20* | *288.71* | *291.17* | *531.36* | *533.49* | | |
| | % | 66.0 | 29.2 | 2.7 | 2.1 | 19.5 | 80.5 | **85.1** | **14.9** |
| **500** | *counts* | *284.77* | *286.25* | *288.80* | *291.12* | *531.73* | *533.73* | | |
| | % | 70.1 | 23.6 | 4.3 | 2.0 | 27.3 | 72.7 | **88.3** | **11.7** |
| **600** | *counts* | *284.74* | *286.33* | *288.69* | *290.84* | *531.81* | *533.73* | | |
| | % | 76.1 | 16.1 | 5.5 | 2.3 | 28.9 | 71.1 | **93.4** | **6.6** |
| **700** | *counts* | *284.79* | *286.34* | *286.63* | *290.89* | *531.81* | *533.67* | | |
| | % | 74.9 | 13.9 | 7.6 | 3.6 | 34.3 | 65.7 | **96.9** | **3.1** |
| **800** | *counts* | *284.79* | *286.29* | *299.61* | *290.91* | *531.81* | *533.27* | | |
| | % | 73.0 | 15.4 | 7.7 | 3.9 | 26.0 | 74.0 | **97.2** | **2.8** |

carbon that was calcined at 600 $^{o}$C reached a peak specific surface area (513 $m^2$ $g^{-1}$) and pore volume (0.101 $cm^3$ $g^{-1}$), which is used for activation and $CO_2$ adsorption in *Chapter 7*. Although $CO_2$ adsorption measurements of monoliths calcined at 700 $^{o}$C prior to activation exhibit a higher $CO_2$ adsorption capacity than those calcined at 600 $^{o}$C, the monoliths calcined at 600 $^{o}$C were used for chemical activation, *via* KOH, due to the high oxygen content for increased reactivity. Monolithic carbon materials, especially those with a hierarchically pore structure, provide the necessary framework for increased adsorption capacity upon activation, water stability, and low reactivity in addition to the monolithic features of the material, which allows for ease of handling, decreased loss material under high flux, and a low pressure differential during adsorption. All of these factors decrease the implementation and operating costs to utilize the material in a power generation facility while still retaining the adsorption capabilities of porous carbon.

# CHAPTER 5.
# A NON-MICELLAR SYNTHESIS OF MESOPOROUS CARBON VIA SPINODAL DECOMPOSITION

This chapter is revised based on a paper published as:

K.M. Nelson, Z. Qiao, S.M. Mahurin, R.T. Mayes, C.A. Bridges, and S. Dai. A Non-Micellar Synthesis of Mesoporous Carbon via Spinodal Decomposition. RSC Advances (2014) Volume 4. pp. 23703-23706.

I provided the major contributions to this paper, excluding various SEM and TEM imaging, SAXS analysis, and the scheme associated.

## 5.1 Introduction

Traditional porous carbon materials are derived from coal, wood, biomass, or polymers.[10, 59, 176] These carbons are typically microporous, which are formed from defects left by heteroatoms that are eliminated during calcination. Microporous carbons are often inadequate in reference to conductivity, mass transport, and structural integrity due to remaining

heteroatoms, restricted flow pathways, and lack of structural control. These deficiencies can be resolved by the introduction of mesoporosity, which make them ideal for catalysis, batteries, super capacitors, and adsorbents.[177, 178] Mesoporous carbons that can be tailored to optimize these applications are in high demand.

The standard templating synthesis uses methods that can be both costly and hazardous on the industrial scale.[177, 179] For instance, hard-templating of mesoporous carbons involves using a sacrificial silica template in combination with a carbon precursor, in which the template is etched after calcination with harsh acids or bases (i.e. HF, NaOH) and a carbon inverse replica is revealed.[87, 88, 180] Soft-templating synthesis tends to be less severe and is based on a self-assembly approach using block copolymer templating agents, which are removed via calcination.[99, 100, 181, 182] The block copolymer can be synthetically intensive to produce, making them very costly. While both of these methods produce well-defined mesopore size distributions and morphologies, they lack a facile route for mesopore development and a cost effective porogen that is relinquished by the process for industrial scale viability. Recently Seo and Hillmyer demonstrated polymerization induced microphase separation of trithiocarbonate terminated polylactide with vinylbenzene/divinylbenzene for mesoporous polymer synthesis via radical addition-fragmentation chain transfer.[179] Polymerization quenched spinodal decomposition creates mesoscopic domains and, when combined with calcination, the pore forming polymer is effectively removed while the carbon precursor remains, preserving the mesostructure. The concept of phase separation was addressed previously in *Chapter 4* for dual phase separation, where the first phase separation occurred due to polymerization induced phase separation and the second occurred during temperature induced phase separation. The acid

ethanol reflux conditions used to induced spinodal decomposition of linear poly (ethylene glycol) were similar to those used for the synthesis of mesoporous carbon using the same PF polymer with an amphiphilic triblock copolymer.[56]

## 5.2 Experimental methods for synthesis and characterization

*Chemicals.* Commercially available polyethylene glycol (PEG) with different average molecular weight: 1 kDa, 2 kDa, 4 kDa, and 8 kDa received from Fluka, along with 20 kDa and 14 kDa PEG and poly ethylene oxide of 100 kDa and 200 k Da received from Sigma-Aldrich, were all used as received. The carbon precursor was phloroglucinol (>99.0%, Aldrich) and formaldehyde (37 wt.%, Sigma-Aldrich). Ethanol, 190 proof, (Decon labs) and aqueous HCl (37 wt.%, Sigma-Aldrich) were used without further purification.

*Preparation of polymer precursors.* 2.3 g of phloroglucinol, 5.3 g of 1 kDa PEG was dissolved under intense stirring in 130 mL ethanol and 1 g HCl (37 wt.%) while heating to reflux. At reflux, 2.3 g of aqueous formaldehyde was added. The cloud point occurred within 3 min after addition of formaldehyde. The reaction mixture was stirred for a total of 1.5 h, which resulted in solid masses.

*Calcination.* The ivory colored polymer solids were washed with ethanol and dried in an oven at 80 $^{o}$C overnight. Calcination was carried out in a tube furnace under flowing Ar at a heating rate of 2 $^{o}$C/min to 850 $^{o}$C and held for 2 h before cooling to ambient temperature.

*Nitrogen adsorption.* Mesoporous sample measurements carried out at 77K using a Micromeritics Tristar 3000 analyzer and microporous sample measurements on Quantachrome AS-1. Prior to measurement, samples were degassed at 170 $^{o}$C under $N_2$ for at least 6 h. The specific surface area was calculated using the Brunauer-Emmett-Teller (BET) method. The pore volume was estimated from singe point adsorption at a relative pressure of 0.995. The average pore diameter was determined from the adsorption branch, according to the Barrett-Joyner-Halanda (BJH) method using Kruk-Jaroniec-Sayari (KJS) correction.

*Electron microscopy.* Scanning electron microscopy (SEM) and transmission electron microscopy (TEM) images were obtained using a Hitachi HD 2000 STEM microscope at 200 kV. Samples for STEM were prepared by dispersion casting, where the sample was dispersed in ethanol with the grid and allowed to dry at ambient temperature before analysis.

*Small angle x-ray scattering (SAXS).* SAXS data were collected with a Panalytical Empyrean diffractometer with Cu Kα radiation.

## 5.3 Results and Discussion

Here, we established a surfactant-free preparation of mesoporous carbon through the in-situ polymerization of phloroglucinol-formaldehyde (PF) resins in the presence of polyethylene glycol (PEG) in acidic ethanol under reflux (Figure 26). The acid catalyzed condensation polymerization of PF resins has served as a carbon precursor previously[167, 183, 184] but the

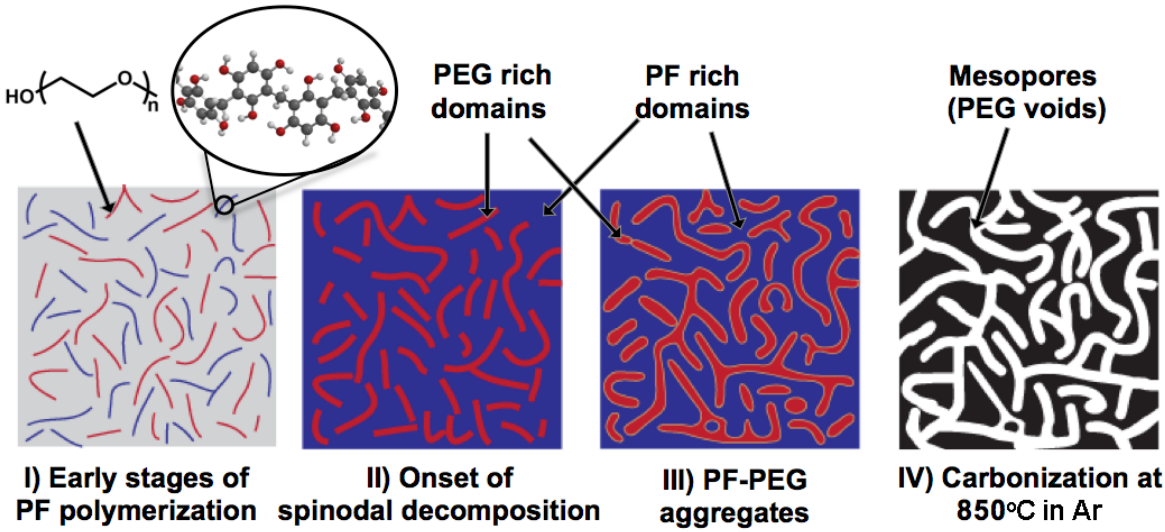


**Figure 26. Schematic illustration of spinodal decomposition (I to III) and subsequent formation of mesoporous carbon (IV) from PF-PEG adduct.**

essence of our methodology resides in the synthesis of mesoporous carbon through spinodal decomposition instead of traditional micellar self-assembly approaches.[167] In lieu of triblock copolymers as templating agents, utilization of linear PEG provides a more cost effective alternative as a sacrificially templating agent.

In a typical run, phloroglucinol, formaldehyde, and PEG were mixed in ethanol under acidic conditions. Under refluxing conditions, PF-PEG aggregates were formed and precipitated. The PF-PEG solid was then dried and calcined at 850 $^{o}$C for 2 h under Ar atmosphere at a rate of 2 $^{o}$C/min. Under these conditions, the near complete degradation of all MWs of PEG used can be achieved and calcination of remaining PF at this temperature could yield a material optimal for conductivity testing.[185, 186] The mesoporosity of the resulting carbon material was confirmed via scanning electron microscopy (SEM) and transmission electron microscopy (TEM) (Figure 27 and Figure 28). The surface area of these materials was measured using nitrogen adsorption (Figure 29).

On the basis of our results and literature reports, a possible mechanism for the formation of mesoporosity under the specified conditions is summarized in Figure 26. Upon addition of formaldehyde, acid catalyzed PF condensation polymerization occurs. As step- growth polymerization proceeds, the hydrophilic PF macromolecules undergo hydrogen-bonding interactions with the PEG polymers, leading to the formation of homogeneous PF-PEG aggregates, i.e. “polymer blend”. As PF molecular weight increases, microphase separation of the aforementioned homogeneous aggregates into the mesoscopic domains via spinodal decomposition is evidenced by the co-continuous structure found in Figure 1 and only microporosity in the PF sample without PEG addition (Figure 30).[16] The PF polymerization

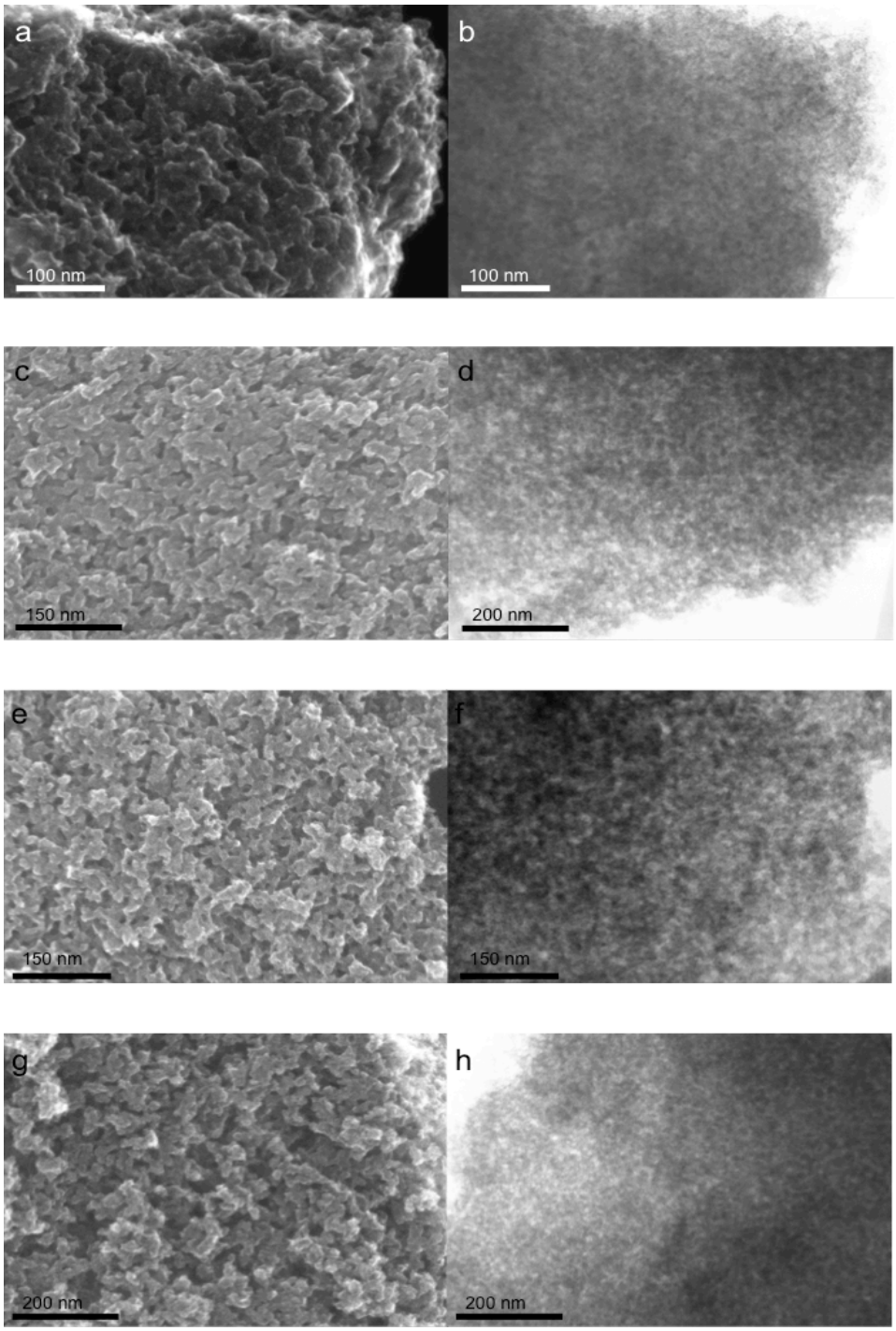


**Figure 27. The SEM image (left) and TEM image (right) of mesoporous carbon derived from PF-PEG 2 k MW (a and b), 4 k MW (c and d), 8 k MW (e and f) and 14 k MW (g and h) after calcination at 850 $^{o}$C for 2h.**

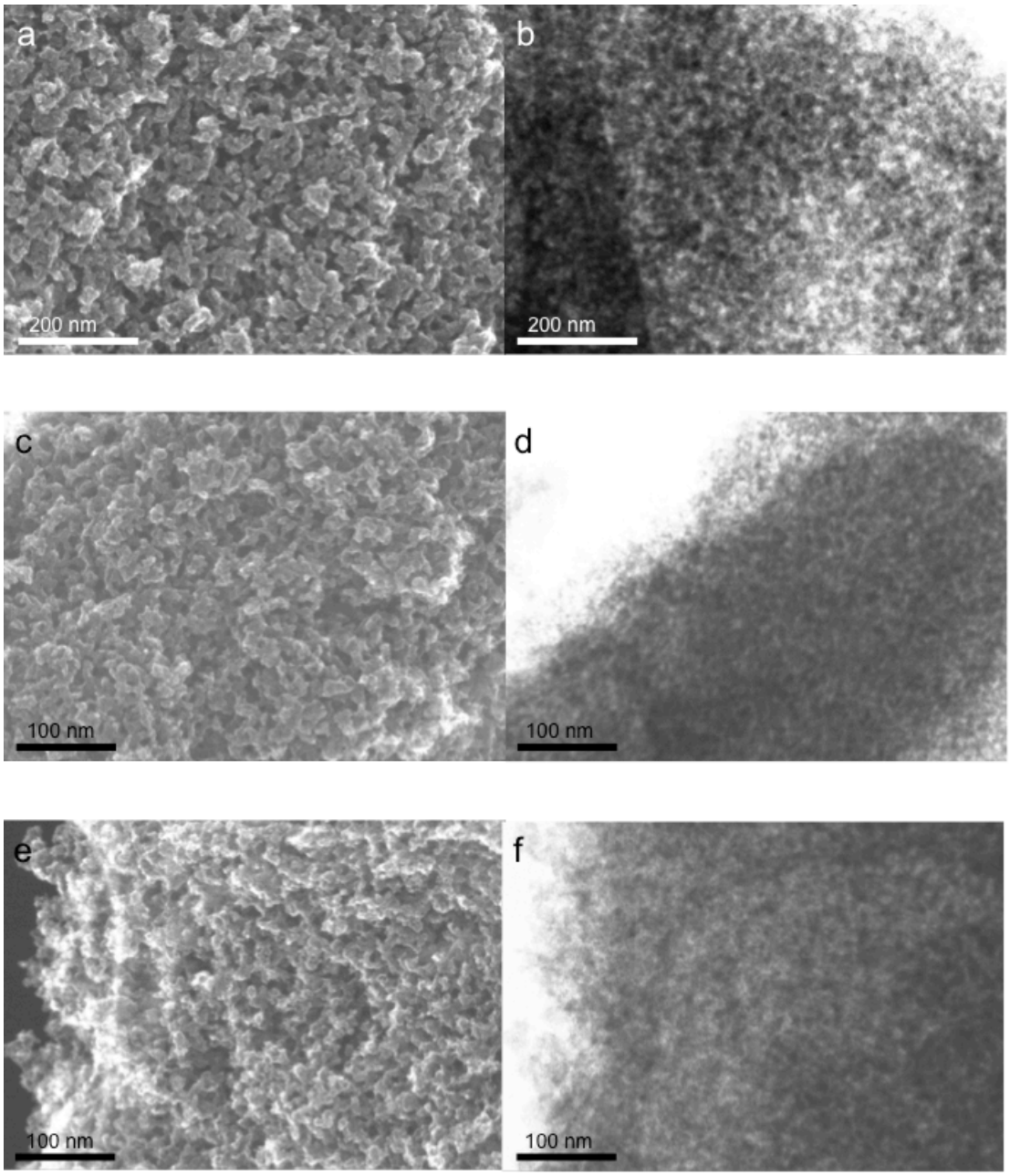


**Figure 28. The SEM image (left) and TEM image (right) of mesoporous carbon derived from PF-PEG 20 k MW (a and b), 100 k MW (c and d), and 200 k MW (e and f) after calcination at 850 oC for 2h.**

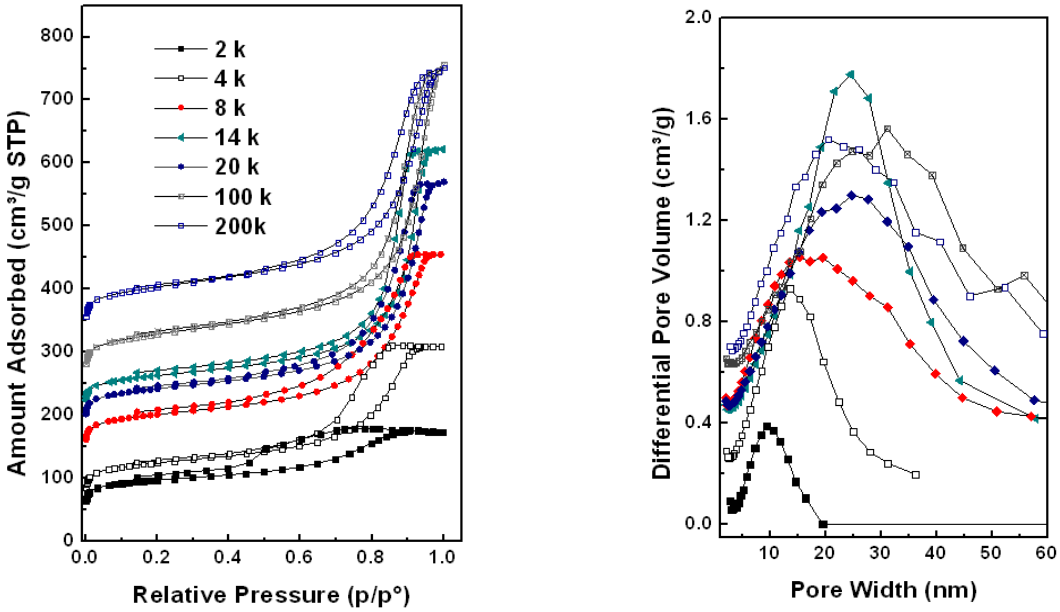


**Figure 29. Nitrogen -196 °C adsorption isotherms (left) and corresponding pore size distributions (right) calculated using KJS method of carbon samples with respective PEG (in Da). For clarity, the isotherms were offset by consecutive increments of 50 $cm^3/g$ and pore size distributions offset in consecutive increments of 0.2 $cm^3/g$.**

**Table 5. Adsorption parameters of mesoporous carbons varying $M_w$ of PEG template as calculated from $N_2$ adsorption at -196 °C isotherms.**

| PEG $M_w$ [Da] | $S_{BET}$ [$m^2\ g^{-1}$][a)] | $S_{micro}$ [$m^2\ g^{-1}$][b)] | $S_{meso-ext.}$ [$m^2\ g^{-1}$] | $V_{total}$ [$cm^3\ g^{-1}$] | $V_{micro}$ [$cm^3\ g^{-1}$][c)] | $V_{meso}$ [$cm^3\ g^{-1}$] | $D_{meso}$ [nm] |
|---|---|---|---|---|---|---|---|
| 2 k | 360 | 246 | 114 | 0.197 | 0.099 | 0.098 | 9 |
| 4 k | 368 | 219 | 149 | 0.356 | 0.089 | 0.267 | 14 |
| 8 k | 372 | 210 | 162 | 0.480 | 0.085 | 0.395 | 16 |
| 14 k | 321 | 162 | 159 | 0.637 | 0.066 | 0.571 | 25 |
| 20 k | 368 | 219 | 149 | 0.374 | 0.089 | 0.285 | 25 |
| 100 k | 375 | 165 | 210 | 0.746 | 0.069 | 0.677 | 31 |
| 200 k | 375 | 171 | 204 | 0.629 | 0.071 | 0.558 | 21 |

a) Specific surface area calculated using the BET equation in the relative pressure range of 0.05-0.20. b) The number in parentheses are percentages of mesopore volume out of total pore volume. c) Average pore diameter found at maximum differential pore volume.

"chemically quenches" the reaction in the spinodal region and as the phase composition changes and new phase miscibility conditions are established for the newly formed polymer-polymer blend.

The acid is an essential component not only to the catalyzed polymerization of PF polymers but also to the interaction between the PF-PEG for driving the spinodal decomposition. The latter was evidenced by the formation of only microporous carbons from the samples prepared without acid. The cloud point is a function of solubility of the polymer blend in ethanol. During polymerization induced phase separation when the molecular weight of the starting PEG is decreased, delayed cloud point is observed due to the increased solubility of this component of the blend in the refluxing ethanol. Acidic ethanol at increased temperature reduces polymer-polymer interactions, causing the end-to-end distance of the polymer chains to shrink. Eventually cluster formation becomes favorable as polymer chains collapse, leading to efficient spinodal decomposition.[187-190] The as- synthesized material is non-porous (Figure 30) after drying and curing. The subsequent calcination at 850 $^{o}$C under inert Ar atmosphere destabilizes and decomposes the high oxygen containing PEG revealing an inverse carbon replica. The mesoporosity is evident from the condensation step in the nitrogen adsorption isotherm with desorption hysteresis characteristics of the type IV isotherm in Figure 29. Textural analysis was done using the Barrett, Joyner, and Halenda (BJH) method to calculate the pore size distributions procedure but with the triblock copolymer template, Pluronic F127 (MW 12.6 kDa, $PEO_{106}PPO_{70}PEO_{106}$), produced a similar micro- mesopore ratio and pore volume but with an average pore size of 8.9 nm and a BET surface area of 518 $m^2/g$.[191] Although the pore size distribution for PF-PEG (14 kDa) covers a much wider range of mesoporosity than that of

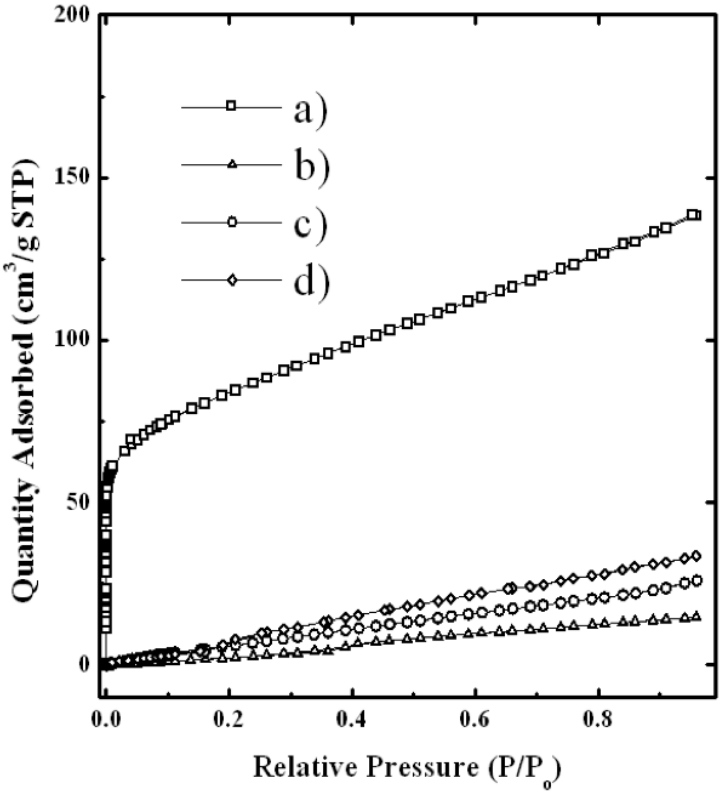


**Figure 30. The $N_2$ adsorption isotherms corresponding to (a) carbon produced using the typical synthesis without the addition of HCl (b) as synthesized polymer (c) carbon produced using the typical synthesis without the addition of PEG (d) carbon produced using PF-PEG 1k polymer.**

Pluronic F127 templated PF resin, the adsorbed $N_2$ contribution from micropores is only 0.066 $cm^3/g$ compared to 0.12 $cm^3/g$, attributing nearly 90 % of the pore volume to mesopores in contrast to 81 %, respectively.

Under acidic ethanol reflux conditions, linear PEG chains agglomerate via spinodal decomposition in a similar fashion to the self-assembly of hydrophobic and hydrophilic blocks of Pluronic F127. In the Pluronic F127 templated carbon, variation in mesopore size, pore size distribution discrepancies, and increased microporosity is due to self-assembly of micelles during the reflux and curing process. The hydrogen bonding between the PF resin and PEO corona yields the high microporosity in the resulting carbon; in contrast, PF resin has a much stronger interaction with the exterior of the PEG, owing to the separate polymer phases.

As seen in Table 5, mesoporosity extends to carbon produced using this method along a molecular weight range of 2 to 200 kDa PEG. Below 2 kDa PEG, no mesoporosity was observed and microporosity was nominal. At the low molecular weights (1 kDa PEG), the PEG still shows solubility in the refluxing ethanol but the addition of acid and the strong hydrogen bonding between the PF and PEG shows more of a "cast and mold" type situation where PF resin ("mold") congregates around the elongated PEG ("cast") to yield only micropores when calcined (Figure 30). At 2 kDa PEG, the desorption hysteresis closes at ~0.45 $P/P_o$, which is typically due to cavitation in spherical pores. The small-angle X-ray scattering (SAXS) patterns of as-synthesized samples in Figure 31 consist of one broad diffraction peak with $q$ values of 0.092 - 0.17, and no resolved features are observed for higher reflections. This result suggests a worm-like mesopore dominated structure, which agrees well with the results observed from TEM images. When reviewing the pore size distribution from the carbon sample using the upper most

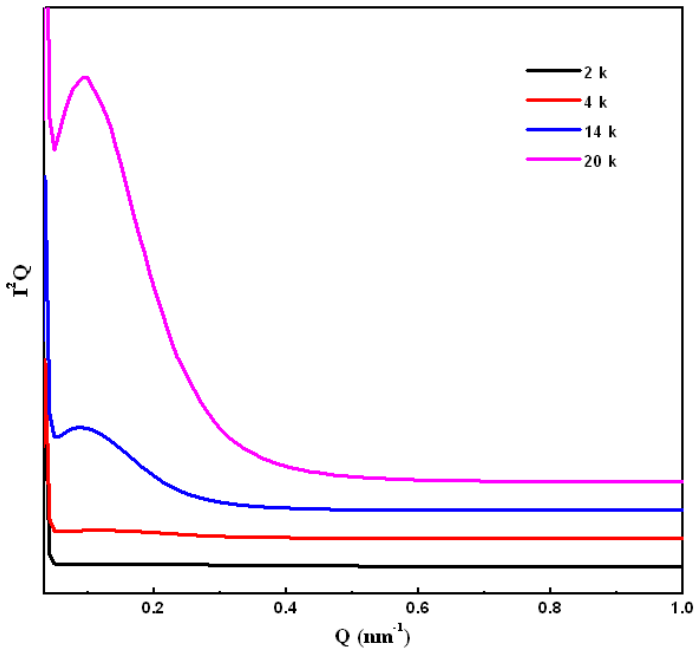


**Figure 31. Small-angle scatterings of mesoporous carbons using respective MW PEG.**

MW PEG, it is apparent that the broad pore size distribution is not a desirable characteristic for templated materials; although, this still provides a reasonably large effective range. The observed results in Figure 29 confirmed that by shifting the molecular weight from low to high, the average pore size increases. These values, however, cannot be reflected in the BJH average pore size calculation, as this method is used for mesopores in the range of 2 to 50 nm. With the pore size distributions for the larger molecular weight PEG, the calculation is not valid as it reaches this limit, considering the values fall well into macropore domain.

The mesopore volume can then be adjusted through the concentration of PEG in solution. This approach allows the mesopore volume of the resulting carbon to be either raised or lowered, as shown in Figure 32, for a specific application. Reducing the concentration from 2.9 mM to 1.4 mM PEG results in a minimal shift in pore size indicating, in this case, that the concentration determines the amount of the corresponding polymer phase. In contrast, when the amount of PEG is further reduced to 0.63 mM, the microporosity of the sample is doubled and mesoporosity is reduced by nearly 40 % (Table 6). By the reversal in porosity, decreasing the concentration of PEG shifts the composition ratio towards the binodal near a metastable region.[192] Consequently, there is less defined spinodal decomposition occurring and fractal clusters are formed that generate the mesopores and micropores, respectively.[193]

## 5.4 Conclusion

In summary, using non-surfactant linear PEG as a template for mesoporous carbon is reported. In contrast to prior soft templating approaches to mesoporous carbon, tailoring is

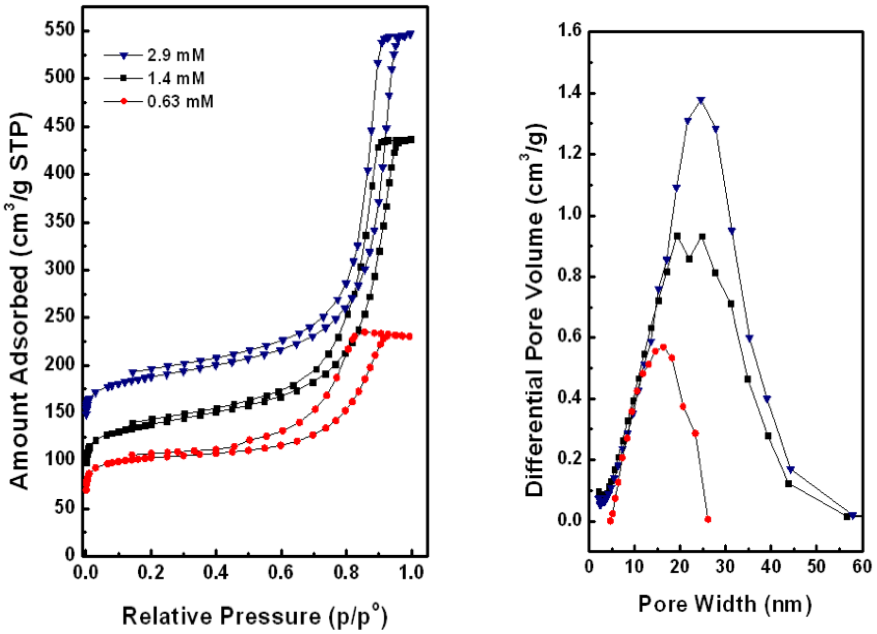


**Figure 32. Nitrogen -196 °C adsorption isotherms (left) and corresponding pore size distributions (right) calculated using BJH method of carbon samples with respective PEG (MW = 14 k Da) concentration. For clarity, the isotherms were offset consecutively by increments of 50 $cm^3/g$.**

**Table 6. Adsorption characteristics for mesoporous carbons of varying PEG concentration as calculated from nitrogen adsorption isotherms at -196 °C.**

| PEG Conc. [mM] [a] | $S_{BET}$ [$m^2\ g^{-1}$][b] | $S_{micro}$ [$m^2\ g^{-1}$] | $S_{meso-ext.}$ [$m^2\ g^{-1}$][c] | $V_{total}$ [$cm^3\ g^{-1}$][d] | $V_{micro}$ [$cm^3\ g^{-1}$] | $V_{meso}$ [$cm^3\ g^{-1}$][e] | $D_{meso}$ [nm][f] |
|---|---|---|---|---|---|---|---|
| 0.63 | 392 | 309 | 83 | 0.244 | 0.123 | 0.121 | 19 |
| 1.4 | 321 | 157 | 164 | 0.546 | 0.065 | 0.481 | 25 |
| 2.9 | 321 | 162 | 159 | 0.637 | 0.066 | 0.571 | 16 |

[a)] Phloroglucinol to 14 kDa PEG weight ratio; [b)] Specific surface area calculated using the BET equation in relative pressure range of 0.05-0.20; [c,d)] Mesopore and external surface area; [e)] Numbers in parentheses are percentages of mesopore volume; [f)] Pore diameter found at maximum differential pore volume.

limited only to the MW selection available. This material shows improvement by reducing inherent microporosity while increasing pore size. By tuning the PF to PEG ratio, the mesopore volume can also be adjusted. These characteristics may be useful where mesoporosity is necessary for mass transport. Increased adsorption sites can be added using various means of activation to increase microporosity and add functionality.[164, 191] The ability to finely tune the mesoporosity of a carbon material through molecular weight and concentration of PEG is relevant due to the novelty, particularly in comparison to traditionally triblock copolymer templates where tuning would require complex and complex polymer synthesis.

# CHAPTER 6. MESOPOROUS CARBON DERIVED FROM CHESTNUT TANNIN VIA SOFT TEMPLATE SYNTHESIS

## 6.1 Introduction

Porous carbon materials have been studied as $CO_2$ adsorbents because of their high chemical stability, high surface area, and low cost.[14, 51, 176, 194] Though a variety of methods have been explored to synthesize carbon, one popular approach is calcination of natural substances (i.e. corn cobs, sawdust, fruit shells, coal tar pitch, etc.) and activation to increase the surface area for adsorption.[9, 69, 73, 195] Consequently, the porosity of carbon derived from natural sources tends to be dominated by disordered micropores (diameter < 2 nm). The presence of larger mesopores (2 - 50 nm in diameter) can better facilitate gas transport and diffusion into micropores by reducing the resistance to mass transfer and pathway distance. Thus, hierarchical carbon that contains both microporosity and mesoporosity and uniform pore size is ideal for systematic adsorption.

Mesoporosity is typically obtained by templating of synthetic precursors, such as phenolic resins, furfuryl alcohol, sucrose, polyacrylonitrile, and poly divinylbenzene.[196] In particular, the mild conditions for condensation polymerization of phenolic-aldehyde resins and

the high char yield upon calcination have made this a practical precursor under a number of conditions for both soft and hard templating techniques.[108, 191] Templating methods can produce hierarchical porous carbon materials, which have proven valuable in part because the tunable pore structures are important for increased mass transport beyond the contribution from mesoporosity.[112, 197] These templating techniques are used to produce ordered mesostructures and soft-templating, where the template is removed by calcination, is the self-assembly of triblock copolymers during phase separation (*Chapter 4*). However, synthetic precursors are often expensive which can increase the cost and energy consumption due to extensive processing and purification, which can offset the beneficial $CO_2$ adsorption. Using a naturally occurring biomass *in lieu* of synthetic precursors provides a means to reduce the energy consuming steps, thereby decreasing negative environmental impact as well as decreasing cost. For example, the naturally occurring poly phenolic material, tannin, has proven to be a suitable replacement for traditional synthetic phenolic species in adhesives.[198] Using tannins as the naturally occurring biomass for ordered carbon materials provides a cost effective alternative that uses a raw material that is readily available, resulting in a greener approach for synthesizing an efficient $CO_2$ adsorbent.

Tannins are classified in two broad classes: the condensed, or polyflavonoid tannins, and the hydrolysable tannins. Condensed tannins are recognized by their oligomeric flavonoid structures. The condensed tannins are a class of catechol or flavanols and these tannins are highly reactive and have been shown to self-polymerize.[199] The hydrolysable tannins are comprised of polyphenolic substituted glucose molecules that are cleaved upon the introduction of weak acids or bases yielding gallic and ellagic acids (Figure 33). [200, 201] The gallic acid moieties

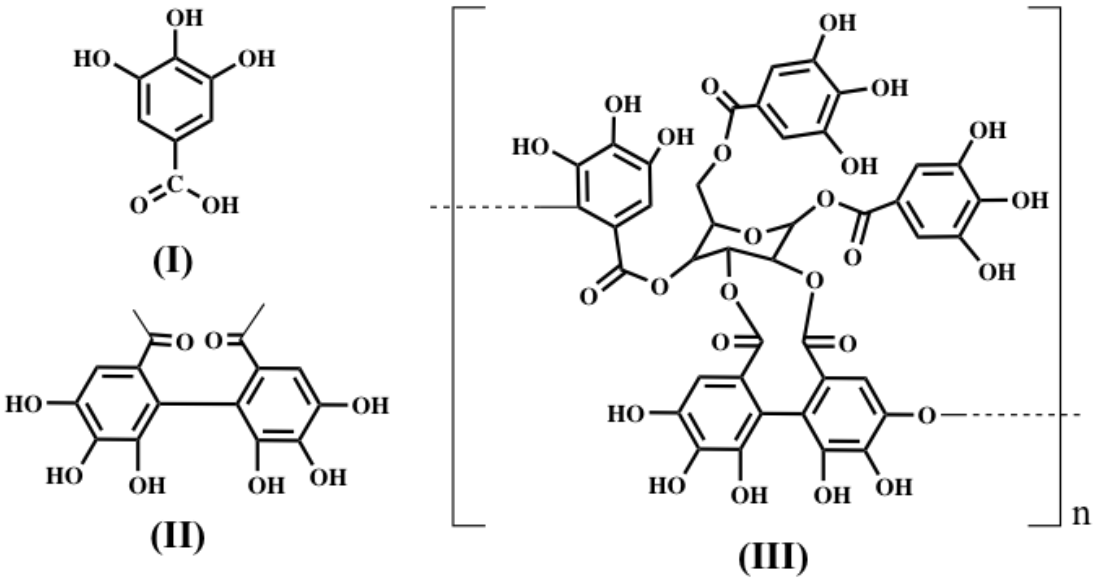


**Figure 33. Primary compounds present in hydrolysable chestnut tannin: gallic acid (I) and hexahydroxydiphenic acid (HHDP) (II) esterfied as the polyol species represented here as a polysubstituted glucose (III).**

found primarily in hydrolysable tannins exhibit a directing effect that is similar to that of resorcinol, a phenolic carbon precursor used previously in templated mesoporous carbons.[197, 202] While the two classes of tannins occur independently and are typical of a given species, both classes have a high char yield and are microporous without templating upon calcination. The acidic nature of hydrolysable tannins can be utilized in the novolac synthesis as a polymerization catalyst eliminating the need for additional acid.[200, 203-205]

In this work, we report the use of chestnut tannin (*Castanea sativa*) in a novolac type phenolic resin in a soft-templating synthesis using a polyethylene oxide–polypropylene oxide–polyethylene oxide triblock copolymer surfactant, Pluronic F127, and measured its performance as an adsorbent for $CO_2$ capture. Chestnut tannin has shown to be a suitable replacement for the phenolic with similar properties, including hydrogen bonding with the triblock copolymer template, which led to the formation of mesoporous carbon. Furthermore, ammoxidation of the mesoporous carbon derived from chestnut tannin was shown to increase both the surface area of the adsorbents and the $CO_2$ adsorption capacity and are examined in *Chapter 7*.

## 6.2 Experimental synthesis and characterization of mesoporous carbon derived from chestnut tannin

*Materials*. The triblock copolymer, Pluronic F127 ($EO_{106}PO_{70}EO_{106}$ 12600 kDa), formaldehyde solution (37 wt. % in $H_2O$, 10-15% methanol stabilized), and glyoxal solution (40 wt. % in $H_2O$) were purchased from Sigma-Aldrich Chemical Inc. Ethanol (200 proof) and concentrated

hydrochloric acid were purchased from Fisher Scientific. Chestnut tannin extract was purchased from Traditional Tanners Supply. All reagents supplied were used without further purification.

*Preparation of chestnut tannin – triblock copolymer blend.* Mesoporous carbons were synthesized by self-assembly of chestnut tannin extract (CT) and Pluronic F127 the structure-directing agent in acidic ethanol. Typically 2.52 g of Pluronic F127 dissolved in 18 g of acidic of 100 EtOH, 90 $H_2O$, and 2 HCl, by mass. After dissolution, 6 g of CT was added and stirred for a labeled period of time. The solution was then cast on a petri dish to evaporate the solvent overnight and subsequently transferred to an oven for curing at 353 K for 24 h. The samples were then calcined at 873 K for 2 h with a ramp rate of 5 K/min. The mass ratio of CT to F127 template was varied from 0.5 to 3 to study the effect on the morphology of the carbon product. Without a catalyst, the solvent was constituted using 52.6 wt.% EtOH in $H_2O$. Formaldehyde or glyoxal were added as 1:1.6 and 1:2.3 by weight, respectively, in relation to CT. The reaction time was measured from the time the cross-linker was added, or when no cross-linker present, to when chestnut tannin was added. The reaction time was varied from 40 min to up to 6 h to determine the effect of cross-linking on morphology.

Samples are designated by their CT: F127 wt. ratio, solution conditions (A-acidic or N-neutral), reaction time (in minutes), cross-linker designation (F - formaldehyde, G - glyoxal, or X - if none was used), and reaction temperature (in ºC). For example, a sample synthesized at 50 ºC under acidic conditions for 70 minutes with a CT:F127 wt. ratio of 2.38 with no cross-linker would be designated as “2.38A70X50”.

*Calcination*. Calcination occurs under flowing Ar at 873 K for 2 h with a ramp rate of 5 K/min. Activation was then performed with flowing anhydrous ammonia $NH_3$ at 1073 K with a ramp rate of 20 K/min to 1073 K and held for 20 min. Thermal cycling occurred under Ar flow. Ammonia activated samples were designated with a leading 'N' i.e. "N2.38A70X50".

*Pore and surface analysis.* Textural characterization was conducted by nitrogen adsorption and surface functionality was found using X-ray photoelectron spectroscopy.[206, 207] Nitrogen adsorption analysis was performed using a Micromeritics Tristar 3000 at 77 K. Prior to measurement, samples were degassed at 443 K for 180 min. The specific surface area was calculated using the Brunauer-Emmett-Teller (BET) equation utilizing the adsorption branch.[208] The pore size distribution plot was derived from the adsorption branch using the Barret-Joyner-Halenda (BJH) method with Kruk-Jaroniec-Sayari (KJS) method corrections.[209] Scanning electron microscopy (SEM) and transmission electron microscopy (TEM) images were obtained using a Hitachi HD 2000 STEM microscope operating at 200 kV. For micropore analysis, density functional theory (DFT) was used with adsorption isotherms acquired by a Quantachrome AS-1 using $N_2$ adsorption at 77 K after degassing the sample.

XPS analysis was performed using a PHI 3056 XPS spectrometer with an Al $K_a$ source (1486.6 eV) at a measurement pressure below $10^{-8}$ Torr. High-resolution scans were acquired at 350 W with 23.5 eV pass energy and 0.05 eV energy step. Survey scans were measured at 350 W with 93.9 eV pass energy and 0.3 eV energy step. The binding energies were shifted to account for charging by setting the main carbon signal to 284.8 eV.

*Adsorption studies*. $CO_2$ and $N_2$ adsorption isotherms were measured gravimetrically with an Intelligent Gravimetric Analyzer, Hiden IGA, using 99.995% purity $CO_2$ and >99% purity $N_2$. The uptake measurements were corrected for buoyancy of the system and samples. Samples were first degassed under vacuum at 423 K until stable weight.

By fitting the $CO_2$ adsorption isotherms from two temperatures (273 K and 298 K), the isosteric heats of adsorption ($\Delta H_{ads}$) were calculated by using the Clausius-Claperyron equation:

$$\ln\left(\frac{P_1}{P_2}\right) = \Delta H_{ads} \times \frac{T_2 - T_1}{R \times T_1 \times T_2} \tag{28}$$

where $P_1$ and $P_2$ are the pressures from the corresponding isotherms with temperatures $T_1$ and $T_2$, respectively, and $R = 8.315\ J \cdot K^{-1} mol^{-1}$.

## 6.3 Results and Discussion

A wide range of synthesis techniques were used to determine the breadth of the applicability of chestnut tannin in the phenolic-aldehyde synthesis including: weight ratio, addition of acid, and variation of cross-linking agent. All materials produced porous carbon materials. In the following sections, the relation between the porous structure and the synthesis conditions are discussed.

### 6.3.1 Synthesis of Chestnut Tannin derived Mesoporous Carbon

Soft templating of phenolic-based resins to synthesize ordered mesoporous carbon utilizes a triblock copolymer template that is removed during calcination.[210] Upon calcination at high temperatures, the heteroatoms of the triblock copolymer destabilize and leave a phenolic-based carbon inverse replica of the template structure. The hydrogen-bonding interaction between the phenolic carbon precursor and the triblock copolymer is essential for obtaining ordered pores via self-assembly of the micelles.[99, 112, 211] The polymerization of the phenol, resorcinol, and phloroglucinol with formaldehyde has been extensively studied under acidic conditions.[112, 210] Furthermore, the gallic acid present in hydrolysable tannins has been found to react similarly to that of resorcinol, which also only allows for linear polymers.[112, 202, 212] Without a template or calcination, formaldehyde cross-linked hydrolysable tannin has proven to be highly valuable as an adhesive because of strength and temperature resistance due to cross-linking showing that this material can be used for the synthesis of a carbon precursor.[201, 213]

With traditional phenolic-formaldehyde (PF) resins, the mechanism for the step-growth polymerization can be easily interpreted because of the well-defined starting product and, in turn, the ordered carbon material. Biomass is often composed of a diverse mixture of compounds that can undergo step-growth polymerization processes resulting in non-uniform structure and composition without templating. Because of this inherent heterogeneity, various mass ratios of chestnut tannin to Pluronic F127 were used to determine a ratio that could structurally withstand activation. In the typical linear novolac PF resin, polymerization occurs with an acid catalyst that increases hydrogen bonding with the polyethylene oxide (PEO) block of the template and assists

in template solubility.[99, 214] By utilizing the acidic sugars in chestnut tannin, elimination of additional acid can be achieved. Additionally, elimination of formaldehyde or substitution with a less toxic cross-linker, like glyoxal, can be implemented.[108, 215] The textural data from the $N_2$ adsorption isotherms of the resulting mesoporous carbon (Figure 34 and Figure 35) are presented in Table 7.

Previously, Wang et al. reported a soft-template approach to mesoporous carbon using resorcinol-formaldehyde resin and Pluronic F127 template.[197] While using an increased calcination temperature (1073 K), the surface area (607 $m^2/g$) and pore volume (0.58 $cm^3/g$) exceeded the values reported from this work but with an average smaller pore diameter (6.3 nm). The purity of monomers resulted in an ordered hexagonal array or pores in the resulting carbon. The ordered carbon derived from phloroglucinol-glyoxal with the Pluronic F127 template ($S_{BET}$: 410 $m^2/g$, average pore diameter: 7.5 nm) provided results more similar to those found in this work, possibly due to the more comparable steric effects presented by the phloroglucinol-glyoxal polymer.[108] The 2.38N series yielded similar pore diameters with increased deviation from the average pore size distribution from those found by Mayes et al., which can be attributed to the heterogeneity of the carbon precursor in the formation of disordered transitional domains, like those found in Figure 36 (c & d). Furthermore, when using an acid catalyst similar surface area results from are found but with an increased average pore diameter. The isotherms from these samples in Figure 35 show a steeper, asymmetric hysteresis compared to isotherms in Figure 34, characteristic of interconnected spherical shaped pores found in the disordered wormlike array found in Figure 38. The opening of the hysteresis loop at lower $P/P_o$ (~0.88 $P/P_o$) for 2.38N

**Table 7. Adsorption parameters of mesoporous carbons varying PEG: template ratio by $N_2$ adsorption at -196 °C isotherms.**

| Sample | $S_{total}$ [$m^2$ $g^{-1}$] | $S_{meso-ext.}$ [$m^2$ $g^{-1}$][b] | $S_{micro}$ [$m^2$ $g^{-1}$] | $V_{total}$ [$cm^3$ $g^{-1}$] | $V_{meso}$ [$cm^3$ $g^{-1}$] | $V_{micro}$ [$cm^3$ $g^{-1}$][c] | D nm |
|---|---|---|---|---|---|---|---|
| 1N40G30 | 420 | 159 (37.9) | 261 | 0.32 | 0.22 (68.9) | 0.11 | 10.3 |
| 1N40F30 | 402 | 147 (36.6) | 255 | 0.36 | 0.26 (72.2) | 0.10 | 12.9 |
| 1N40X30 | 242 | 75 (31.0) | 167 | 0.18 | 0.11 (61.1) | 0.067 | 16.5 |
| 1N40X50 | 322 | 64 (19.9) | 258 | 0.16 | 0.060 (37.5) | 0.10 | 18.1 |
| 2.38N80F50 | 355 | 130 (36.6) | 225 | 0.19 | 0.10 (52.6) | 0.091 | 7.8 |
| 2.38N120F30 | 338 | 125 (36.9) | 213 | 0.18 | 0.096 (53.3) | 0.086 | 7.5 |
| 2.38N240F30 | 323 | 108 (33.4) | 215 | 0.15 | 0.068 (45.3) | 0.087 | 7.4 |
| 2.38N360F30 | 364 | 152 (41.8) | 212 | 0.22 | 0.13 (59.1) | 0.086 | 7.7 |
| 0A145F65 | - | | - | | | - | - |
| 0.8A80F50 | 315 | 67 (21.3) | 248 | 0.20 | 0.096 (50.5) | 0.099 | 16.3 |
| 2.38A70G30 | 289 | 69 (23.9) | 220 | 0.16 | 0.076 (45.0) | 0.088 | 11.9 |
| 2.38A60F30 | 372 | 128 (34.4) | 244 | 0.27 | 0.168 (63.3) | 0.099 | 11.2 |
| 2.38A100F30 | 371 | 115 (31.0) | 256 | 0.19 | 0.099 (52.1) | 0.091 | 9.2 |
| 2.38A240F30 | 344 | 114 (33.1) | 230 | 0.21 | 0.11 (63.7) | 0.093 | 9.7 |
| 2.38A360F30 | 263 | 74 (28.2) | 189 | 0.14 | 0.066 (46.7) | 0.076 | 10.9 |

[a] $S_{total}$: total BET specific surface area; $S_{micro}$: micropore surface area; $S_{mest-ext}$: mesopore and external surface area; $V_{total}$: total pore volume; $V_{micro}$: micropore volume; $V_{meso}$: mesopore volume; d: mesopore size at maximum . [b] The numbers in parentheses are the percentages of surface area contributed from the mesopore and external surface area. [c] The numbers in parentheses are the percentages of mesopore volume out of the total pore volume.

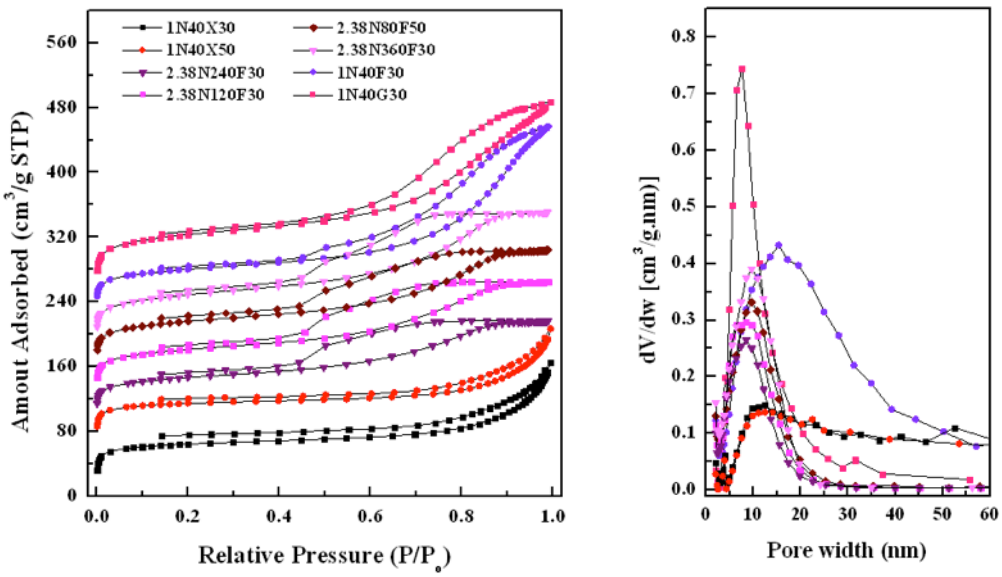


**Figure 34. Nitrogen adsorption isotherms at 77 K (left) and corresponding pore size distributions (right) of mesoporous carbon synthesized under neutral conditions prior to activation with ammonia. Isotherms offset vertically by 30 $cm^3/g$ consecutively.**

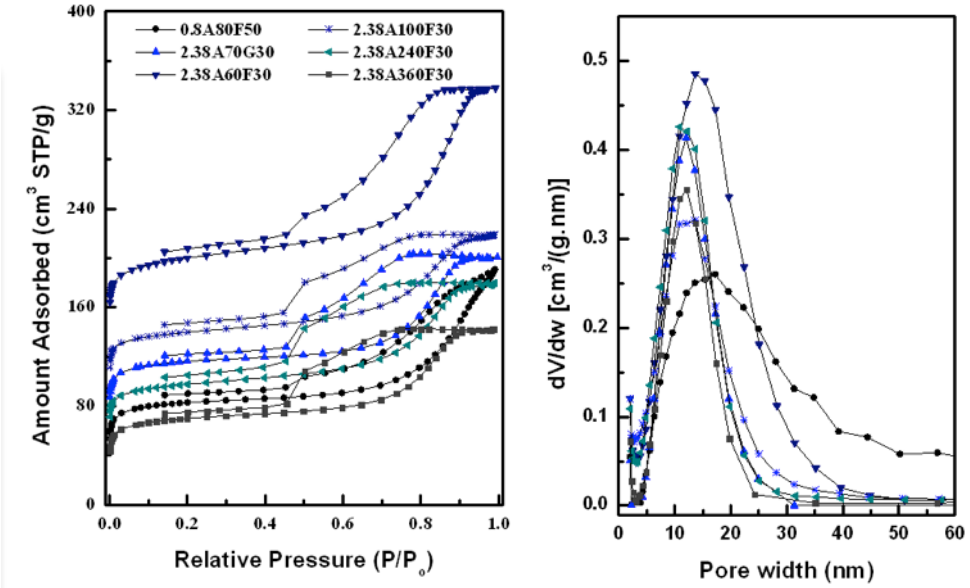


**Figure 35. Nitrogen adsorption isotherms at 77 K (left) and corresponding pore size distributions (right) of mesoporous carbon synthesized under acidic conditions prior to activation with ammonia. Isotherms offset vertically by 20 $cm^3/g$ consecutively.**

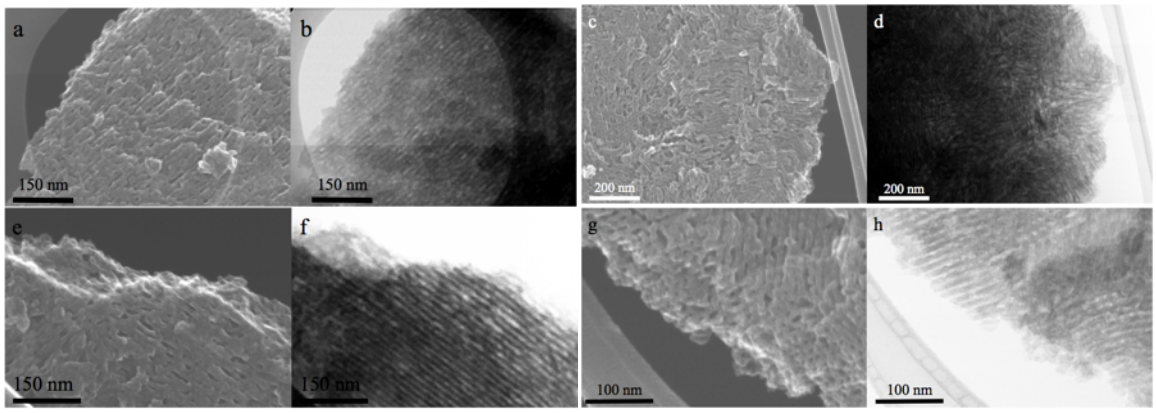


**Figure 36. SEM and TEM images of 2.38N80F50 (a) and (b), 2.38N120F30 (c) and (d), 2.38N240F30 (e) and (f), and 2.38N360F30 (g) and (h), respectively.**

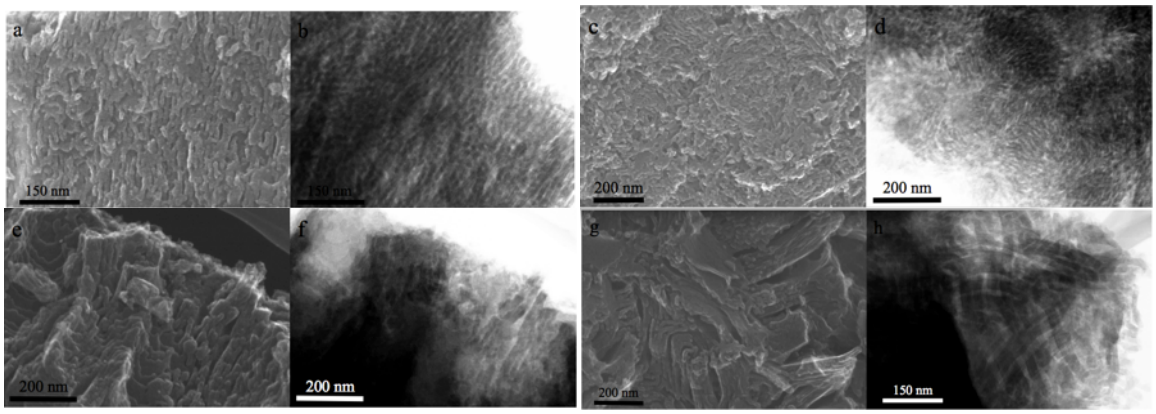


**Figure 37. SEM and TEM images of 1N40G30 (a) and (b), 1N40F30 (c) and (d), 1N40X30 (e) and (f), and 1N40X50 (g) and (h), respectively.**

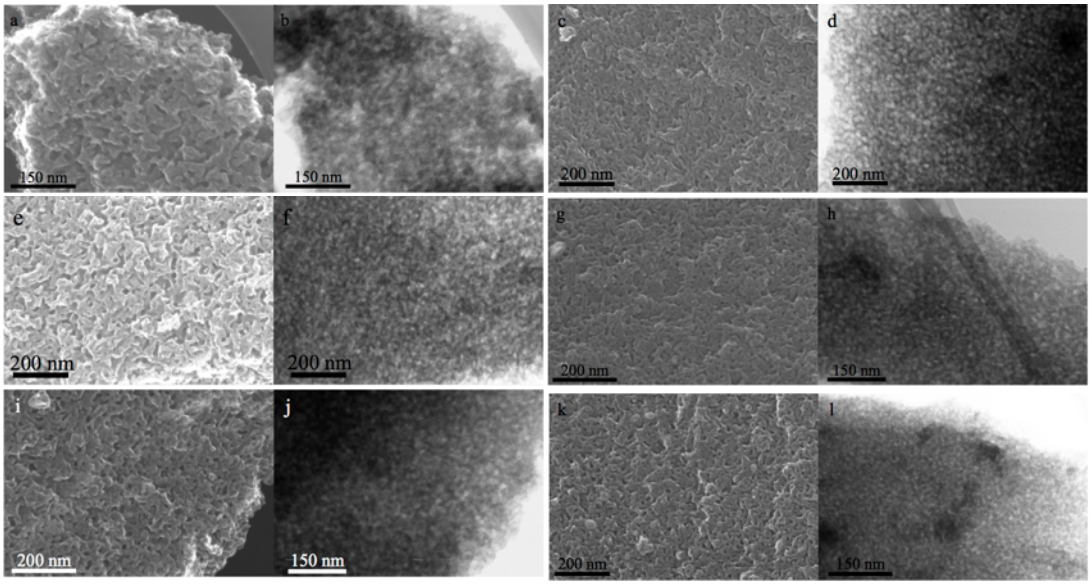


**Figure 38. SEM and TEM images of 0.8A80F50 (a) and (b), 2.38A70G30 (c) and (d), 2.38A60F30 (e) and (f), 2.38A100F30 (g) and (h), 2.38A240F30 (i) and (j), and 2.38360F30 (k) and (l), respectively.**

series compared to their acidic counterparts, 2.38A (0.90-0.92 $P/P_o$), indicates that the distribution of mesopores shifted to smaller pore diameters, which is illustrated using the BJH pore size distributions in Figure 34 and Figure 35, respectively. The closing of the hysteresis in the 2.38A series abruptly connects to the adsorption branch at ~0.45 $P/P_o$, which is indicative of cavitation due to constrictions. The broad hysteresis in the 2.38N series is typical of cylindrical pores with one end closed.[216]

The cross-linker (formaldehyde or glyoxal) has proven to be an integral part of the synthesis of specific structures. In this work, the removal of the formaldehyde cross-linker and the acid catalyst resulted in a lamellar-type layered structure (Figure 37) for samples 1N40X30 and 1N40X50. Increasing the temperature further increased the surface area, pore diameter, and mesopore volume, followed by an increased instance of voids and defects as observed in 1N40X50. Using the same ratio and no acid catalyst, the addition of a cross-linker showed the initiation of rod-like structures that exhibited a hexagonal-type array sample. Increasing the chestnut tannin ratio, polymerization time, and/or temperature consistently produced a hexagonal type array through 2.38N360F30.

Under increased pH, consistent disordered worm-like mesostructures (Figure 38) were formed under all acidic conditions. Acidic reaction conditions favor both polymerization and cleaving of gallic acid from poly substituted glucose. The number of “active” hydrogen bonding donors increases under acidic conditions, which could swell the micelles and increase the curvature forming a disordered structure.[217]

## 6.4 Conclusion

Various synthesis conditions for obtaining carbon materials using the soft templating technique and chestnut tannin have been obtained. By using biomass as a carbon precursor in lieu of phenolic-formaldehyde resin, ordered carbon structures are obtained over a range of morphologies without the use of an acid precursor. It was found that ordering can be introduced by using this technique.

# CHAPTER 7. ACTIVATION AND $CO_2$ ADSORPTION OF POROUS CARBON

*"In the case of active carbons, however, the disturbances in the elementary microcrystalline structure, due to the presence of imperfect or partially burnt graphitic layers in the crystallites, causes a variation in the arrangement of electron clouds in the carbon skeleton and results in the creation of unpaired electrons and incompletely saturated valences, and this influences the adsorption properties of active carbons, especially for polar and polarizable compounds"*

*–Bansal and Goyal, Activated Carbon Adsorption*

## 7.1 Introduction

Activation of carbon can be achieved through physical or chemical activation. Physical activation uses an agent that does not chemically react with the surface but physically bombards the surface to increase microporosity under high temperature conditions. Chemical activation uses an activating agent that can chemically react with the graphitic surface, i.e. etching, and remove atoms or molecules to create edges, i.e. micropores, to increase the surface area.

### 7.1.1 Contributing properties to selective $CO_2$ adsorption

Beyond the mere existence of pores, *Chapter 2* reviews that micropores and surface functionality both play a role in selective $CO_2$ adsorption. Through calcination, removal of the templating agent and structural heteroatoms reveals micropores in the form of edges and voids in addition to mesopore channels. Primary adsorption occurs in the microporous region where the $CO_2$ molecule can penetrate. Tuning the size of the pore allows for selective adsorption of $CO_2$ due to overlapping potential fields from the pore walls and with a kinetic diameter of 0.33 nm, the minimum pore size for slit and cylindrical pores is ~0.7-0.8 nm (ultra micropores).[23] To obtain maximum capacity, pore volume in this region maximizes the physisorption interaction energy and would exhibit increased heats of adsorption. Additionally, the presence of basic nitrogen functionality in pores of this size further increases the heat of adsorption and draws the adsorbate into the larger pores. There is a fine balance when nitrogen functionality is being added due to the increase in heat of adsorption. Beyond selective $CO_2$ adsorption, the ease of desorption for recycling of the material must also be considered. The energy cost for pressure and temperature swing adsorption can be determined for the material but is beyond the scope of this work.[218]

### 7.1.2 Physical Activation of mesoporous carbon by $CO_2$

By using a polarizable $CO_2$ under high temperatures, development of microporosity through gasification of char. The extent of activation can be measured through burn-off (BO)

percentage. A gradual pore enlargement proceeds gradually that can be firstly attributed to the removal of tar like remnants from calcination then to the widening and deepening of micropores rather than the formation of new micropores.[219] The gradual incremental pore widening can be attributed to the size of $CO_2$ and the slow process, due to the otherwise non-existent dipole moment, can be controlled in terms of hours of exposure making this method easily controllable and with relatively reproducible results.[220]

### 7.1.3 Chemical activation of mesoporous carbon

In contrast to introducing a non-reactive activating agent, chemical activation uses highly reactive agents to increase the surface area and, in some cases, use the chemical reactions to add functional groups to the surface of the carbon. The chemical activation process using high temperature conditions can be completed under flowing activating gas or impregnated with the activating agent prior to heating, where both processes involve intercalation for the development of micropores. The degree of chemical activation is a function of temperature and exposure time. Optimization of the conditions was first done for the ammonia activation technique in regards to $CO_2$ uptake capacity, while one activation using KOH was completed on the monolithic carbon due to safety concerns for large-scale synthesis.

### *$NH_3$ Activation*

Nitrogen doping of carbon surfaces has been shown to add surface basicity for adsorption of acidic $CO_2$ and several authors have studied the effects of thermal activation using ammonia on a variety of carbon sources,[70, 196, 221-223] and ammonia activation of carbon specifically applied for $CO_2$ adsorption.[57, 70, 175, 223-226] The results reported by Plaza et al. indicated that with an activation temperature of 1073 K for 2h, development of porosity in the otherwise non-porous calcined almond shells as well as the increased nitrogen content contributed to a $CO_2$ uptake capacity of ~2 mmol $g^{-1}$ at 300 K and 100 kPa.[70]

The presence of oxygen functionalities allows for tethering of the nitrogen functionality during activation, where some materials may require a pre-oxidation or simultaneous activation/oxidation step, known as ammoxidation, to retain a practical amount of the nitrogen functionality. Previously in *Chapter 4*, confirmation of oxygen content as a function of temperature allows us to carbonize at a reduced temperature to retain oxygen to allow for the exchange for nitrogen during ammonia activation.

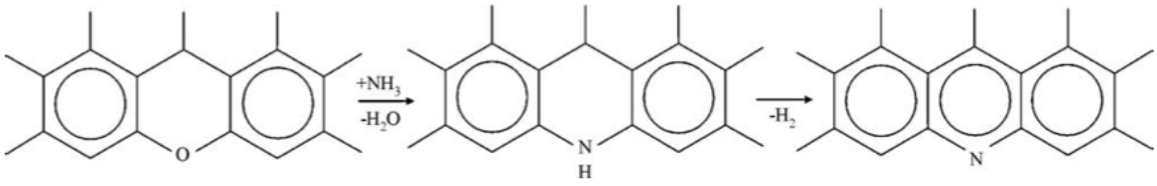


**Scheme 2. Reaction scheme for the conversion of oxygen into nitrogen moieties (imine and pyridine) upon activation with ammonia.** ***Reproduced from [15]***

***KOH Activation***

Activation with KOH is one of the most commonly used techniques for activation of carbon due to the availability of KOH and the extent of activation. The method has shown to be very useful for drastically creating microporous surface area in non-porous carbon and templated materials by the intercalation of potassium. The etching ability of the highly reactive potassium in combination with the reactivity of oxygen under high temperature conditions allows for etching beyond the capabilities of ammonia but does not have the potential for added basic functionality.

## 7.2 Materials and Characterization

The materials used in this chapter were those previously synthesized in *Chapter 4 – Meso- Macroporous Carbon Monoliths*, *Chapter 5 – PEG-PF Mesoporous Carbon,* and *Chapter 6 – Chestnut Tannin derived Mesoporous Carbon*. This section details the activation techniques for the respective carbon synthesis and the characterization techniques used to evaluate the activated carbon for $CO_2$ sequestration.

### 7.2.1 Activation of mesoporous carbon monoliths

Activation with $CO_2$ was completed according to the method described by Dai et al.[227], $CO_2$ activation was performed by placing 1.0 g of monolithic material in a tube furnace

under pure $CO_2$ flow with a heating rate of 20 $^oC$ $min^{-1}$ at 900 $^oC$ for 3.5 h. MCMs activated using $CO_2$ were labeled as such i.e. MCM-600-$CO_2$ identifies the MCM calcined at 600 $^oC$ and activated with $CO_2$.

According to the method described by Dai et al.,[227] monolithic material and KOH pellets were placed into nickel crucibles in a tube furnace under strong nitrogen flow. The material was then heated to 800 $^oC$ with a heating rate of 20 $^oC$ $min^{-1}$. The mass ratio of monolith to KOH was held at 1:8 by mass. After activation, the carbon was soaked with a 0.2 M HCl solution at 80 $^oC$ with stirring for 30 min, the samples were filtered, and dried overnight at 100 $^oC$ to remove the water. MCM-600-KOH identifies the MCM calcined at 600 $^oC$ and activated with KOH.

It should be noted that special precaution should be undertaken when doing activation of carbon with potassium. Under the high temperatures, metallic potassium is formed, which is highly reactive and flammable. When furnace cools, it is recommended that copious amounts of water vapor be bubbled with nitrogen into the system to quench the reactive potassium.

### 7.2.2 Activation of mesoporous carbon derived from novalac-polyethylene glycol blend (PF-PEG)

The activation conditions used for all PF-PEG samples were derived from the above method for $CO_2$ activation and the method from the following section: *7.2.3* Activation of mesoporous carbon derived from chestnut tannin and micellar template*,* for the ammonia activation conditions.

### 7.2.3 Activation of mesoporous carbon derived from chestnut tannin and micellar template

The activation conditions were determined as a function of uptake capacity (Figure 39). The representative sample was activated at: 500 $^{o}$C for 30 min with a ramp rate of 10 $^{o}$C/min (A), ramped to 600 $^{o}$C for 30 min then held at 900 $^{o}$C for 5 min for activation with a ramp rate of 5 $^{o}$C/min and 2 $^{o}$C/min consecutively (B), 700 $^{o}$C for 15 min with a ramp rate of 10 $^{o}$C /min (C), ramped to 600 $^{o}$C for 30 min then held at 900 $^{o}$C for 5 min for activation with a ramp rate of 20 $^{o}$C/min (D), or 800 $^{o}$C for 20 min with a ramp rate of 20 $^{o}$C/min (E). As seen in Figure 39, the maximum uptake capacity was achieved using E conditions and these were used for all the samples in the series designated with a leading 'N' i.e. "N2.38A70X50".

Textural characterization was conducted by nitrogen adsorption and surface functionality was found using X-ray photoelectron spectroscopy.[206, 207] Nitrogen adsorption analysis was performed using a Micromeritics Tristar 3000 at -196 $^{o}$C. Prior to measurement, samples were degassed at 170 $^{o}$C for 180 min or until stable weight. The specific surface area was calculated using the Brunauer-Emmett-Teller (BET) equation utilizing the adsorption branch.[208] The pore size distribution plot was derived from the adsorption branch using the Barret-Joyner-Halenda (BJH) method with Kruk-Jaroniec-Sayari (KJS) method corrections.[29] For micropore analysis, density functional theory (DFT) was used with adsorption isotherms acquired by a Quantachrome AS-1 using $N_2$ adsorption at -196 $^{o}$C after degassing the sample.

XPS analysis was performed using a PHI 3056 XPS spectrometer with an Al $K_a$ source (1486.6 eV) at a measurement pressure below $10^{-8}$ Torr. High-resolution scans were acquired at

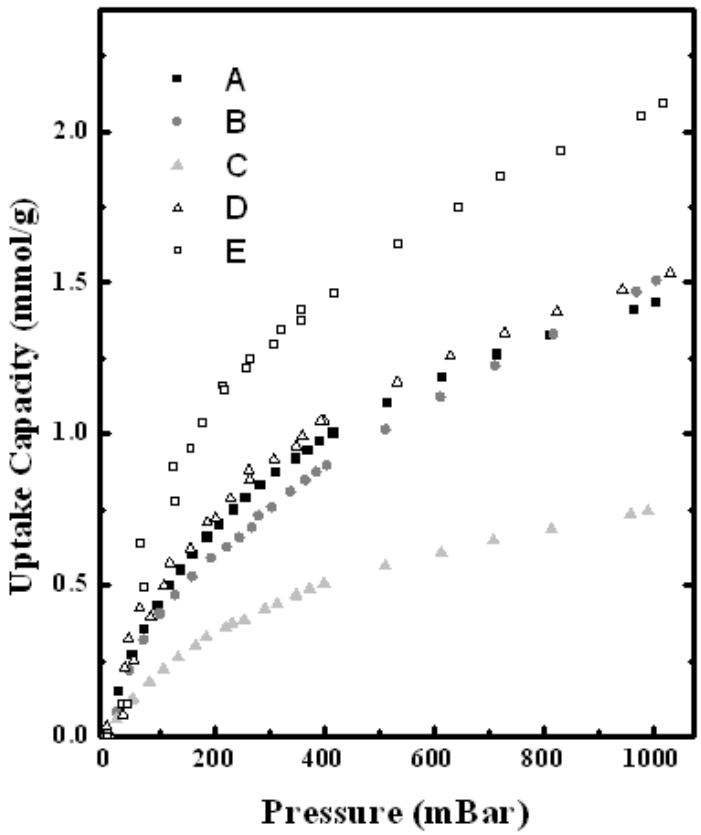


**Figure 39. Optimization of $CO_2$ adsorption *via* ammonia activation on a representative chestnut tannin derived mesoporous carbon using the Pluronic F127 template.**

350 W with 23.5 eV pass energy and 0.05 eV energy step. Survey scans were measured at 350 W with 93.9 eV pass energy and 0.3 eV energy step. The binding energies were shifted to account for charging by setting the main carbon signal to 284.8 eV.

## 7.3 Results and Discussion

The conditions used for activation of mesoporous carbon monoliths were determined for maximize the surface area *as per* work using similar the same PF polymer with Pluronic F127 template.[56] Due to the lack of specific conditions in referenced work, the conditions for $NH_3$ activation were determined through optimization of $CO_2$ uptake using a representative CT-F127 sample, resulting in maximum uptake acquired by activation at 900 $^oC$ for 20 min. The optimal activation conditions of PF-PEG samples were used from the previous determinations.

### 7.3.1 Effect of activation on mesoporous carbon monoliths

By activating the mesoporous carbon monoliths (*Chapter 4*) that were calcined at different temperatures, the change in the porous properties as a function of calcination temperature can be determined. Teng et al performed a similar procedure on a phenol-formaldehyde resin (no template) with both $CO_2$ and KOH, which demonstrated that at the same BO, $CO_2$ activation caused more of a compaction from the physical bombardment and KOH taking a more active role in creating new micropores through intercalation.[219] Although this approach used a dual calcination-activation procedure with an increased temperature ramp rate,

the results displayed a clear correlation between temperature and activating agent to carbon with increased surface area and widening of pores. At 900 $^{o}$C, calcination-activation with KOH shows a sharp decrease in surface area, where deterioration of the pore walls due to widening and exfoliation from the harsh activating agent. Previous work using the same carbon precursor and templating agent calcined at 850 $^{o}$C resulted in a $S_{total}$ = 1980 $m^2$ $g^{-1}$ for the $CO_2$ activation and $S_{Total}$ = 2037 $m^2$ $g^{-1}$ for the KOH activation. As seen in Table 8, the results for the $CO_2$ activation are consistent with the previous work; although, MCM-600-KOH showed ~1000 $m^2$ $g^{-1}$ increase in specific surface area compared to the carbon calcined at 850 $^{o}$C, demonstrating the drastic role that the oxygen content has in chemical activations.

The prepared mesoporous carbon monoliths (MCM) were first calcined and then activated. The textural results from the $N_2$ adsorption isotherms (Figure 40) at -196 $^{o}$C can be found in Table 8. The $CO_2$ adsorption capacities can be correlated to the micropore surface area, which increases to a maximum from MCM-400-$CO_2$ to MCM-600-$CO_2$ and declines with increasing temperature. The carbon that was previously calcined at lower temperatures (600 $^{o}$C and below) were annealed and, although they still contain a high amount of oxygen, the structure retained it's rigidity compared to carbon that was calcined at higher temperatures, which took on a more graphitic-like structure and when activated only continued to compress, eliminating microporous voids that were previously there. As seen in Figure 40, MCM-600-$CO_2$ only retained a small hysteresis due to widening of the mesopores.

The monoliths activated with $CO_2$ retained their structure despite the activation (Figure 41) but the intense KOH activation produced the highest specific surface and sacrificed the monolithic structure in its wake. The integrity of the macroporous structure was completely

**Table 8. Textural properties of monolithic carbon after activation**

| Adsorbent [a] [°C] | Activation method | $S_{BET}$ [$m^2 g^{-1}$] | $S_{micro}$ [$m^2 g^{-1}$] | $V_{micro}$ [$cm^3 g^{-1}$] | $CO_2$ uptake capacity [b] [mmol $g^{-1}$] |
|---|---|---|---|---|---|
| 400 | $CO_2$ | 1020 | 643 | 0.295 | 2.650 |
| 500 | $CO_2$ | 1376 | 914 | 0.419 | 2.705 |
| 600 | $CO_2$ | 1853 | 1284 | 0.582 | 3.314 |
| 700 | $CO_2$ | 1082 | 704 | 0.323 | 3.241 |
| 800 | $CO_2$ | 630 | 313 | 0.143 | 2.430 |
| 600 | KOH | 3070 | - | - | 2.958 |

[a)] Calcination temperature prior to activation. [b)] Measured at ~25 °C and 1 bar.

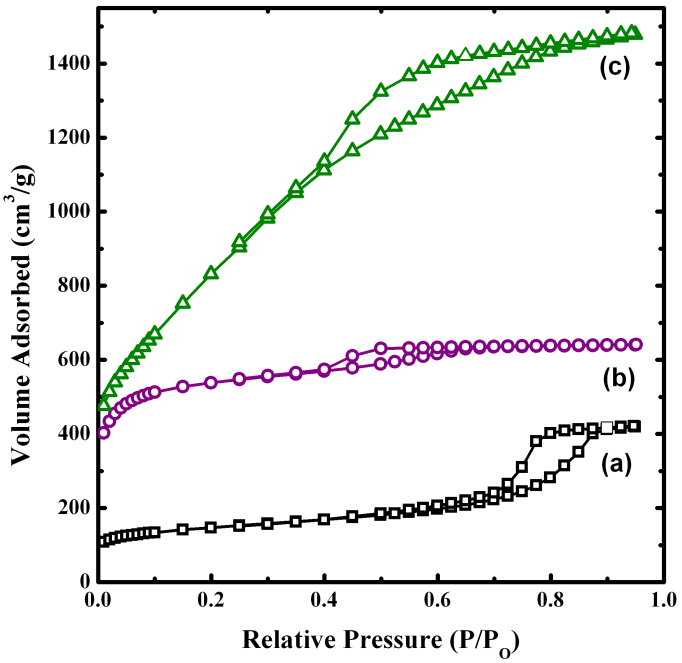


**Figure 40. $N_2$ adsorption isotherms at 77 K of MCM-600 (a), MCM-600-$CO_2$ (b), and MCM-600-KOH (c).**

**Table 9. XPS results for monolithic carbon prepared from calcination and activation of phloroglucinol-formaldehyde polymer monoliths.**

| Adsorbent [$^{o}$C] | | C1 | C2 | C3 | C4 | O1 | O2 | Total %C | Total %O |
|---|---|---|---|---|---|---|---|---|---|
| MCM-600 | *counts* | *284.74* | *286.33* | *288.69* | *290.84* | *531.81* | *533.73* | | |
| | % | 76.1 | 16.1 | 5.5 | 2.3 | 28.9 | 71.1 | 93.4 | 6.6 |
| MCM-600-$CO_2$ | *counts* | *284.8* | *26.24* | *288.66* | *290.96* | *531.81* | *533.47* | | |
| | % | 68.6 | 17.2 | 8.6 | 5.6 | 14.3 | 85.7 | 98.0 | 2.0 |
| MCM-600-KOH | *counts* | *284.79* | *286.30* | *288.51* | *290.74* | *531.31* | *533.15* | | |
| | % | 64.1 | 18.7 | 11.7 | 5.5 | 17.0 | 83.0 | 95.6 | 4.4 |

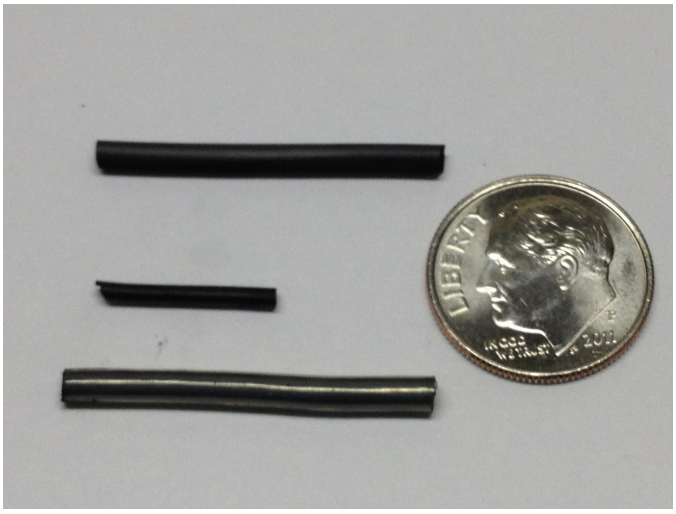


**Figure 41. Monolithic material shown after calcination (top), after CO2 activation (middle), and monolithic material after calcination in PEEK packing.**

depleted by chemical activation in all of the samples, thus rendering the KOH activation of this type of material moot and the results from the MCM-600-KOH are reported for discussion of the microporous features. This sample resulted in the highest specific surface area but the widening of the pores caused this sample to perform below the sample activated by $CO_2$.

Activation of monolithic carbon with $CO_2$ has provided the necessary microporosity to compete as an adsorbent for CCS, demonstrated by the maximum capacity achieved by MCM-600-$CO_2$ of 3.3 mmol $g^{-1}$ at ambient temperature and pressure. Although by introducing a nitrogen moiety as a basic surface group would increase adsorption capacity, the synthesis technique is laborious, requires costly precursors, and generates waste by the handling of the fragile polymer monoliths, the polymer precursors and triblock copolymer template, and the copious amounts of triethylene glycol needed for washing, respectively.

### 7.3.2 Effect of activation on PF-PEG mesoporous carbon

The carbon produced using this synthesis method provided several advantages over existing methods, which include the ability to tune the pore size and pore volume to an application. By using the spinodal decomposition approach in contrast to traditional triblock copolymer templates, there is very little evolution of microporosity upon calcination. This is in contrast to triblock copolymer templated carbon where the hydrogen bonding between the corona of the micelle with the carbon precursor forming microporous voids when the template is decomposed during calcination. Therefore for carbon dioxide and other small molecule

adsorption, activation of this type of carbon is required to achieve the microporosity for increased capture capacity.

The calcination temperature of the carbon used for activation was 600 $^{o}$C where in *Chapter 5* 800 $^{o}$C was used. In comparison to the data in Table 5 with the textural data of the PEG-PF samples calcined and activated in Table 10, the samples used for activation exhibited an increased $S_{BET}$ of ~25-30%. The microporosity increased with decreasing MW between the two calcination temperatures, whereas mesoporosity increased with increasing MW. The dominating pore sizes and the effects after calcination again corresponds to phase-separation *via* spinodal decomposition with lower MW being more miscible in the PF domains for the formation of micropores even though all MW exhibit mesoporosity. The existence of micropores at lower MW better allows for physical activation because of the availability of edges for attack and elimination of heteroatoms. Because of the smooth interface formed under spinodal decomposition, there are no interconnected micropores or deep micropores to allow for greater penetration of the activating agent. Because of the lack of this smooth interface, activation using previously determined optimal $NH_3$ activation conditions were not severe enough to exfoliate the surface to the degree found in samples found in the next section.

The activation of PF-PEG mesoporous carbon with $CO_2$ and $NH_3$ resulted in higher surface area and, specifically, microporous surface area. The textural results from the isotherms (Figure 42, Figure 43, and Figure 44) of the calcined and activated samples are found in Table 10. By activation with $CO_2$ increased microporosity is found in all the samples, where samples that used 2 kDa PEG and 8 kDa PEG nearly doubled their specific surface area, attributed by both increased micro- and mesoporosity. Under the $CO_2$ activation conditions, PF-PEG 20 kDa

**Table 10. Textural characteristics from $N_2$ adsorption at 77 K of PF-PEG carbon samples and their activation with $CO_2$ and $NH_3$.**

| MW PEG | Activation Method | $S_{BET}$ [$m^2\ g^{-1}$] | $S_{micro}$ [$m^2\ g^{-1}$] | $S_{meso}$ [$m^2\ g^{-1}$] | $V_{Total}$ [$cm^3\ g^{-1}$] | $V_{micro}$ [$cm^3\ g^{-1}$] | $V_{meso}$ [$cm^3\ g^{-1}$] | $w_{BJH}$ [nm] | $w_{peak\ max}$ [nm] | $CO_2$ uptake [mmol $g^{-1}$] |
|---|---|---|---|---|---|---|---|---|---|---|
| 2 kDa | - | 482 | 362 | 125 | 0.368 | 0.144 | 0.224 | 9.5 | 9.6 | - |
| 2 kDa | $CO_2$ | 972 | 696 | 276 | 0.679 | 0.280 | 0.398 | 7.6 | 10.5 | 2.205 |
| 2 kDa | $NH_3$ | 464 | 334 | 136 | 0.382 | 0.134 | 0.248 | 8.9 | 11.7 | 1.560 |
| 8 kDa | - | 545 | 270 | 275 | 0.856 | 0.111 | 0.745 | 14.2 | 27.5 | - |
| 8 kDa | $CO_2$ | 971 | 794 | 177 | 0.798 | 0.316 | 0.482 | 12.2 | 14.5 | 2.394 |
| 8 kDa | $NH_3$ | 563 | 382 | 186 | 0.468 | 0.154 | 0.314 | 8.24 | 10.5 | 1.835 |
| 20 kDa | - | 550 | 254 | 297 | 1.0371 | 0.105 | 0.932 | 16.6 | 35 | - |
| 20 kDa | $CO_2$ | 672 | 592 | 80 | 0.5313 | 0.235 | 0.297 | 16.6 | 20.3 | 2.057 |
| 20 kDa | $NH_3$ | 570 | 342 | 229 | 0.7843 | 0.139 | 0.645 | 13.5 | 25 | 1.816 |

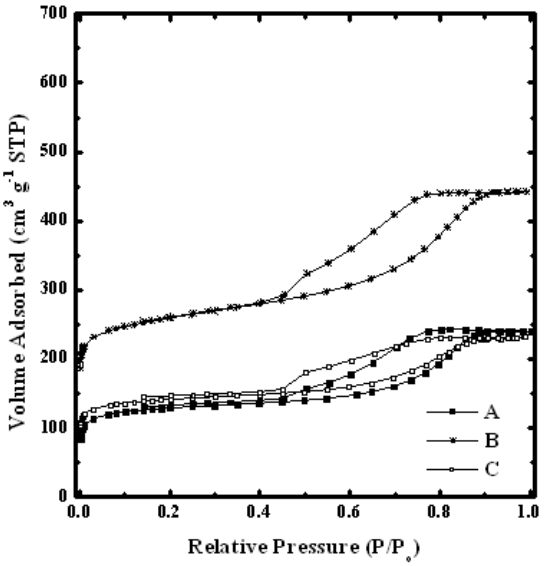


**Figure 42. Nitrogen adsorption isotherms measured at -196 °C of 2 kDa PEG-PF calcined at 600 °C (A), activated with $CO_2$ (B) or ammonia (C).**

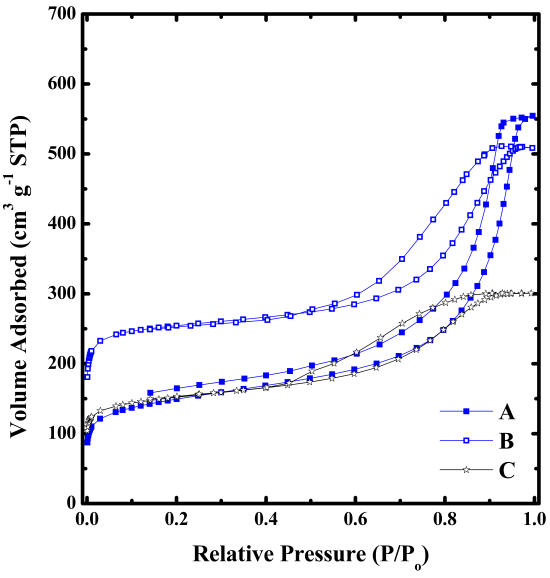


**Figure 43. Nitrogen adsorption isotherms measured at -196 °C of 8 kDa PEG-PF calcined at 600 °C (A), activated with $CO_2$ (B) or ammonia (C).**

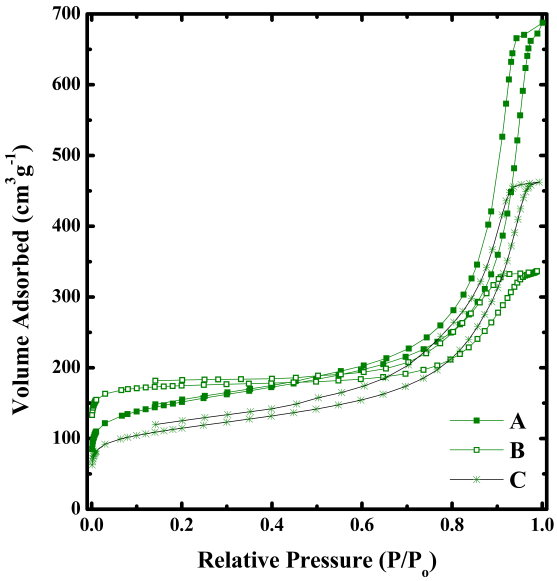


**Figure 44. Nitrogen adsorption isotherms measured at -196 °C of 20 kDa PEG-PF calcined at 600 °C (A), activated with $CO_2$ (B) or ammonia (C). Isotherms (B) and (C) offset vertically by 20 cm$^3$ g$^{-1}$ and 40 cm$^3$ g$^{-1}$, respectively.**

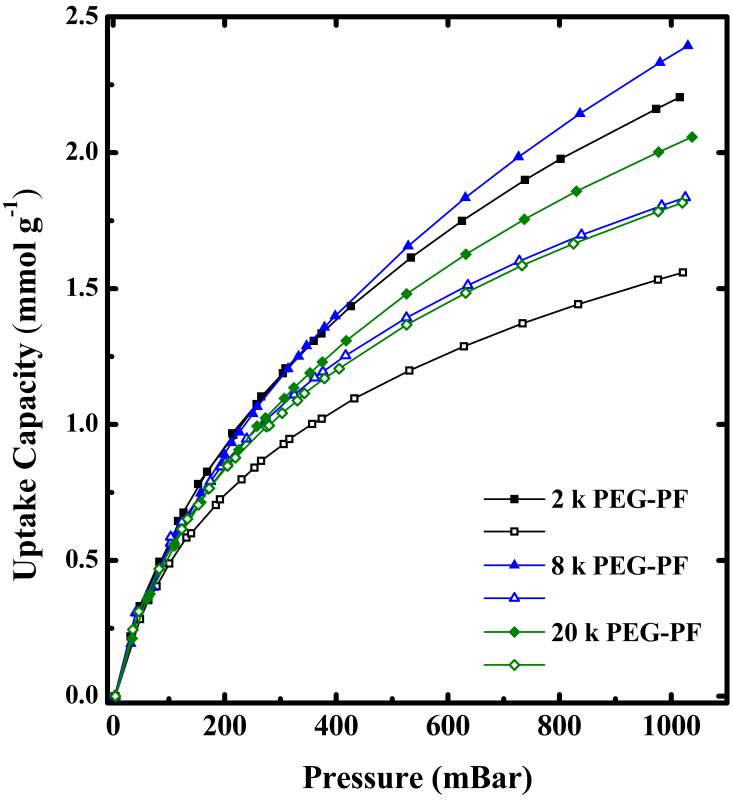


**Figure 45. $CO_2$ adsorption isotherms of $CO_2$ activated PEG-PF carbon (closed symbols) and ammonia activated PEG-PF carbon (open symbols) using the respective MW PEG.**

experienced a different effect. The larger mesopore size increased the mass transport properties by allowing for more direct and unhindered barrage of the surface, compacting the structure for micropore development at the sacrifice of mesoporosity with nearly doubling in microporosity and mesoporosity being reduced by ~75 %. The 8 k PEG-PF activated with $CO_2$ yielded the highest microporosity and subsequent maximum uptake capacity of $CO_2$ at 2.394 mmol $g^{-1}$ and when the uptake values for both activations are normalized by $CO_2$ uptake per $S_{micro}$, the ammonia-activated carbons are ~40% greater than the $CO_2$ activated samples, confirming the basic effect of added nitrogen on uptake capacity of the acidic gas.

### 7.3.3 Effect of activation on CT-F127 mesoporous carbon

Prior to activation, all samples were calcined at 873 K. At this temperature under inert Ar, calcination of the chestnut tannin polymer resin occurred with complete decomposition of the template due to the oxygen instability where it is released as both $CO_2$ and CO.[15] The tannin-based carbon was activated at high temperatures under flowing anhydrous $NH_3$ which reacts with ether-like oxygen to form imine and pyridinic nitrogen moieties on the surface and etches the carbon resulting in increased micropore surface area, reported in Table 11.[228]

Surface activation of porous carbon with ammonia is initiated by the decomposition of ammonia to free radicals, such as $NH_2$, NH, atomic hydrogen and nitrogen, which quickly attacks the carbon leading to nitrogen containing functionality.[15, 229] The increased temperature during activation destabilizes the nitrogen and only a small portion of stable nitrogen moieties remains after activation. This can prove detrimental to the surface area by

**Table 11. Textural characteristics of mesoporous carbon after amination.**

| Sample | $S_{total}$ [$m^2 g^{-1}$] | $S_{meso}$ [$m^2 g^{-1}$] | $S_{micro}$ [$m^2 g^{-1}$] | $V_{Total}$ [$cm^3 g^{-1}$] | $V_{micro}$ [$cm^3 g^{-1}$] | $w_{BJH}$ [nm] | $CO_2$ uptake [mmol $g^{-1}$] |
|---|---|---|---|---|---|---|---|
| N1N40G30 | 520 | 191 (36.7) | 329 | 0.34 | 0.13 | 7.3 | 1.807 |
| N1N40F30 | 375 | 116 (30.1) | 259 | 0.33 | 0.10 | 12.8 | 1.745 |
| N1N40X30 | 458 | 133 (29.0) | 325 | 0.22 | 0.13 | 12.7 | 1.845 |
| N1N40X50 | 533 | 100 (18.8) | 433 | 0.20 | 0.17 | 14.6 | 1.993 |
| N2.38N80F50 | 428 | 111 (25.9) | 317 | 0.17 | 0.13 | 7.9 | 1.892 |
| N2.38N120F30 | 438 | 113 (25.7) | 325 | 0.20 | 0.13 | 8.7 | 1.899 |
| N2.38N240F30 | 415 | 115 (27.7) | 300 | 0.17 | 0.12 | 7.7 | 1.873 |
| N2.38N360F30 | 700 | 219 (31.3) | 481 | 0.24 | 0.19 | 7.0 | 2.135 |
| N0A145F65 | 569 | - | - | 0.20 | 0.20 | 2.3 | 2.221 |
| N0.8A80F50 | 747 | 186 (24.9) | 561 | 0.27 | 0.22 | 10.6 | 2.265 |
| N2.38A70G30 | 689 | 195 (28.3) | 493 | 0.26 | 0.20 | 8.3 | 2.043 |
| N2.38A60F30 | 505 | 140 (27.7) | 365 | 0.27 | 0.15 | 10.0 | 2.076 |
| N2.38A100F30 | 300 | 80 (26.7) | 220 | 0.16 | 0.088 | 9.8 | 1.852 |
| N2.38A240F30 | 291 | 81 (27.8) | 210 | 0.16 | 0.085 | 10.1 | 1.873 |
| N2.38A360F30 | 355 | 94 (26.5) | 261 | 0.19 | 0.10 | 10.4 | 2.023 |

[a] $S_{total}$: total BET specific surface area; $S_{micro}$: micropore surface area; $S_{mest-ext}$: mesopore and external surface area; $V_{total}$: total pore volume; $V_{micro}$: micropore volume; $V_{meso}$: mesopore volume; $w_{BJH}$: mesopore size derived from BJH method. [b] The numbers in parentheses are the percentages of surface area contributed from the mesopore and external surface area. [c] The numbers in parentheses are the percentages of mesopore volume out of the total pore volume.

smoothing defects and edges before etching into pore walls and enlarging pore widths.[228] This is demonstrated by decreased micro- and mesoporosity in N2.38A100F30 and N2.38A240F30 from activation. Increased $CO_2$ adsorption can also be attributed to the elimination of acidic oxygen functionality and/or preservation of basic oxygen functionality due to the high temperature treatment.[230] Activation with ammonia generally led to increased surface area and nitrogen content, which gave increased $CO_2$ adsorption properties.

It is apparent that beyond the inherent porosity, the heteroatoms impact the adsorption capacity and interaction with the surface of the carbon. The samples N1N40X50, N2.38N360F30, N0.8A80F50, and N2.38A360F30 exhibited the highest adsorption of pure $CO_2$ at 100 kPa, 298 K and warranted further investigation of the interaction between the adsorbent and adsorbate through: isosteric heat, selectivity, micropore analysis, and functional group analysis *via* XPS.

The isosteric heat is used to describe the surface interactions between the adsorbent and the adsorbate. While the deconvolution of the isosteric heat is not possible to reveal the exact contribution of physisorption or chemisorption, the inherent strength of the forces in chemisorption strongly outweigh those contributed by physisorption, where values of ~40 kJ $mol^{-1}$ and above characterize primarily a chemisorption progression. Increasing isosteric heat by functionalization of the surface of porous carbons can provide a more selective approach to $CO_2$ adsorption at higher temperatures.[23] The Toth fitted adsorption isotherms (Figure 46) for $CO_2$ at 273 K and 298 K provided values to use the Clausius – Clapeyron relation yielding heats in the range off 10.7 – 29.5 kJ $mol^{-1}$ (at 15% loading). The values are well within the range for physisorption and are comparable to biomass based porous carbons activated with ammonia (21-

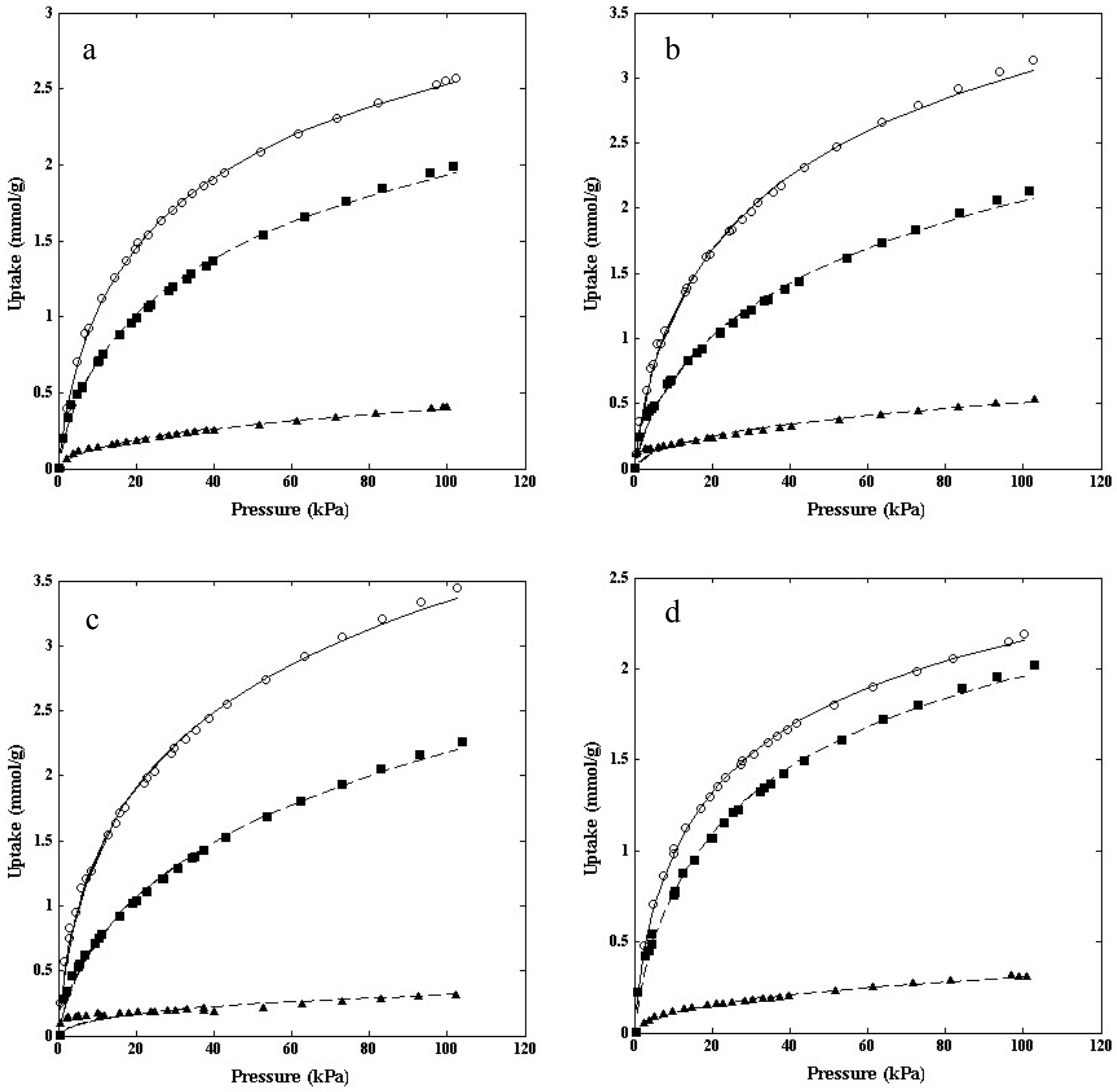


**Figure 46. Toth fitted adsorption isotherms of (a) N1N40F50, (b) N2.38N360F30, (c) N0.8A80F30, and (d) N2.38A360F30. Adsorption of $CO_2$ at 273 K (open circles) and 298 K (black squares) and $N_2$ adsorption (black triangles) with connecting line corresponding to the fitted isotherm.**

26 kJ $mol^{-1}$) and similar to carbons that include a nitrogen-containing precursor in their synthesis (19.6-26.7 kJ $mol^{-1}$).[70, 105] The sample with the highest isosteric heat (N0.8A80F30) also provided the highest selectivity, with the rest of the series following the same correlation with isosteric heat (Figure 47 and Table 12).

A micropore survey, *via* DFT pore size analysis (Figure 48), was done on these four samples to provide a better understanding on the capacity performance. In sample N2.38A360F30, only a small increase (~0.16 mmol $g^{-1}$ at 100 kPa) of the $CO_2$ adsorption is found from 273 K to 298 K, which in turn produced a low isosteric heat of adsorption as well as a low $CO_2/N_2$ selectivity for this sample. While the micropore size distribution exhibits a high pore volume at 0.5 nm to 0.65 nm, comparable to that of N2.38N360F30, it lacks a comparable pore volume from 0.7 nm to 2 nm (the supermicropore region) that is responsible for increased capacity, giving a negligible increase of uptake capacity from 298 K to 273 K. In addition to the very similar result for $CO_2$ adsorption at 298 K and 100 kPa for N1N40X50, the $CO_2$ capacity difference at 0 $^oC$ between N2.38N360F30 and N1N40X50 can be attributed to this increased pore volume difference between the two samples. In contrast, N0.8A80F50 exhibits the highest uptake capacity of $CO_2$ in the series and with an isosteric heat of 24.6 kJ $mol^{-1}$ that can be attributed to the high pore volume of supermicropores (Figure 48) in addition to the presence of nitrogen containing functionality (Table 12). Whilst functionality can enhance adsorption and selectivity, the overall capacity using this material provides a direct association with microporous pore volume in the supermicropore region at 298 K and 100 kPa.

The nature of the nitrogen species was further investigated using XPS measurements, where the nitrogen species can be deconvoluted from the N1s spectra into pyridinic nitrogen

**Table 12. $CO_2$ adsorption capacities, $CO_2/N_2$ selectivity's, $CO_2$ isosteric heat of adsorption and XPS analysis of porous carbons.**

| Sample | $CO_2$ uptake at 273 K [mmol/g, 100 kPa] | $CO_2$ uptake at 298 K [mmol/g, 100 kPa] | $CO_2/N_2$ selectivity | $Q_{st}$ [kJ/mol; @15% capacity] | % N |
|---|---|---|---|---|---|
| N1N40X50 | 2.571 | 1.993 | 8.6 | 14.8 | 6.0 |
| N2.38N360F30 | 3.136 | 2.135 | 11.9 | 22.2 | 4.3 |
| N0.8A80F50 | 3.441 | 2.266 | 14.4 | 29.5 | 4.8 |
| N2.38A360F30 | 2.189 | 2.023 | 8.5 | 10.7 | 3.4 |

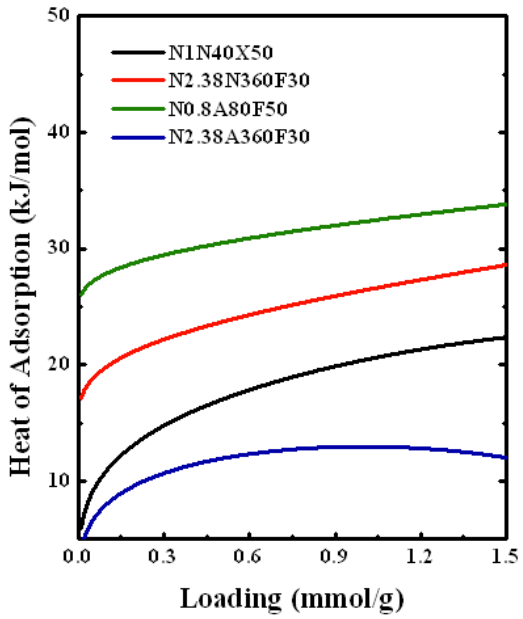


**Figure 47. Isosteric heat of adsorption for N1N40F50, N2.38N360F30, N0.8A80F30, and N2.38A360F30 at different $CO_2$ loadings.**

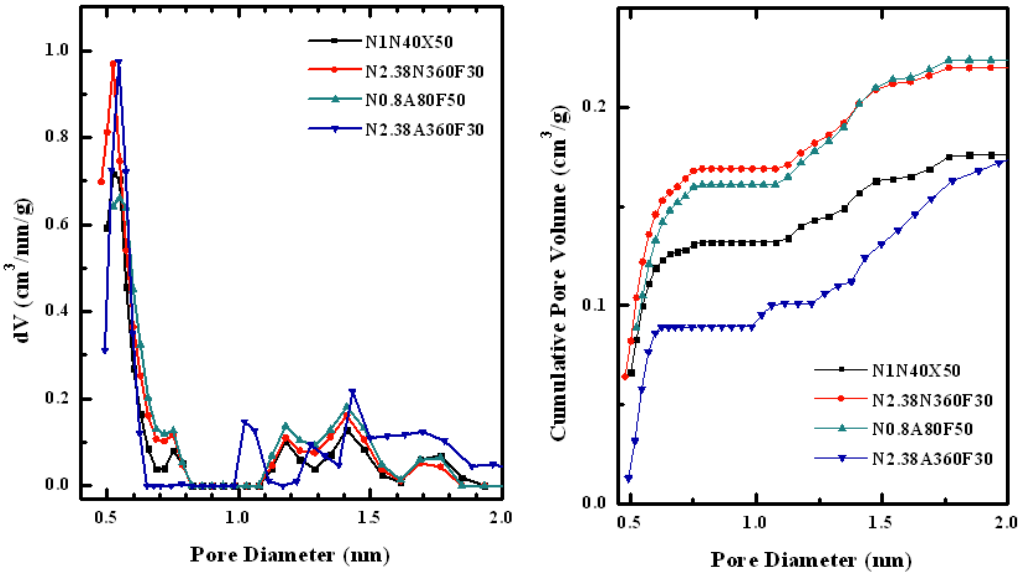


**Figure 48. DFT pore size distribution (left) and cumulative pore volume (right) derived from nitrogen adsorption at 77 K of mesoporous carbon after activation with ammonia.**

(398.4 eV), pyrrolic nitrogen (400.5 eV), and oxidized nitrogen impurities (402.7 eV). A clear distinction between the nitrogen functional groups was found between the samples without acid (Figure 49 a & b), which exhibit more of a mixture of pyridinic and pyrrolic nitrogen, where samples with an acid catalyst (Figure 49, c & d) have primarily pyridinic-like nitrogen.

## 7.4 Summary and comparison

Beyond achieving maximum adsorption capacity with a carbon material, evolution of different pore structures through activation. This was evident in the comparison between the two activations, $CO_2$ and KOH, of MCMs. Although ultra high surface area was obtained using the KOH activation, the intense conditions proved detrimental to the monolithic structure while widening the micropore size beyond the ideal size for adsorption of $CO_2$. While the $CO_2$ activation of MCMs proved near ideal for increasing the micropore surface area while preserving the monolithic structure.

In the activated samples of the PEG-PF samples, the $CO_2$ activation and the $NH_3$ both increased the microporous surface area. While using the same conditions as the MCM-600-$CO_2$, it is obvious that the there was a decreased effect of activation on the PEG-PF samples resulting in a $S_{BET}$ of only ~ 50%, ~ 60% of the $S_{micro}$, and ~70% of the $CO_2$ adsorption capacity. The highest micropore volume from the PEG-PF ammonia activated samples was 0.154 $cm^3\ g^{-1}$ and can be compared to N2.38A70G30 with a similar uptake, where both are of the disordered morphology and similar BJH pore size (~8 nm). The activation effects the pores differently in these materials, which is seen in the $CO_2$ adsorption to differ by 0.2 mmol $g^{-1}$, favoring the CT-

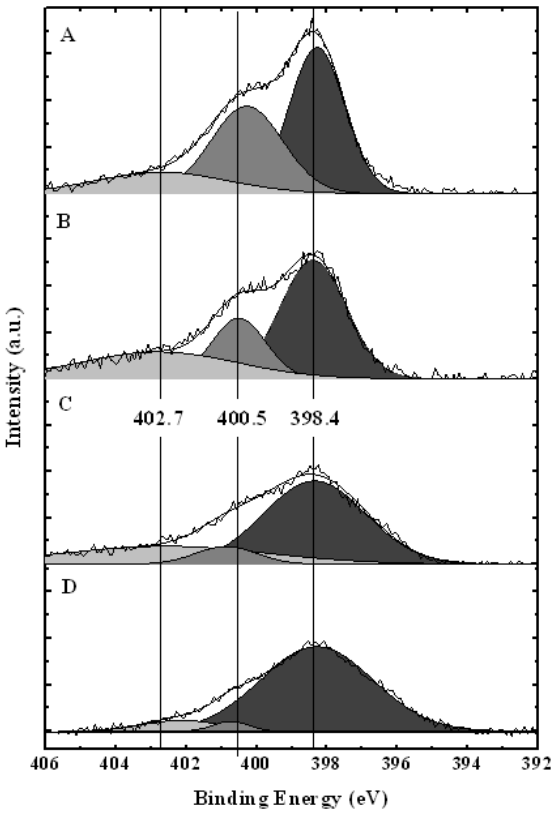


**Figure 49. N1s XPS spectra of (A) N1N40X50, (B) N2.38N360F30, (C) N0.8A0F50, and (D) N2.38N360F30.**

F127 samples. The $NH_3$ activation conditions favor the chestnut derived samples, obtaining larger pore volumes in the microporous region. The activation of chestnut tannin derived carbon with under high temperature flowing anhydrous $NH_3$ increased the adsorption capacity over its carbonized counterpart, demonstrated increased heats of adsorption, and provided a green solution to the carbon precursor.

# CHAPTER 8.
# CONCLUSIONS AND FUTURE WORK

## 8.1 Overview

The main focus of the work presented in this dissertation has been to generate and capture $CO_2$ using carbon synthesized through phase separation of polymer blends, where one polymer acts as a templating agent and the other acts as the carbon precursor. By taking advantage of thermally induced phase separation (TIPS) and polymerization induced phase separation (PIPS) homogeneous phase domains can be established and are found from the resulting carbon. Using this approach, mesoporous carbon can be produced by inducing spinodal decomposition at reflux in acidic ethanol, replacing the costly triblock copolymer template. Chestnut tannin can be used as biomass carbon precursor can be used without additional acid for ordered mesoporous carbon. The activation of carbon with potassium hydroxide, carbon dioxide and ammonia have increased the adsorption capacity of the carbon synthesized due to the increased microporosity and, in the case of ammonia, nitrogen doping. This research has demonstrated that with an analytical and environmental approach to synthesis of materials, both the environmental impact and the cost can be reduced for an industrially viable product for large-scale synthesis.

## 8.2 Investigation through established synthesis techniques

Mesoporous carbon monoliths (MCMs) were synthesized using dual phase-separation of firstly the micro-meso scale phase separation of phloroglucinol-formaldehyde (PF) and triblock copolymer, PEO-PPO-PEO Pluronic F127 (F127), and subsequent phase separation of the PF-F127 with triethylene glycol under increased temperatures. The low-pressure differential, hydrophobicity, and high chemical stability are all beneficial attributes for using MCMs for $CO_2$ sequestration. The heteroatom stability is a function of temperature and can be used to further tune the material. High concentrations of oxygen were found at lower temperatures and monoliths calcined at 773 K possessed a balance of the necessary microporosity in addition the oxygen heteroatoms for activation. The $CO_2$ and KOH activated MCM-600 yielded $S_{Total}$ of 1853 $m^2\ g^{-1}$ and 3070 $m^2\ g^{-1}$, respectively. Although the high microporosity was obtained with MCM-600-KOH, the $CO_2$ uptake at 100 kPa and 298 K was 2.958 mmol $g^{-1}$ whereas MCM-600-$CO_2$ yielded an uptake of 3.314 mmol $g^{-1}$. The lower uptake of MCM-600-KOH can be attributed to the wide pore radius from the intense activation conditions, where in contrast to large excavation of the pores, $CO_2$ activation deepened the existing pores for increased capture capacity.

## 8.3 Mesoporous carbon derived from the spinodal decomposition of PF-PEG

Mesoporous carbons were prepared using phase separation *via* spinodal decomposition. Upon dissolution of the PEG and phloroglucinol under acidic ethanol reflux conditions, the

formaldehyde cross linker was added to undergo step growth condensation polymerization. The enhanced hydrogen bonding between the phloroglucinol-formaldehyde (PF) resin and the PEG drove the blend to phase separate. Further step growth polymerization caused small concentration fluctuations that are indicative of spinodal decomposition. Spinodal decomposition was confirmed by the calcination of the solid, which revealed uniformly dispersed mesopores left by the PEG. Under these conditions, the interaction parameter of polymer blend can be utilized to tune the mesopore by the MW of the PEG in the range of 2 kDa to 200 kDa. By these means, mesopore volume can also be tuned by the PF: PEG ratio.

The low microporosity in the resulting polymer blend requires activation for increased surface area. Activation with $CO_2$ and $NH_3$ provided a high $S_{BET}$ of 971 $m^2\ g^{-1}$ and 563 $m^2\ g^{-1}$ from the 8 kDa PEG-PF carbon, respectively. The activation with $CO_2$ found the maximum $CO_2$ uptake capacity at 2.394 mmol $g^{-1}$ at 25 $^oC$ and 100 kPa; although when normalized for $S_{micro}$, higher values were found for all $NH_3$ activated samples, further research into optimal activation conditions for this type of pore structure is still required.

## 8.4 Mesoporous carbon derived from self-assembly of chestnut tannin and Pluronic F127

Mesoporous carbon samples were prepared from self-assembly of chestnut tannin extract and the triblock copolymer Pluronic F127. In ethanol-water solution, control over morphology (lamellar-like, hexagonal-like, and worm-like) is found by the CT: F127 ratio without the addition of acid. In fact, addition of acid only produces worm-like structures upon calcination.

Activation of CT-F127 carbon yields, in general, increased uptake of $CO_2$. The effect of $NH_3$ activation on the different precursor carbon ranges drastically, which can be due to the heterogeneous nature of the carbon precursor. Furthermore, the highest uptake capacity is found by a worm-like sample, N0.8A80F50, of 2.265 mmol $g^{-1}$ with a $S_{BET}$ of 747 $m^2$ $g^{-1}$. Further work utilizing this carbon precursor material with PEG as the mesopore templating agent would completely renovate the previous synthesis method. The synthesis method would: minimize the use of acid, the capital loss due to sacrificial template would be minimized, and the biomass precursor could be obtained on a large scale.

## 8.5 Future Work

The work completed in this dissertation encompasses a portion of the total collaborative effort for investigation into porous carbon. Several other efforts have been made for utilization of: N-doped carbons membranes,[231] microporous polymer membranes,[41, 232] amidoxime modification of porous carbon,[233] and carbon membranes as ionic liquid supports[234] for $CO_2$ separation. The capabilities of membrane technology warrant further research of the carbon researched in this dissertation as a separation medium (gas or liquid) and as a support medium for polymers or ionic liquids. Because of the conductivity of porous carbon materials, atomic layer deposition (ALD) onto carbon is possible and the ability to tune the porosity to optimize penetration into the high surface area structure is another avenue for future work with the PEG-PF carbon.

## 8.6 Summary

The research in this dissertation focused on the development of green synthesis techniques of mesoporous carbon to be utilized as post combustion $CO_2$ capture materials. By tuning the carbonization temperature, the pre-oxidation step for activation can be nullified. Utilizing polymer blend separation techniques, I have introduced a new synthetic approach to templating using easily synthesized and readily available linear poly (ethylene glycol) that is more economically suited as a sacrificial templating agent. By using the biomass carbon precursor chestnut tannin, I have shown that self-assembly occurs without additional acid. These concepts provide an example of synthesis and potential development of a material with environmental aspects at the forefront so that the means justify the end product.

# LIST OF REFERENCES

[1] Climate change: How do we know? Global Climate Change: Vital Signs of the Planet [cited; Available from: climate.nasa.gov/evidence

[2] Overview of Greenhouse Gases. Climate Change April 15, 2014 [cited 2014; Available from: http://www.epa.gov/climatechange/ghgemissions/gases.html

[3] Garrett CW. On global climate change, carbon-dioxide, and fossil-fuel combustion. Progr Energy Combust Sci. 1992;18(5):369-407.

[4] Orr FMJ. CO2 capture and storage: are we ready? Eng Env Sci. 2009;2(5):449-58.

[5] Clean Air Act 42. USC 1970, p. 7401 et seq.

[6] Campbell RJ. Increasing the Efficiency of Existing Coal-Fired Power Plants: Congressional Research Service; 2013.

[7] Administrtion USEI. AEO2014 Early Release Overview; 2013 Dec 13.

[8] Zhu G, Zhu X, Xiao Z, Zhou R, Yi F. Pyrolysis characteristics of bean dregs and in situ visualization of pyrolysis transformation. Waste Manag. 2012:1-7.

[9] Wang YX, Liu BS, Zheng C. Preparation and Adsorption Properties of Corncob-Derived Activated Carbon with High Surface Area. J Chem Eng Data. 2010;55(11):4669-76.

[10] Tseng R-L, Tseng S-K. Pore structure and adsorption performance of the KOH-activated carbons prepared from corncob. J Colloid Interface Sci. 2005;287(2):428-37.

[11] Tsai WT, Chang CY, Lee SL. A low cost adsorbent from agricultural waste corn cob by zinc chloride activation. Bioresour Technol. 2003;64(3):211-7.

[12] Rodriguez-Reinoso F, de D Lopez-Gonzalez J, Berenguer C. Activated carbons from almond shells—I: preparation and characterization by nitrogen adsorption. Carbon. 1982;20(6):513-8.

[13] Plaza MG, Pevida C, Martín CF, Fermoso J, Pis JJ, Rubiera F. Developing almond shell-derived activated carbons as CO2 adsorbents. Sep Purif Technol. 2010;71(1):102-6.

[14] Hu ZH, Srinivasan MP, Ni YM. Novel activation process for preparing highly microporous and mesoporous activated carbons. Carbon. 2001;39(6):877-86.

[15] Shafeeyan MS, Daud WMAW, Houshmand A, Shamiri A. A review on surface modification of activated carbon for carbon dioxide adsorption. J Anal Appl Pyrol. 2010;89(2):143-51.

[16] Bansal RC, Goyal M. Activated Carbon Adsorption. Boca Raton, FL: CRC Press; 2005.

[17] Franklin RE. Crystallite Growth in Graphitizing and Non-Graphitizing Carbons. Proc R Soc A. 1951;209(1097):196-218.

[18] Wilcox J. Carbon Capture; 2012.

[19] Lowell S, Shields JE, Thomas M, Thomas M. Characterization of porous solids and powders: Surface area, pore size and density. Dordrecht, The Netherlands: Kluwer Academic Publishers; 2004.

[20] Do DD. Adsorption Analysis: Equilibria and Kinetics. London: Imperial College Press; 1998.

[21] Attard G, Barnes C. Surfaces. New York: Oxford University Press Inc. ; 1998.

[22] Thommes M. Micropore analysis. In: Lowell S, Shields JE, Thomas M, Thommes M, eds. Characterization of Porous Solids and Powders: surface area, pore size, and density. Dordrecht, The Netherlands: Kluwer Academic Publishers 2003, p. 1-29.

[23] Sevilla M, Parra JB, Fuertes AB. Assessment of the Role of Micropore Size and N-Doping in CO2 Capture by Porous Carbons. ACS Appl Mater Interfaces. 2013;5(13):6360-8.

[24] House KZ, Harvey CF, Aziz MJ, Schrag DP. The energy penalty of post-combustion CO2 capture & storage and its implications for retrofitting the US installed base. Eng Env Sci. 2009;2(2):193-205.

[25] Veltman K, Singh B, Hertwich EG. Human and Environmental Impact Assessment of Postcombustion CO2 Capture Focusing on Emissions from Amine-Based Scrubbing Solvents to Air. Environ Sci Technol. 2010;44(4):1496-502.

[26] Orr FM, Jr. CO2 capture and storage: are we ready? Energy Environ Sci. 2009;2(5):449-58.

[27] Aaron D, Tsouris C. Separation of CO2 from flue gas: A review. Sep Sci Technol. 2005;40(1-3):321-48.

[28] Brennecke JE, Gurkan BE. Ionic Liquids for CO(2) Capture and Emission Reduction. J Phys Chem. 2010;1(24):3459-64.

[29] Kruk M, Jaroniec M. Gas adsorption characterization of ordered organic-inorganic nanocomposite materials. Chem Mat. 2001;13(10):3169-83.

[30] Sing KSW, Everett DH, Haul RAW, Moscou L, Pierotti RA, Rouquerol J, et al. Reporting physisorption data for gas solid systems with special reference to the determination of surface-area and porosity (recommendations 1984). Pure Appl Chem. 1985;57(4):603-19.

[31] D'Alessandro DM, Smit B, Long JR. Carbon Dioxide Capture: Prospects for New Materials. Angew Chem. 2010;49(35):6058-82.

[32] Millward AR, Yaghi OM. Metal-organic frameworks with exceptionally high capacity for storage of carbon dioxide at room temperature. J Am Chem Soc. 2005;127(51):17998-9.

[33] Wang B, Cote AP, Furukawa H, O'Keeffe M, Yaghi OM. Colossal cages in zeolitic imidazolate frameworks as selective carbon dioxide reservoirs. Nature. 2008;453(7192):207-12.

[34] Li J-R, Sculley J, Zhou H-C. Metal-Organic Frameworks for Separations. Chem Rev (Washington, DC, U S). 2012;112(2):869-932.

[35] Sumida K, Rogow DL, Mason JA, McDonald TM, Bloch ED, Herm ZR, et al. Carbon Dioxide Capture in Metal-Organic Frameworks. Chem Rev (Washington, DC, U S). 2012;112(2):724-81.

[36] McDonald TM, Lee WR, Mason JA, Wiers BM, Hong CS, Long JR. Capture of Carbon Dioxide from Air and Flue Gas in the Alkylamine-Appended Metal–Organic Framework mmen-Mg2(dobpdc). J Am Chem Soc. 2012;134(16):7056-65.

[37] Dawson R, Adams DJ, Cooper AI. Chemical tuning of CO2 sorption in robust nanoporous organic polymers. Chem Sci. 2011;2(6):1173-5.

[38] Dawson R, Stockel E, Holst JR, Adams DJ, Cooper AI. Microporous organic polymers for carbon dioxide capture. Eng Env Sci. 2011;4(10):4239-45.

[39] Du N, Park HB, Robertson GP, Dal-Cin MM, Visser T, Scoles L, et al. Polymer nanosieve membranes for CO2-capture applications. Nat Mater. 2011;10(5):372-5.

[40] Lu W, Yuan D, Sculley J, Zhao D, Krishna R, Zhou H-C. Sulfonate-Grafted Porous Polymer Networks for Preferential CO(2) Adsorption at Low Pressure. J Am Chem Soc. 2011;133(45):18126-9.

[41] Zhu X, Tian C, Mahurin SM, Chai S-H, Wang C, Brown S, et al. A Superacid-Catalyzed Synthesis of Porous Membranes Based on Triazine Frameworks for CO2 Separation. J Am Chem Soc. 2012;134(25):10478-84.

[42] Lu W, Sculley JP, Yuan D, Krishna R, Wei Z, Zhou H-C. Polyamine-Tethered Porous Polymer Networks for Carbon Dioxide Capture from Flue Gas. Angew Chem, Int Ed. 2012;51(30):7480-4.

[43] Hicks JC, Drese JH, Fauth DJ, Gray ML, Qi G, Jones CW. Designing adsorbents for CO2 capture from flue gas-hyperbranched aminosilicas capable of capturing CO2 reversibly. J Am Chem Soc. 2008;130(10):2902-3.

[44] Choi S, Drese JH, Jones CW. Adsorbent Materials for Carbon Dioxide Capture from Large Anthropogenic Point Sources. ChemSusChem. 2009;2(9):796-854.

[45] Ma X, Wang X, Song C. "Molecular Basket" Sorbents for Separation of CO2 and H2S from Various Gas Streams. J Am Chem Soc. 2009;131(16):5777-83.

[46] Goeppert A, Czaun M, May RB, Prakash GKS, Olah GA, Narayanan SR. Carbon Dioxide Capture from the Air Using a Polyamine Based Regenerable Solid Adsorbent. J Am Chem Soc. 2011;133(50):20164-7.

[47] Kuwahara Y, Kang D-Y, Copeland JR, Brunelli NA, Didas SA, Bollini P, et al. Dramatic Enhancement of CO 2Uptake by Poly(ethyleneimine) Using Zirconosilicate Supports. J Am Chem Soc. 2012:120620103107004.

[48] Sevilla M, Valle-Vigon P, Fuertes AB. N-Doped Polypyrrole-Based Porous Carbons for CO(2) Capture. Adv Funct Mater. 2011;21(14):2781-7.

[49] Hao GP, Li WC, Qian D, Lu AH. Rapid Synthesis of Nitrogen-Doped Porous Carbon Monolith for CO(2) Capture. Adv Mater (Weinheim, Ger). 2010;22(7):853-7.

[50] Svendsen HF, Hessen ET, Mejdell T. Carbon dioxide capture by absorption, challenges and possibilities. Chem Eng J (Lausanne). 2011;171(3):718-24.

[51] Siriwardane RV, Shen M-S, Fisher EP, Poston JA. Adsorption of CO2 on Molecular Sieves and Activated Carbon. Energy Fuels. 2001;15(2):279-84.

[52] Arrigo R, Haevecker M, Wrabetz S, Blume R, Lerch M, McGregor J, et al. Tuning the Acid/Base Properties of Nanocarbons by Functionalization via Amination. J Am Chem Soc. 2010;132(28):9616-30.

[53] Xing W, Liu C, Zhou Z, Zhang L, Zhou J, Zhuo S, et al. Superior CO2 uptake of N-doped activated carbon through hydrogen-bonding interaction. Eng Env Sci. 2012;5(6):7323.

[54] Hayashi J, Kazehaya A, Muroyama K, Watkinson AP. Preparation of activated carbon from lignin by chemical activation. Carbon. 2000;38(13):1873-8.

[55] Fulvio PF, Lee JS, Mayes RT, Wang X, Mahurin SM, Dai S. Boron and nitrogen-rich carbons from ionic liquid precursors with tailorable surface properties. Phys Chem Chem Phys. 2011;13(30):13486.

[56] Wang X, Lee JS, Tsouris C, DePaoli DW, Dai S. Preparation of activated mesoporous carbons for electrosorption of ions from aqueous solutions. J Mater Chem. 2010;20(22):4602-7.

[57] Zhang Z, Xu M, Wang H, Li Z. Enhancement of CO2 adsorption on high surface area activated carbon modified by N-2, H-2 and ammonia. Chem Eng J (Lausanne). 2010;160(2):571-7.

[58] Shafeeyan MS, Daud WMAW, Houshmand A, Arami-Niya A. The application of response surface methodology to optimize the amination of activated carbon for the preparation of carbon dioxide adsorbents. Fuel. 2012;94(C):465-72.

[59] White RJ, Budarin V, Luque R, Clark JH, Macquarrie DJ. Tuneable porous carbonaceous materials from renewable resources. Chem Soc Rev. 2009;38(12):3401.

[60] Cazorla-Amoros D, Alcaniz-Monge J, de la Casa-Lillo MA, Linares-Solano A. CO2 as an adsorptive to characterize carbon molecular sieves and activated carbons. Langmuir. 1998;14(16):4589-96.

[61] Meng LY, Park SJ. Investigation of Narrow Pore Size Distribution on Carbon Dioxide Capture of Nanoporous Carbons. Bull Korean Chem Soc. 2012;33(11):3749-54.

[62] Martin CF, Plaza MG, Garcia S, Pis JJ, Rubiera F, Pevida C. Microporous phenol-formaldehyde resin-based adsorbents for pre-combustion CO2 capture. Fuel. 2011;90(5):2064-72.

[63] Carruthers JD, Petruska MA, Sturm EA, Wilson SM. Molecular sieve carbons for CO2 capture. Microporous Mesoporous Mater. 2012;154(C):62-7.

[64] Sevilla M, Fuertes AB. CO2 adsorption by activated templated carbons. J Colloid Interface Sci. 2012;366(1):147-54.

[65] Meng L-Y, Park S-J. Influence of MgO template on carbon dioxide adsorption of cation exchange resin-based nanoporous carbon. J Colloid Interface Sci. 2012;366(1):125-9.

[66] Wang LF, Yang RT. Significantly Increased CO2 Adsorption Performance of Nanostructured Templated Carbon by Tuning Surface Area and Nitrogen Doping. J Phys Chem C. 2012;116(1):1099-106.

[67] Builes S, Roussel T, Ghimbeu CM, Parmentier J, Gadiou R, Vix-Guterl C, et al. Microporous carbon adsorbents with high CO2 capacities for industrial applications. Phys Chem Chem Phys. 2011;13(35):16063.

[68] Sevilla M, Fuertes AB. Sustainable porous carbons with a superior performance for CO2 capture. Energy & Environ Sci. 2011;4(5):1765.

[69] Wang Z, Zhan L, Ge M, Xie F, Wang Y, Qiao W, et al. Pith based spherical activated carbon for CO2 removal from flue gases. Chem Eng Sci. 2011;66(22):5504-11.

[70] Plaza MG, Garcia S, Rubiera F, Pis JJ, Pevida C. Evaluation of ammonia modified and conventionally activated biomass based carbons as CO2 adsorbents in postcombustion conditions. Sep Purif Technol. 2011;80(1):96-104.

[71] Boonpoke A, Chiarakorn S, Laosiripojana N, Towprayoon S, Chidthaisong A. Investigation of CO2 adsorption by bagasse-based activated carbon. Korean J Chem Eng. 2012;29(1):89-94.

[72] Yang H, Gong M, Chen Y. Preparation of activated carbons and their adsorption properties for greenhouse gases: CH4 and CO2. J Nat Gas Chem. 2011;20(5):460-4.

[73] Wang JC, Heerwig A, Lohe MR, Oschatz M, Borchardt L, Kaskel S. Fungi-based porous carbons for CO2 adsorption and separation. J Mater Chem. 2012;22(28):13911-3.

[74] Wang YX, Liu BS, Zheng C. Preparation and Adsorption Properties of Corncob-Derived Activated Carbon with High Surface Area. J Chem Eng Data. 2010;55(11):4669-76.

[75] Tseng RL, Tseng SK. Pore structure and adsorption performance of the KOH-activated carbons prepared from corncob. J Colloid Interface Sci. 2005;287(2):428-37.

[76] Zhang Z, Wang K, Atkinson JD, Yan X, Li X, Rood MJ, et al. Sustainable and hierarchical porous Enteromorpha prolifera based carbon for CO2 capture. J Hazard Mater. 2012;229-230:183-91.

[77] Teng HS, Wang SC. Preparation of porous carbons from phenol-formaldehyde resins with chemical and physical activation. Carbon. 2000;38(6):817-24.

[78] Kilic M, Apaydin-Varol E, Putun AE. Preparation and surface characterization of activated carbons from Euphorbia rigida by chemical activation with ZnCl2, K2CO3, NaOH and H3PO4. Appl Surf Sci. 2012;261:247-54.

[79] Maroto-Valer MM, Tang Z, Zhang YZ. CO2 capture by activated and impregnated anthracites. Fuel Process Technol. 2005;86(14-15):1487-502.

[80] Wang Z, Zhan L, Ge M, Xie F, Wang Y, Qiao W, et al. Pith based spherical activated carbon for CO2 removal from flue gases. Chem Eng Sci. 2011;66(22):5504-11.

[81] Rodriguezreinoso F, Molinasabio M, Gonzalez MT. THE USE OF STEAM AND CO2 AS ACTIVATING AGENTS IN THE PREPARATION OF ACTIVATED CARBONS. Carbon. 1995;33(1):15-23.

[82] Pilato L. Phenolic resins : a century of progress. Heidelberg; New York: Springer; 2010.

[83] Perez-Ramirez J, Christensen CH, Egeblad K, Christensen CH, Groen JC. Hierarchical zeolites: enhanced utilisation of microporous crystals in catalysis by advances in materials design. Chem Soc Rev. 2008;37(11):2530-42.

[84] Xia YD, Yang ZX, Mokaya R. Templated nanoscale porous carbons. Nanoscale. 2010;2(5):639-59.

[85] Kruk M, Dufour B, Celer EB, Kowalewski T, Jaroniec M, Matyjaszewski K. Synthesis of mesoporous carbons using ordered and disordered mesoporous silica templates and polyacrylonitrile as carbon precursor. J Phys Chem B. 2005;109(19):9216-25.

[86] Pevida C, Drage TC, Snape CE. Silica-templated melamine-formaldehyde resin derived adsorbents for CO2 capture. Carbon. 2008;46(11):1464-74.

[87] Jun S, Joo SH, Ryoo R, Kruk M, Jaroniec M, Liu Z, et al. Synthesis of New, Nanoporous Carbon with Hexagonally Ordered Mesostructure. J Am Chem Soc. 2000;122(43):10712-3.

[88] Ryoo R, Joo SH, Jun S. Synthesis of Highly Ordered Carbon Molecular Sieves via Template-Mediated Structural Transformation. J Phys Chem B. 1999;103(37):7743-6.

[89] Nishihara H, Yang Q-H, Hou P-X, Unno M, Yamauchi S, Saito R, et al. A possible buckybowl-like structure of zeolite templated carbon. Carbon. 2009;47(5):1220-30.

[90] Kruk M, Jaroniec M, Kim TW, Ryoo R. Synthesis and characterization of hexagonally ordered carbon nanopipes. Chem Mat. 2003;15(14):2815-23.

[91] Kaneda M, Tsubakiyama T, Carlsson A, Sakamoto Y, Ohsuna T, Terasaki O, et al. Structural study of mesoporous MCM-48 and carbon networks synthesized in the spaces of MCM-48 by electron crystallography. J Phys Chem B. 2002;106(6):1256-66.

[92] Solovyov LA, Zaikovskii VI, Shmakov AN, Belousov OV, Ryoo R. Framework characterization of mesostructured carbon CMK-1 by X-ray powder diffraction and electron microscopy. J Phys Chem B. 2002;106(47):12198-202.

[93] Ryoo R, Joo SH, Kruk M, Jaroniec M. Ordered mesoporous carbons. Adv Mater (Weinheim, Ger). 2001;13(9):677-81.

[94] Gierszal KP, Jaroniec M. Carbons with extremely large volume of uniform mesopores synthesized by carbonization of phenolic resin film formed on colloidal silica template. J Am Chem Soc. 2006;128(31):10026-7.

[95] Yoon SB, Chai GS, Kang SK, Yu JS, Gierszal KP, Jaroniec M. Graphitized pitch-based carbons with ordered nanopores synthesized by using colloidal crystals as templates. J Am Chem Soc. 2005;127(12):4188-9.

[96] Li ZJ, Jaroniec M. Synthesis and adsorption properties of colloid-imprinted carbons with surface and volume mesoporosity. Chem Mat. 2003;15(6):1327-33.

[97] Li ZJ, Jaroniec M. Colloidal imprinting: A novel approach to the synthesis of mesoporous carbons. J Am Chem Soc. 2001;123(37):9208-9.

[98] Wang XQ, Liang CD, Dai S. Facile synthesis of ordered mesoporous carbons with high thermal stability by self-assembly of resorcinol-formaldehyde and block copolymers under highly acidic conditions. Langmuir. 2008;24(14):7500-5.

[99] Liang CD, Dai S. Synthesis of mesoporous carbon materials via enhanced hydrogen-bonding interaction. J Am Chem Soc. 2006;128(16):5316-7.

[100] Liang CD, Hong KL, Guiochon GA, Mays JW, Dai S. Synthesis of a large-scale highly ordered porous carbon film by self-assembly of block copolymers. Angew Chem, Int Ed. 2004;43(43):5785-9.

[101] Meng Y, Gu D, Zhang FQ, Shi YF, Cheng L, Feng D, et al. A family of highly ordered mesoporous polymer resin and carbon structures from organic-organic self-assembly. Chem Mat. 2006;18(18):4447-64.

[102] Meng Y, Gu D, Zhang FQ, Shi YF, Yang HF, Li Z, et al. Ordered mesoporous polymers and homologous carbon frameworks: Amphiphilic surfactant templating and direct transformation. Angew Chem, Int Ed. 2005;44(43):7053-9.

[103] Zhang FQ, Meng Y, Gu D, Yan Y, Yu CZ, Tu B, et al. A facile aqueous route to synthesize highly ordered mesoporous polymers and carbon frameworks with Ia(3)over-bard bicontinuous cubic structure. J Am Chem Soc. 2005;127(39):13508-9.

[104] Wu Z, Webley PA, Zhao D. Post-enrichment of nitrogen in soft-templated ordered mesoporous carbon materials for highly efficient phenol removal and CO2 capture. J Mater Chem. 2012;22(22):11379.

[105] Hao G-P, Li W-C, Qian D, Wang G-H, Zhang W-P, Zhang T, et al. Structurally Designed Synthesis of Mechanically Stable Poly(benzoxazine-co-resol)-Based Porous Carbon Monoliths and Their Application as High-Performance CO 2Capture Sorbents. J Am Chem Soc. 2011;133(29):11378-88.

[106] Liu L, Deng Q-F, Ma T-Y, Lin X-Z, Hou X-X, Liu Y-P, et al. Ordered mesoporous carbons: citric acid-catalyzed synthesis, nitrogen doping and CO2 capture. J Mater Chem. 2011;21(40):16001-9.

[107] Liang CD, Dai S, Guiochon G. A graphitized-carbon monolithic column. Anal Chem. 2003;75(18):4904-12.

[108] Mayes RT, Tsouris C, Kiggans JO, Mahurin SM, DePaoli DW, Dai S. Hierarchical ordered mesoporous carbon from phloroglucinol-glyoxal and its application in capacitive deionization of brackish water. J Mater Chem. 2010;20(39):8674-8.

[109] Fulvio PF, Mayes RT, Wang X, Mahurin SM, Bauer JC, Presser V, et al. "Brick-and-Mortar" Self-Assembly Approach to Graphitic Mesoporous Carbon Nanocomposites. Adv Funct Mater. 2011;21(12):2208-15.

[110] Zhu X, Hillesheim PC, Mahurin SM, Wang C, Tian C, Brown S, et al. Efficient CO2 Capture by Porous, Nitrogen-Doped Carbonaceous Adsorbents Derived from Task-Specific Ionic Liquids. ChemSusChem. 2012;5(10):1912-7.

[111] Jansen RJJ, Vanbekkum H. Amination and Ammoxidation of Activated Carbons. Carbon. 1994;32(8):1507-16.

[112] Zhai Y, Dou Y, Zhao D, Fulvio PF, Mayes RT, Dai S. Carbon Materials for Chemical Capacitive Energy Storage. Adv Mater (Weinheim, Ger). 2011;23(42):4828-50.

[113] Pevida C, Plaza MG, Arias B, Fermoso J, Rubiera F, Pis JJ. Surface modification of activated carbons for CO2 capture. Appl Surf Sci. 2008;254(22):7165-72.

[114] Li Q, Yang JP, Feng D, Wu ZX, Wu QL, Park SS, et al. Facile synthesis of porous carbon nitride spheres with hierarchical three-dimensional mesostructures for CO(2) capture. Nano Res. 2010;3(9):632-42.

[115] Deng Q-F, Liu L, Lin X-Z, Du G, Liu Y, Yuan Z-Y. Synthesis and CO2 capture properties of mesoporous carbon nitride materials. Chem Eng J (Lausanne). 2012;203(0):63-70.

[116] Liu L, Deng Q-F, Hou X-X, Yuan Z-Y. User-friendly synthesis of nitrogen-containing polymer and microporous carbon spheres for efficient CO2 capture. J Mater Chem. 2012;22(31):15540-8.

[117] Chandra V, Yu SU, Kim SH, Yoon YS, Kim DY, Kwon AH, et al. Highly selective CO2 capture on N-doped carbon produced by chemical activation of polypyrrole functionalized graphene sheets. Chem Commun. 2012;48(5):735-7.

[118] Nandi M, Okada K, Dutta A, Bhaumik A, Maruyama J, Derks D, et al. Unprecedented CO2 uptake over highly porous N-doped activated carbon monoliths prepared by physical activation. Chem Commun (Cambridge, U K). 2012.

[119] Yang H, Yuan Y, Tsang SCE. Nitrogen-enriched carbonaceous materials with hierarchical micro-mesopore structures for efficient CO2 capture. Chem Eng J (Lausanne). 2012;185-186:374-9.

[120] Gutiérrez MC, Carriazo D, Ania CO, Parra JB, Ferrer ML, del Monte F. Deep eutectic solvents as both precursors and structure directing agents in the synthesis of nitrogen doped hierarchical carbons highly suitable for CO2 capture. Eng Env Sci. 2011;4(9):3535.

[121] Novoselov KS, Geim AK, Morozov SV, Jiang D, Zhang Y, Dubonos SV, et al. Electric field effect in atomically thin carbon films. Science. 2004;306(5696):666-9.

[122] Geim AK, Novoselov KS. The rise of graphene. Nat Mater. 2007;6(3):183-91.

[123] Rao CNR, Sood AK, Subrahmanyam KS, Govindaraj A. Graphene: The New Two-Dimensional Nanomaterial. Angew Chem, Int Ed. 2009;48(42):7752-77.

[124] Jiang DE, Sumpter BG, Dai S. Unique chemical reactivity of a graphene nanoribbon's zigzag edge. J Chem Phys. 2007;126(13):134701.

[125] Chiappe C, Pieraccini D. Ionic liquids: solvent properties and organic reactivity. J Phys Org Chem. 2005;18(4):275-97.

[126] Wang XQ, Dai S. Ionic Liquids as Versatile Precursors for Functionalized Porous Carbon and Carbon-Oxide Composite Materials by Confined Carbonization. Angewandte Chemie-International Edition. 2010;49(37):6664-8.

[127] Paraknowitsch JP, Thomas A, Antonietti M. A detailed view on the polycondensation of ionic liquid monomers towards nitrogen doped carbon materials. J Mater Chem. 2010;20(32):6746-58.

[128] Paraknowitsch JP, Zhang J, Su DS, Thomas A, Antonietti M. Ionic Liquids as Precursors for Nitrogen-Doped Graphitic Carbon. Adv Mater (Weinheim, Ger). 2010;22(1):87-92.

[129] Lee JS, Wang XQ, Luo HM, Dai S. Fluidic Carbon Precursors for Formation of Functional Carbon under Ambient Pressure Based on Ionic Liquids. Adv Mater (Weinheim, Ger). 2010;22(9):1004-+.

[130] Lee JS, Wang XQ, Luo HM, Baker GA, Dai S. Facile Ionothermal Synthesis of Microporous and Mesoporous Carbons from Task Specific Ionic Liquids. J Am Chem Soc. 2009;131(13):4596-+.

[131] Welton T. Room-temperature ionic liquids. Solvents for synthesis and catalysis. Chem Rev (Washington, DC, U S). 1999;99(8):2071-83.

[132] Ma Z, Yu JH, Dai S. Preparation of Inorganic Materials Using Ionic Liquids. Adv Mater (Weinheim, Ger). 2010;22(2):261-85.

[133] Paraknowitsch JP, Thomas A. Functional Carbon Materials From Ionic Liquid Precursors. Macromol Chem Phys. 2012;213(10-11):1132-45.

[134] Ma Z, Yu J, Dai S. Preparation of Inorganic Materials Using Ionic Liquids. Adv Mater (Weinheim, Ger). 2010;22(2):261-85.

[135] Gutierrez MC, Carriazo D, Ania CO, Parra JB, Ferrer ML, del Monte F. Deep eutectic solvents as both precursors and structure directing agents in the synthesis of nitrogen doped hierarchical carbons highly suitable for CO(2) capture. Eng Env Sci. 2011;4(9):3535-44.

[136] Sculley JP, Verdegaal WM, Lu WG, Wriedt M, Zhou HC. High-Throughput Analytical Model to Evaluate Materials for Temperature Swing Adsorption Processes. Adv Mater (Weinheim, Ger). 2013;25(29):3957-61.

[137] Bhadra SJ, Ebner AD, Ritter JA. On the Use of the Dual Process Langmuir Model for Predicting Unary and Binary Isosteric Heats of Adsorption. Langmuir. 2012;28(17):6935-41.

[138] Chakraborty A, Saha BB, Koyama S, Ng KC. On the thermodynamic modeling of the isosteric heat of adsorption and comparison with experiments. Appl Phys Lett. 2006;89(17):171901.

[139] Levesque D, Lamari FD. Pore geometry and isosteric heat: an analysis of carbon dioxide adsorption on activated carbon. Mol Phys. 2009;107(4-6):591-7.

[140] Liu YM, Ye Q, Shen M, Shi JJ, Chen J, Pan H, et al. Carbon Dioxide Capture by Functionalized Solid Amine Sorbents with Simulated Flue Gas Conditions. Environ Sci Technol. 2011;45(13):5710-6.

[141] Mohr R, Rao MB. Isosteric Heat of Adsorption: Theory and Experiment. J Phys Chem B. 1999;103(31):6539-46.

[142] Pan H, Ritter JA, Balbuena PB. Examination of the approximations used in determining the isosteric heat of adsorption from the Clausius-Clapeyron equation. Langmuir. 1998;14(21):6323-7.

[143] Whittaker PB, Wang X, Regenauer-Lieb K, Chua HT. Predicting isosteric heats for gas adsorption. Phys Chem Chem Phys. 2012;15(2):473.

[144] Cessford NF, Seaton NA, Düren T. Evaluation of Ideal Adsorbed Solution Theory as a Tool for the Design of Metal–Organic Framework Materials. Ind Eng Chem Res. 2012;51(13):4911-21.

[145] Chen J, Loo LS, Wang K. An Ideal Absorbed Solution Theory (IAST) Study of Adsorption Equilibria of Binary Mixtures of Methane and Ethane on a Templated Carbon. J Chem Eng Data. 2011;56(4):1209-12.

[146] Heidari A, Younesi H, Rashidi A, Ghoreyshi AA. Evaluation of CO2 adsorption with eucalyptus wood based activated carbon modified by ammonia solution through heat treatment. Chem Eng J (Lausanne). 2014;254:503-13.

[147] Wu F-C, Tseng R-L, Juang R-S. Comparisons of porous and adsorption properties of carbons activated by steam and KOH. J Colloid Interface Sci. 2005;283(1):49-56.

[148] Zhao L, Bacsik Z, Hedin N, Wei W, Sun YH, Antonietti M, et al. Carbon Dioxide Capture on Amine-Rich Carbonaceous Materials Derived from Glucose. ChemSusChem. 2010;3(7):840-5.

[149] Bezerra DP, Oliveira RS, Vieira RS, Cavalcante CL, Azevedo DCS. Adsorption of CO2 on nitrogen-enriched activated carbon and zeolite 13X. Adsorption. 2011;17(1):235-46.

[150] Chen C, Kim J, Ahn W-S. Efficient carbon dioxide capture over a nitrogen-rich carbon having a hierarchical micro-mesopore structure. Fuel. 2012;95(C):360-4.

[151] García S, Pis JJ, Rubiera F, Pevida C. Predicting Mixed-Gas Adsorption Equilibria on Activated Carbon for Precombustion CO2 Capture. Langmuir. 2013;29(20):6042-52.

[152] Plaza MG, García S, Rubiera F, Pis JJ, Pevida C. Evaluation of ammonia modified and conventionally activated biomass based carbons as CO2 adsorbents in postcombustion conditions. Sep Purif Technol. 2011;80(1):96-104.

[153] Chen JH, Loo LS, Wang K. An Ideal Absorbed Solution Theory (IAST) Study of Adsorption Equilibria of Binary Mixtures of Methane and Ethane on a Templated Carbon. J Chem Eng Data. 2011;56(4):1209-12.

[154] Zhu X, Tian C, Chai S, Nelson K, Han KS, Hagaman EW, et al. New Tricks for Old Molecules: Development and Application of Porous N-doped, Carbonaceous Membranes for CO2 Separation. Adv Mater (Weinheim, Ger). 2013:n/a-n/a.

[155] Bollini P, Brunelli NA, Didas SA, Jones CW. Dynamics of CO 2Adsorption on Amine Adsorbents. 1. Impact of Heat Effects. Ind Eng Chem Res. 2012;51(46):15145-52.

[156] Himeno S, Komatsu T, Fujita S. High-Pressure Adsorption Equilibria of Methane and Carbon Dioxide on Several Activated Carbons. J Chem Eng Data. 2005;50(2):369-76.

[157] Lee J-S, Kim J-H, Kim J-T, Suh J-K, Lee J-M, Lee C-H. Adsorption Equilibria of CO 2on Zeolite 13X and Zeolite X/Activated Carbon Composite. J Chem Eng Data. 2002;47(5):1237-42.

[158] Malek A, Farooq S. Comparison of isotherm models for hydrocarbon adsorption on activated carbon. AIChE J. 1996.

[159] Biniak S, Szymanski G, Siedlewski J, Swiatkowski A. The characterization of activated carbons with oxygen and nitrogen surface groups. Carbon. 1997;35(12):1799-810.

[160] Jansen RJJ, Vanbekkum H. XPS of nitrogen-containing functional-groups on activated carbon. Carbon. 1995;33(8):1021-7.

[161] van der Heide P. X-Ray Photoelectron Spectroscopy: An Introduction to Priniciples and Practices. Hoboken, NJ: John Wiley & Sons; 2011.

[162] Maroto-Valer MM, Lu Z, Zhang YZ, Tang Z. Sorbents for CO2 capture from high carbon fly ashes. Waste Manag. 2008;28(11):2320-8.

[163] Maroto-Valer MM, Tang Z, Zhang Y. CO2 capture by activated and impregnated anthracites. Fuel Process Technol. 2005;86(14-15):1487-502.

[164] Zhang Z, Xu M, Wang H, Li Z. Enhancement of CO2 adsorption on high surface area activated carbon modified by N2, H2 and ammonia. Chem Eng J (Lausanne). 2010;160(2):571-7.

[165] Paola Vargas D, Giraldo L, Silvestre-Albero J, Carlos Moreno-Pirajan J. CO2 adsorption on binderless activated carbon monoliths. Adsorption-Journal of the International Adsorption Society. 2011;17(3):497-504.

[166] Dai S, Guiochon GA, Liang C, inventors; Robust carbon monolith having hierarchical porosity patent U.S. Pat. No. 7,892,516. 2008.

[167] Liang C, Dai S. Dual Phase Separation for Synthesis of Bimodal Meso-/Macroporous Carbon Monoliths. Chem Mat. 2009;21:2115-24.

[168] Wang XL, Chengdu; Dai, Sheng. Facile Synthesis of Ordered Mesoporous Carbons with High Thermal Stability By Self-Assemly of Resorcinol-Formaldehyde and Block Copolymers under Highly Acidic Conditions. Langmuir. 2008;24:7500-5.

[169] Robeson LM. Polymer Blends: A comprehensive review. Cincinnati, OH: Hanser-Gardner Publications, Inc.; 2007.

[170] Robeson LM. Polymer Blends. Cincinnati, OH: Hanser Gardner Publications, Inc. ; 2007.

[171] Zhulina EB, Borisov OV. Theory of Block Polymer Micelles: Recent Advances and Current Challenges. Macromolecules. 2012;45(11):4429-40.

[172] Koo K, Ahn H, Kim SW, Ryu DY, Russell TP. Directed self-assembly of block copolymers in the extreme: guiding microdomains from the small to the large. Soft Matter. 2013;9(38):9059-71.

[173] Arrigo R, Hävecker M, Wrabetz S, Blume R, Lerch M, McGregor J, et al. Tuning the Acid/Base Properties of Nanocarbons by Functionalization via Amination. J Am Chem Soc. 2010;132(28):9616-30.

[174] Zhao y, Liu X, Yao KX, Zhao L, Han Y. Superior Capture of CO2 Achieved by Introducing Extra- framework Cations into N-doped Microporous Carbon. Chem Mat. 2012:1-13.

[175] Shafeeyan MS, Daud W, Houshmand A, Arami-Niya A. Ammonia modification of activated carbon to enhance carbon dioxide adsorption: Effect of pre-oxidation. Appl Surf Sci. 2011;257(9):3936-42.

[176] Liang C, Li Z, Dai S. Mesoporous Carbon Materials: Synthesis and Modification. Angew Chem, Int Ed. 2008;47(20):3696-717.

[177] Shi Y, Wan Y, Zhao D. Ordered mesoporous non-oxide materials. Chem Soc Rev. 2011;40(7):3854.

[178] Zhai YP, Dou YQ, Zhao DY, Fulvio PF, Mayes RT, Dai S. Carbon Materials for Chemical Capacitive Energy Storage. Adv Mater. 2011;23(42):4828-50.

[179] Seo M, Hillmyer MA. Reticulated Nanoporous Polymers by Controlled Polymerization-Induced Microphase Separation. Science. 2012;336(6087):1422-5.

[180] Lu AH, Schüth F. Nanocasting: A Versatile Strategy for Creating Nanostructured Porous Materials. Adv Mater (Weinheim, Ger). 2006;18(14):1793-805.

[181] Meng Y, Gu D, Zhang F, Shi Y, Cheng L, Feng D, et al. A Family of Highly Ordered Mesoporous Polymer Resin and Carbon Structures from Organic−Organic Self-Assembly. Chem Mat. 2006;18(18):4447-64.

[182] Meng Y, Gu D, Zhang F, Shi Y, Yang H, Li Z, et al. Ordered Mesoporous Polymers and Homologous Carbon Frameworks: Amphiphilic Surfactant Templating and Direct Transformation. Angew Chem, Int Ed. 2005;44(43):7053-9.

[183] Tanaka S, Nakatani N, Doi A, Miyake Y. Preparation of ordered mesoporous carbon membranes by a soft-templating method. Carbon. 2011;49(10):3184-9.

[184] Brun N, García-González CA, Smirnova I, Titirici MM. Hydrothermal synthesis of highly porous carbon monoliths from carbohydrates and phloroglucinol. RSC Advances. 2013;3(38):17088.

[185] Vrandecic NS, Erceg M, Jakic M, Klaric I. Kinetic analysis of thermal degradation of poly(ethylene glycol) and poly(ethylene oxide)s of different molecular weight. Thermochim Acta. 2010;498(1-2):71-80.

[186] Wang FY, Ma CCM, Wu WJ. Kinetic parameters of thermal degradation of polyethylene glycol-toughened novolac-type phenolic resin. J Appl Polym Sci. 2001;80(2):188-96.

[187] Hammouda B, Ho DL, Kline S. Insight into Clustering in Poly(ethylene oxide) Solutions. Macromolecules. 2004;37(18):6932-7.

[188] Pang P, Englezos P. Kinetics of the aggregation of polyethylene oxide at temperatures above the polyethylene oxide–water cloud point temperature. Colloids Surf, A. 2002;204(1):23-30.

[189] Briscoe B, Luckham P, Zhu S. Rheological properties of poly (ethylene oxide) aqueous solutions. J Appl Polym Sci. 1998;70(3):419-29.

[190] Mehrdad A, Akbarzadeh R. Effect of Temperature and Solvent Composition on the Intrinsic Viscosity of Poly(ethylene glycol) in Water−Ethanol Solutions. J Chem Eng Data. 2010;55(7):2537-41.

[191] Wang X, Lee JS, Tsouris C, DePaoli DW, Dai S. Preparation of activated mesoporous carbons for electrosorption of ions from aqueous solutions. J Mater Chem. 2010;20(22):4602-7.

[192] Norisuye T, Takeda M, Shibayama M. Cluster-Size Distribution of Cross-Linked Polymer Chains across the Gelation Threshold. Macromolecules. 1998;31:1-7.

[193] Binder K. Dynamics of Phase-Separation and Critical Phenomena in Polymer Mixtures. Colloid Polym Sci. 1987;265(4):273-88.

[194] Plaza MG, Pevida C, Arias B, Casal MD, Martin CF, Fermoso J, et al. Different Approaches for the Development of Low-Cost CO2 Adsorbents. J Environ Eng-ASCE. 2009;135(6):426-32.

[195] Plaza MG, Pevida C, Arenillas A, Rubiera F, Pis JJ. CO2 capture by adsorption with nitrogen enriched carbons. Fuel. 2007;86(14):2204-12.

[196] Shen WZ, Yang XP, Guo QJ, Liu YH, Song YR, Han ZX, et al. The effect of carbon precursor on the pore size distribution of mesoporous carbon during templating synthesis process. Mater Lett. 2006;60(29-30):3517-21.

[197] Wang X, Liang C, Dai S. Facile Synthesis of Ordered Mesoporous Carbons with High Thermal Stability By Self-Assembly of Resorcinol-Formaldehyde and Block Copolymers under Highly Acidic Conditions. Langmuir. 2008;24(14):7500-5.

[198] Belgacem MN, Gandini A. Monomers, Polymers and Composites from Renewable Resources. Amsterdam; Boston: Elsevier; 2008.

[199] Pizzi A. Condensed Tannins for Adhesives. Ind Eng Chem Prod Rd. 1982;21(3):359-69.

[200] Hagerman AE, Zhao Y, Johnson S. Methods for determination of condensed and hydrolyzable tannins. In: Shahidi F, ed. Antinutrients and Phytochemicals in Food. Washington: ACS 1997, p. 209-22.

[201] Spina S, Zhou X, Segovia C, Pizzi A, Romagnoli M, Giovando S, et al. Phenolic resin adhesives based on chestnut (Castanea sativa) hydrolysable tannins. J Adhes Sci Technol. 2013;27(18-19):2103-11.

[202] Garro Galvez JM, Riedl B. Pyrogallol–formaldehyde thermosetting adhesives. J Appl Polym Sci. 1998;65(2):399-408.

[203] Szczurek A, Amaral-Labat G, Fierro V, Pizzi A, Masson E, Celzard A. The use of tannin to prepare carbon gels. Part I: Carbon aerogels. Carbon. 2011;49(8):2773-84.

[204] Szczurek A, Amaral-Labat G, Fierro V, Pizzi A, Celzard A. The use of tannin to prepare carbon gels. Part II. Carbon cryogels. Carbon. 2011;49(8):2785-94.

[205] Peña C, Larrañaga M, Gabilondo N, Tejado A, Echeverria JM, Mondragon I. Synthesis and characterization of phenolic novolacs modified by chestnut and mimosa tannin extracts. J Appl Polym Sci. 2006;100(6):4412-9.

[206] Lowell S, Shields JE, Thomas MA, Thommes M. Micropore Analysis. Characterization of Porous Solids and Powders: Surface Area, Pore Size and Density. Dordrecht, The Netherlands: Kluwer Academic Publishers 2004, p. 1-29.

[207] Salame, II, Bandosz TJ. Surface Chemistry of Activated Carbons: Combining the Results of Temperature-Programmed Desorption, Boehm, and Potentiometric Titrations. J Colloid Interface Sci. 2001;240(1):252-8.

[208] Sing KSW. Adsorption methods for the characterization of porous materials. Adv Colloid Interface Sci. 1998;76:3-11.

[209] Kruk M, Jaroniec M. Gas Adsorption Characterization of Ordered Organic−Inorganic Nanocomposite Materials. Chem Mat. 2001;13(10):3169-83.

[210] Liang CD, Li ZJ, Dai S. Mesoporous carbon materials: Synthesis and modification. Angew Chem, Int Ed. 2008;47(20):3696-717.

[211] Brinker CJ, Lu Y, Sellinger A, Fan H. Evaporation-induced self-assembly: nanostructures made easy. Adv Mater. 1999;11(7):579-85.

[212] Raquez JM, Deleglise M, Lacrampe MF, Krawczak P. Thermosetting (bio)materials derived from renewable resources: A critical review. Prog Polym Sci. 2010;35(4):487-509.

[213] Conner AH. Wood: Adhesives. Amsterdam: Elsevier Science, Ltd. ; 2004.

[214] Wan Y, Shi YF, Zhao DY. Supramolecular aggregates as templates: Ordered mesoporous polymers and carbons. Chem Mat. 2008;20(3):932-45.

[215] Schlienger S, Graff A-L, Celzard A, Parmentier J. Direct synthesis of ordered mesoporous polymer and carbon materials by a biosourced precursor. Green Chem. 2012;14(2):313.

[216] Nguyen PTM, Do DD, Nicholson D. On the Irreversibility of the Adsorption Isotherm in a Closed-End Pore. Langmuir. 2013;29(9):2927-34.

[217] Long DH, Qiao WM, Zhan L, Liang XY, Ling LC. Effect of template and precursor chemistry on pore architectures of triblock copolymer-templated mesoporous carbons. Microporous Mesoporous Mater. 2009;121(1-3):58-66.

[218] Sculley JP, Verdegaal WM, Lu W, Wriedt M, Zhou H-C. High-Throughput Analytical Model to Evaluate Materials for Temperature Swing Adsorption Processes. Adv Mater (Weinheim, Ger). 2013;25(29):3957-61.

[219] Teng H, Wang SC. Preparation of porous carbons from phenol–formaldehyde resins with chemical and physical activation. Carbon. 2000;38(6):817-24.

[220] Enterria M, Suárez-García F, Martínez-Alonso A, Tascón JMD. Synthesis of ordered micro-mesoporous carbons by activation of SBA-15 carbon replicas. Microporous Mesoporous Mater. 2012;151(C):390-6.

[221] Boudou JP. Surface chemistry of a viscose-based activated carbon cloth modified by treatment with ammonia and steam. Carbon. 2003;41(10):1955-63.

[222] Pevida C, Plaza MG, Arias B, Fermoso J, Rubiera F, Pis JJ. Surface modification of activated carbons for CO(2) capture. Appl Surf Sci. 2008;254(22):7165-72.

[223] Przepiorski J, Skrodzewicz M, Morawski AW. High temperature ammonia treatment of activated carbon for enhancement of CO2 adsorption. Appl Surf Sci. 2004;225(1-4):235-42.

[224] Plaza MG, Rubiera F, Pis JJ, Pevida C. Ammoxidation of carbon materials for CO2 capture. Appl Surf Sci. 2010;256(22):6843-9.

[225] Shafeeyan MS, Daud WMAW, Houshmand A, Arami-Niya A. Ammonia modification of activated carbon to enhance carbon dioxide adsorption: Effect of pre-oxidation. Appl Surf Sci. 2011;257(9):3936-42.

[226] Mahurin SM, Lee JS, Wang X, Dai S. Ammonia-activated mesoporous carbon membranes for gas separations. J Membrane Sci. 2011;368(1-2):41-7.

[227] Wang XQ, Lee JS, Tsouris C, DePaoli DW, Dai S. Preparation of activated mesoporous carbons for electrosorption of ions from aqueous solutions. J Mater Chem. 2010;20(22):4602-8.

[228] Stohr B, Boehm HP, Schlogl R. Enhancement of the Catalytic Activity of Activated Carbons in Oxidation Reactions by Thermal-Treatment with Ammonia or Hydrogen-Cyanide and Observation of a Superoxide Species as a Possible Intermediate. Carbon. 1991;29(6):707-20.

[229] Shen WZ, Fan WB. Nitrogen-containing porous carbons: synthesis and application. J Mater Chem A. 2013;1(4):999-1013.

[230] Montes-Moran MA, Suarez D, Menendez JA, Fuente E. On the nature of basic sites on carbon surfaces: An overview. Carbon. 2004;42(7):1219-25.

[231] Zhu X, Tian CC, Chai SH, Nelson K, Han KS, Hagaman EW, et al. New Tricks for Old Molecules: Development and Application of Porous N-doped, Carbonaceous Membranes for CO2 Separation. Adv Mater (Weinheim, Ger). 2013;25(30):4152-8.

[232] Qiao ZA, Chai SH, Nelson K, Bi ZG, Chen JH, Mahurin SM, et al. Polymeric molecular sieve membranes via in situ cross-linking of non-porous polymer membrane templates. Nature Communications. 2014;5.

[233] Mahurin SM, Gorka J, Nelson KM, Mayes RT, Dai S. Enhanced CO2/N-2 selectivity in amidoxime-modified porous carbon. Carbon. 2014;67:457-64.

[234] Chai SH, Fulvio PF, Hillesheim PC, Qiao ZA, Mahurin SM, Dai S. "Brick-and-mortar" synthesis of free-standing mesoporous carbon nanocomposite membranes as supports of room temperature ionic liquids for CO2-N-2 separation. J Membrane Sci. 2014;468:73-80.

[235] Myers AL, Prausnitz JM. Thermodynamics of Mixed-Gas Adsorption AIChE J. 1965;11(1):1-7.

[236] Lin W. Gas Sorption and the Consequent Volumetric and Permeability Change of Coal. Department of Energy Resources and Engineering. Stanford University, PhD, 2010.

# APPENDIX

# Appendix A. MatLab Code for Adsorption Calculations

```
%% Fitting of CO2 Adsorption isotherms for isosteric heat calculation
% %%%%%%%%%%%%%%%%%%%%%%%%%%%%%%%%%%%%%%%%%%%%%%%%%%%%%%%%%%%%%%%%%%%%%%%%%%%%%%%
% Use this script for fitting of adsorption isotherms to evalutate
%     goodness of fit statistics and for isosteric heat calculation
%         - sum of squared error, root mean squared error, adjusted r2
%           error, and rmse
%         - provides temperature independent fitting parameters
%         - provides isosteric heat values (kJ/mol)  vs. loading (mmol)
%       Includes conversion to "param" format to substitute in script that
%       uses "fitAdsorptionisotherm.m" for fitting.
%       *Column 1 - Pressure (kPa) *Column 2 - Uptake (mmol/g)
%   Last Modified 11 - Aug - 2014
%%%%%%%%%%%%%%%%%%%%%%%%%%%%%%%%%%%%%%%%%%%%%%%%%%%%%%%%%%%%%%%%%%%%%%%%%%%%%%%
close all
clear all
clc


R=8.314;
T1=273;     %Insert temperature for first isotherm here
disp('Select CO2 isotherm at 0C');
filename=uigetfile('.txt');
disp(filename);
disp('Select CO2 isotherm at 25C');
filename2=uigetfile('.txt');
disp(filename2);

[pressure, uptake] = importfile1(filename, 'CO2');

T2=298;     %Insert temperature for second isotherm here

[pressure1, uptake1] = importfile1(filename2, 'CO2');



%Fitting and data from fits for tables

%Langmuir
[fitresult, gof] = LangmuirFit(pressure, uptake); %Fit isotherms
[fitresult5, gof5] = LangmuirFit(pressure1, uptake1);

x0 = coeffvalues(fitresult);                      %Extract parameters
x5 = coeffvalues(fitresult5);

errors0=struct2cell(gof);        %Parameters in cells for table
errors5=struct2cell(gof5);

%Freundlich
[fitresult1, gof1] = FreundlichFit(pressure, uptake);   %Fit isoterms
[fitresult6, gof6] = FreundlichFit(pressure1, uptake1);

x1 = coeffvalues(fitresult1);           %Extract parameters
x6 = coeffvalues(fitresult6);

errors1=struct2cell(gof1);      %Parameters in cells for table
errors6=struct2cell(gof6);
```

```
%Sips
[fitresult2, gof2] = SipsFit(pressure, uptake);     %Fit isotherms
[fitresult7, gof7] = SipsFit(pressure1, uptake1);

x2 = coeffvalues(fitresult2);           %Extract parameters
x7 = coeffvalues(fitresult7);

errors2=struct2cell(gof2);      %Parameters in cells for table
errors7=struct2cell(gof7);

%Toth
[fitresult3, gof3] = TothFit(pressure, uptake); %Fit isotherms
[fitresult8, gof8] = TothFit(pressure1, uptake1);

x3 = coeffvalues(fitresult3);       %Extract parameters
x8 = coeffvalues(fitresult8);

errors3=struct2cell(gof3);          %Parameters in cells for table
errors8=struct2cell(gof8);

%Dual Site Langmuir
%***Coefficients from this fitting included in table where N1=m and K1=t
[fitresult4, gof4] = DualLangmuirFit(pressure, uptake); %Fit isotherms
[fitresult9, gof9] = DualLangmuirFit(pressure1, uptake1);

x4 = coeffvalues(fitresult4);       %Extract parameters
x9 = coeffvalues(fitresult9);

errors4=struct2cell(gof4);          %Parameters in cells for table
errors9=struct2cell(gof9);


% Plot experimental data with fitted data (both temperatures)

%Langmuir
figure( 'Name', 'Langmuir fit' );
h = plot( fitresult,'r-', pressure, uptake, 'k.');
    hold on
    plot( fitresult5, 'k-', pressure1, uptake1, 'b.');
    hold on
    legend( 'experimental 273 K', 'Langmuir fit 273 K',...
        'experimental 298 K', 'Langmuir 298 K');
    legend('Location', 'SouthEast' ); %Move legend to lower right
    % Label axes
    xlabel( 'Pressure (kPa)' );
    ylabel( 'Uptake (mmol/g)' );
    grid off
    set(gcf,'Color',[1 1 1])

% Freundlich
figure( 'Name', 'Freundlich fit' );
h1 = plot( fitresult1, 'r-', pressure, uptake, 'k.');
    hold on
    plot( fitresult6, 'k-', pressure1, uptake1, 'b.');
    hold on
    legend( 'experimental 273 K', 'Freundlich fit 273 K',...
        'experimental 298 K', 'Freundlich 298 K');
    legend('Location', 'SouthEast' ); %Move legend to lower right
```

```
    % Label axes
    xlabel( 'Pressure (kPa)' );
    ylabel( 'Uptake (mmol/g)' );
    grid off
    set(gcf,'Color',[1 1 1])

% Sips
figure( 'Name', 'Sips fit' );
h2 = plot( fitresult2,'r-', pressure, uptake, 'k.');
    hold on
    plot( fitresult7, 'k-', pressure1, uptake1, 'b.');
    hold on
    legend( 'experimental 273 K', 'Sips fit 273 K',...
        'experimental 298 K', 'Sips 298 K');
    legend('Location', 'SouthEast' ); %Move legend to lower right
    % Label axes
    xlabel( 'Pressure (kPa)' );
    ylabel( 'Uptake (mmol/g)' );
    grid off
    set(gcf,'Color',[1 1 1])

% Toth
figure( 'Name', 'Toth fit ' );
h3 = plot( fitresult3, 'r-', pressure, uptake, 'k.');
    hold on
    plot( fitresult8, 'k-', pressure1, uptake1, 'b.');
    hold on
    legend( 'experimental 273 K', 'Toth fit 273 K',...
        'experimental 298 K', 'Toth 298 K');
    legend('Location', 'SouthEast' ); %Move legend to lower right
    % Label axes
    xlabel( 'Pressure (kPa)' );
    ylabel( 'Uptake (mmol/g)' );
    grid off
    set(gcf,'Color',[1 1 1])

% Dual Site Langmuir
figure( 'Name', 'Dual Langmuir fit' );
h4 = plot( fitresult4, 'r-', pressure, uptake, 'k.');
    hold on
    plot( fitresult9, 'k-', pressure1, uptake1, 'b.');
    hold on
    legend( 'experimental 273 K', 'Dual Langmuir fit 273 K',...
        'experimental 298 K', 'Dual Langmuir 298 K');
    legend('Location', 'SouthEast' ); %Move legend to lower right
    % Label axes
    xlabel( 'Pressure (kPa)' );
    ylabel( 'Uptake (mmol/g)' );
    grid off
    set(gcf,'Color',[1 1 1])


%Table of all fitting errors and parameter values

Isotherms={'Langmuir 273 K'; 'Freundlich 273 K'; 'Sips 273 K';...
    'Toth 273 K'; 'DSL 273 K';...
    'Langmuir 298 K'; 'Freundlich 298 K'; 'Sips 298 K';...
    'Toth 298 K'; 'DSL 298 K'};
```

```
SSE = [errors0(1); errors1(1); errors2(1); errors3(1); errors4(1);...
       errors5(1); errors6(1); errors7(1); errors8(1); errors9(1)];
%Sum of squared error (SSE) is a measure of the total deviation of response
% values from the fit. Values closest to 0 is best.
rsquare = [errors0(2); errors1(2); errors2(2); errors3(2);...
       errors4(2); errors5(2); errors6(2); errors7(2); errors8(2);
       errors9(2)];
%Rsquare is calculated from the sum of squares of the regression(SSR) and
% the total number of squares or squares about the mean (SST).
% SST=SSR+SSE and rsquare=SSR/SST=1-SSE/SST
% Values closest to 1 are best.

%dfe = [errors0(3); errors1(3); errors2(3); errors3(3); errors4(3);...
%       errors5(3); errors6(3); errors7(3); errors8(3); errors9(3)];

adjrsquare = [errors0(4); errors1(4); errors2(4); errors3(4);...
              errors4(4);errors5(4); errors6(4); errors7(4); ...
              errors8(4); errors9(4)];
%Adjusted rsquare value adjusts for degrees of freedom via v=n-m where
%  n=# of response values and m= # of fitted coefficients.
% adj.rsquare= 1- (SSE(n-1))/(SST(v))

rmse = [errors0(5); errors1(5); errors2(5); errors3(5); errors4(5);...
       errors5(5); errors6(5); errors7(5); errors8(5); errors9(5)];
% Root mean squared error - the fit standard error and the standard error
% of the regression. RMSE=s=sqrt(MSE)   MSE=SSE/v
%Values closer to 0 indicated better fit.

%N0 is the saturation capacity of the surface
N0=[x0(2); 0; x2(2); x3(2); x4(4);...
    x5(2); 0; x7(2); x8(2); x9(4)];

%K is regarded as the affinity coefficent, although it holds no meaning in
% the Freundlich equation
K=[x0(1); x1(1); x2(1); x3(1); x4(1);...
    x5(1); x6(1); x7(1); x8(1); x9(1)];

%m is used as a exponential coefficient in the Freundlich and Sips equation
% but only holds meaning as a measure of system heterogeneity in the Sips,
% increasing with increasing heterogeneity.
m=[0; x1(2); x2(3); 0; x4(3);...
    0; x6(2); x7(3); 0; x9(3)];

%While the t is also a measure of increasing system heterogeneity in the
%Toth equation as deviation from 1 increases, a value of 1 (homongeneous)
%returns the Langmuir equation.
t=[0; 0; 0; x3(3); x4(2);...
    0; 0; 0; x8(3); x9(2)];

T=table(SSE, rsquare, adjrsquare, rmse,'RowNames', Isotherms);
D=table(N0, K, m, t,'RowNames', Isotherms);
disp(T);
disp(D);
%conversion of coefficients into parameter format
param0(1).N0=x0(2);
param0(1).K= x0(1);
param1(1).K = x1(1);
```

```
param1(1).m = x1(2);
param2(1).K = x2(1);
param2(1).N0 = x2(2);
param2(1).m = x2(3);
param3(1).K = x3(1);
param3(1).N0 = x3(2);
param3(1).t = x3(3);
param4(1).K = x4(1);
param4(1).K1 = x4(2);
param4(1).N0 = x4(4);
param4(1).N1 = x4(3);

param5(1).N0=x5(2);
param5(1).K= x5(1);
param6(1).K = x6(1);
param6(1).m = x6(2);
param7(1).K = x7(1);
param7(1).N0 = x7(2);
param7(1).m = x7(3);
param8(1).K = x8(1);
param8(1).N0 = x8(2);
param8(1).t = x8(3);
param9(1).K = x9(1);
param9(1).K1 = x9(2);
param9(1).N0 = x9(4);
param9(1).N1 = x9(3);

%%%%%%%%%%%%%%%%%%%%%%%%%%%%%%%%%%%%%%%%%%%%%%%%%%%%%%%%%%%%%%%%%%%%%%%%%%%%%%%
%Using fitting parameters to determine the isosteric heat via the
% Clausius-Clapeyron equation. By fitting at two different temperatures,
% the pressure can be evaluated at the same loading. The Clausius-Clapeyron
% equation H/R=(dlnP/d1/T) @ constant loading provides a plot by which the
% slope is equal to the adsorption enthalpy. Furthermore, by using fittings
% and solving equations, the heat can be estimated over a wide loading
% range.
%%%%%%%%%%%%%%%%%%%%%%%%%%%%%%%%%%%%%%%%%%%%%%%%%%%%%%%%%%%%%%%%%%%%%%%%%%%%%%%

%Using the Langmuir equation to get pressures
n=[0:.001:1.5];   %Loading range
nl=n';

for i=1;
    for j=1:length(nl)
    P1(j) = fzero(@(t)fitresult(t)-nl(j),[0, 100]);
    end

    for j=1:length(nl)
    P2(j) = fzero(@(t)fitresult5(t)-nl(j),[0, 100]);
    end
P3=P2./P1;


% P1=-(ng)./(x0(1).*ng-x0(1).*x0(2));
% P2=-(ng)./(x5(1).*ng-x5(1).*x5(2));
y=(R.*(log(P3)))./((1./T1)-(1./T2));
y1=y./1000;
%Clausius clapeyron equation to determine isosteric heat of adsorption
end
```

```
[F1]=log(P1)';  %code for line graphs
[temp]=repmat((1/T1),1,1501)';
[F2]=log(P2)';
[temp2]=repmat((1/T2),1,1501)';
P=[F1, F2];
T=[temp, temp2];
figure('Color',[1,1,1]);
    plot(temp, F1, temp2, F2);

slope=(F2-F1)./(temp2-temp);



%Using the Sips equation to get pressures
ns=[0:.001:1.5];   %Loading range
ns1=ns';
for i=1

    for j=1:length(ns1)
    P5(j) = fzero(@(t)fitresult2(t)-ns1(j),[0, 100]);
    end

    for j=1:length(ns1)
    P6(j) = fzero(@(t)fitresult7(t)-ns1(j),[0, 100]);
    end

y3=((R.*(log(P6./P5)./((1./T1)-(1./T2)))./1000);
end

%Using the Toth equation to get pressures
nt=[0:.001:1.5];   %Loading range
nt1=nt';
for i=1

for j=1:length(nt1)
   P7(j) = fzero(@(t)fitresult3(t)-nt1(j),[0, 100]);
end

for j=1:length(nt1)
   P8(j) = fzero(@(t)fitresult8(t)-nt1(j),[0, 100]);
end



y4=-(R.*((log(P7)-log(P8))./(1/T1-1/T2))./1000);
end



%Heat calculations all on one graph for comparison
figure('Color',[1,1,1]);
    plot(nl, y1, ns1, y3, nt1, y4);
    hold on;
    title('Isosteric Heat-Langmuir');
    xlabel('Loading (mmol/g)');
    ylabel('Isosteric heat (kJ/mol)');


    axis([0 1.5 0 50]);         %loading 0 to 1.5 mmol/g up to 50 kJ/mol
    legend('Langmuir', 'Sips', 'Toth');
```

# Appendix B. Procedure for Predicting Competitive Binary Adsorption using Ideal Adsorbed Solution Theory (IAST)

The ability to obtain several pure isotherm measurements provides an abundance of information about the adsorption process; although, binary adsorption data for the separation of $CO_2$ from $N_2$ remains elusive. This data is difficult to obtain experimentally due to the equipment and gas analysis needed for measurement but estimating adsorption equilibria by using the pure adsorption isotherms. Ideal adsorbed solution (IAS) theory was established by Myers and Prausnitz for multicomponent adsorption.[235] A factor termed spreading pressure, Π, is introduced to describe the reduction in surface tension between the adsorbate and adsorbent upon adsorption. It is the related to the chemical potential in the gaseous phase to the chemical potential in the adsorbed phase as:

$$u_i(T, p, y_1 ...) = u_i(T, \Pi, \chi_i ...) \qquad (29)$$

In Equation 21, relation to the chemical potential of the gas phase (left) and the chemical potential of the adsorbed phase (right) are equal using the Gibbs approach to vapor-adsorbate equilibrium (VAE), where the chemical potential of the gas phase is a function of temperature ($T$), pressure ($p$), and gas phase composition ($y_1$) and the chemical potential of the adsorbed phase is a function of temperature, spreading pressure ($\Pi$) and adsorbed phase composition ($\chi_i$).(ref) At low to moderate pressures, ideal gas behaviors can be used in isofugacity equations at equilibrium for a mixture of components $i$ and $j$ as:

$$y_i p = \chi_i p_i^o$$
$$y_j p = \chi_j p_j^o \qquad (30)$$

where $p_i^o$ and $p_j^o$ are the pure adsorption pressures at the same surface potential and temperature in the mixture and are analogous to the respective vapor pressures of each component in Raoult's law. The sum of the mole fractions of component *i* and *j*, $\chi_i$ and $\chi_j$, equal unity.

The relation between chemical potential and pressure is derived via the *Gibbs - Duhem* equation (at constant temperature) for a binary mixture:

$$-Ad\Pi + \sum_{i=1}^{2} n_i \, d\mu_i = 0 \qquad (31)$$

which can be simplified through integration and approximated using pressure in lieu of fugacity due to the low to moderate pressure conditions that are applicable to yield:

$$\psi_i^o = \frac{A\Pi_i^o}{RT} = \int_0^{p_i^o} \left(\frac{n}{p}\right)_i dp \qquad (32)$$

where $\psi_i^o$ is the modified surface potential, *A* is the specific surface area, *n* is the adsorbed amount, and *p* is pressure. Therefore the pure isotherms can be used to calculate:

$$\Pi_i^o = \Pi = \Pi_j^o \qquad (33)$$

$$\psi_i^o = \psi = \psi_j^o \qquad (34)$$

The adsorbed amount (*n*) in Equation 19 can be evaluated using the Langmuir model (Equation 2), the Sips model (Equation 11) or the Toth model (Equation 12). Evaluating the integral with the Langmuir equation returns:

$$\psi_i^o = q_i \ln(1 + B_i\, p_i^o) \qquad (35)$$

Due complexity of the integral of the Sips and Toth equations, the resulting hypergeometric functions are evaluated using MatLab with script found in Appendix XXX.

Predicting mixed gas adsorption and selectivity using pure adsorption isotherms provides another means to evaluate adsorbents for real environments. The adsorption curves obtained using this method provide reasonable data, while selectivity values are overestimated significantly due to the use of ideal assumptions where real gas interactions are occurring.

The seven unknowns, $\psi_j^o$, $\psi_i^o$, $\psi$, $\chi_j$, $\chi_i$, $p_j^o$, and $p_i^o$ from Equations 17, 21, and 22, along with the 2 unknowns, $n_i^o$ and $n_j^o$, from the experimental fit, were found using a procedure by Do [20]:

1. Estimating of the surface potential, $\psi$, as the mole-fraction weighted average of the pure adsorption surface potential for each component using pure adsorption pressure for initial $p_i^o$:

$$\psi = \sum_{i=1}^{2} y_i\, \psi_i^o(p_i^o) \qquad (36)$$

2. The initial estimation of $\psi$ allows for a back calculation of $p_j^o$ and $p_i^o$ for each component using the respective relation from Equation 21 for $\psi_i^o$ and $\psi_j^o$. With $p_j^o$ and $p_i^o$, calculation of $\chi_i$ and $\chi_j$ for Equation 17 with inputs *p*, $y_i$, and $y_j$ are calculated

inputs from the respective fitting.

3. An objective function that utilizes the summation of $\chi_i$ and $\chi_j$ equals unity and a Newton-Raphson iteration to improve the estimation of $\psi$:

$$F(\psi) = \sum_{i=1}^{2} \chi_i - 1 = 0 \tag{37}$$

When the Langmuir fitting for pure isotherms is used, the derivative is:

$$F'(\psi) = -\sum_{i=1}^{2} \frac{py_i}{(p_i^o(\psi))^2} \frac{dp_i^o}{d\psi} = -\sum_{i=1}^{2} \frac{py_i}{p_i^o(\psi) n_i^o} \tag{38}$$

4. The previous 2 steps are evaluated until convergence.

5. From the iteration, $p_j^o$ and $p_i^o$ are found and the parameters for the respective gas phase are found:

$$\chi_i = \frac{py_i}{p_i^o} \tag{39}$$

$$\frac{1}{n_t} = \sum \frac{\chi_i}{n_i^o} \tag{40}$$

where:

$$n_i = n_t \chi_i \tag{41}$$

The MatLab code for the Langmuir model were based on those found in a dissertation by Weijuan Lin.[236] Modifications were made for both the Sips and the Toth models.

# VITA

Kimberly Marie Nelson was born in Logan, Ohio, to Christine and Rocky Nelson. She only has one older sister, Leslie. She attended Central Elementary School in Logan until moving to rural Rockbridge to attend Rockbridge Elementary School in 1994 and continued on to Logan-Hocking Middle School and Logan High School. She was an active 4-H and FFA member after moving to Rockbridge, where she developed her love for animals. After graduation from high school, she started at Wilmington College in Wilmington, Ohio with aspirations for veterinary studies. During her 2$^{nd}$ year, she found a passion and curiosity in an introductory chemistry course and an aversion for viscera. She obtained a Bachelors of Science degree in Chemistry from Wilmington College in May 2008 with a minor in Animal Science. She accepted employment at an environmental corporation doing bench and field-testing of catalysts for $NO_x$ reduction. After the two years under employment, aspirations for a doctorate degree led to acceptance of a graduate teaching assistantship at the University of Tennessee-Knoxville on the Analytical Chemistry track in fall of 2010. She began research of porous carbon materials for separations under Dr. Sheng Dai. In December 2014, she completed the requirements for a PhD in chemistry.